Appendix A

Detector Design Details and R&D Plans

A.1 Pixel Detector

In this section, we first present a review of our R&D on pixel sensors (A.1.1). This is followed by a review of our testbeam results, with emphasis on charge collection, charge sharing, and position resolution (A.1.2). Finally, we present short sections on the bench top apparatus which we have built to explore ways to provide electromagnetic shielding for the BTeV pixel detector and its readout against pickup from the circulating beams (A.1.3), and on our recently completed radiation exposure of prototype 0.25 μm CMOS pixel readout circuits (A.1.4).

In the past two years, we have made great progress in the development of the individual components and enabling technologies required to build the BTeV pixel detector. Our R&D focus is now shifting to system engineering problems. We believe that it is very important for us to test our design ideas in real systems, and to gain experience with large scale pixel detectors. In the immediate future, our focus will be on subsystems, specifically pixel modules of a sensor bonded to 5 readout chips and to a readout "HDI." Soon after that, we will start tests of modules "shingled" onto a carbon-carbon "half-plane." Longer term, we expect to validate our BTeV design in "3%" and "10%" system tests in C0 or a test beam.

A.1.1 Sensor Design and Simulation

A.1.1.1 Introduction

A key element driving the pixel sensor design is the necessity to put these detectors as close as possible to the beam axis in order to optimize the vertex resolution. In our baseline configuration, the innermost edge is located 6 mm away from the beam line. This requirement focuses our choices on technologies optimized for an extended lifetime of the detector in a harsh radiation environment. This challenge is not unique to BTeV; it is also quite important for the LHC experiments. This allows us to progress in a cost effective way utilizing joint developments with other research groups.

The geometrical parameters of the sensor are the result of a careful optimization. The dimensions of the pixel unit cell determine the hit resolution and occupancy. In turn, they affect the complexity of the system, the space available for the pixel electronics, and the demands posed on the cooling system. The sensor thickness affects the signal to noise achievable in the course of the detector lifetime, and the resolution achievable for large angle tracks that share the charge signal among several pixel cells. The material budget is affected not only by the thickness of the active elements in this system (sensor and readout electronics), but also by the mechanical support and cooling system.

Finally, a key element to ensure that the sensor can provide useful information after high radiation dose is the ability to withstand a high reverse bias voltage. For example, the ROSE collaboration finds that the ATLAS "first layer," located at a radius of 10.1 cm from the beam axis, will have a depletion voltage of about 800 V after 10 years of LHC operation, if fabricated with conventional silicon, but this can be reduced to 400 V using oxygenated wafers [1]. Note that ATLAS is planning to use a layer even closer to the beam axis, the so-called "b-layer," located at 4.3 cm. Our situation is closer to the "first layer." One of the key features required for such high voltage operation is a careful guard ring design. Several multi-ring designs that fulfil this requirement have been developed [2], [3].

A.1.1.2 Radiation Hardness

Radiation induced changes in silicon sensors have been the subject of detailed studies[4]. These changes are generally divided into two classes; changes in surface properties and in bulk properties. The latter changes are generally expressed in terms of an equivalent fluence of 1 MeV neutrons. Conversion factors as a function of the particle types and their energies, known as NIEL (non ionizing energy loss) scaling coefficients, have been compiled by the ROSE collaboration [5]. Above 1MeV, protons, neutrons and pions have NIEL factors less than 1. Bulk damage effects include increased leakage current, reduced charge collection efficiency and change in effective doping concentration. This eventually leads to the so called "type inversion" in n type substrates, when their effective doping changes sign, leading to effective p-type substrates. ATLAS and CMS both have chosen a sensor technology for their pixel detectors commonly identified as n^+np^+, in which the pixels are n^+ cells on an n-type substrate and the backplane is a p^+ junction. These sensors can be operated after type

inversion at bias voltages less than the full depletion voltage. In the simpler p^+nn^+ sensors, after type inversion, if the sensor is operated at less than the full depletion voltage, then the charge spreads across many pixels, which quickly leads to a loss of position resolution and efficiency. However, a more complex sensor fabrication procedure is needed in order to provide electrical isolation between the n^+ pixels, which otherwise would be shorted together by the n-channel induced in the surface by positive charges trapped in the oxide layer.

A dedicated R&D effort towards the development of substrates capable of withstanding large radiation doses, the ROSE collaboration, made systematic studies of "defect engineering," with the goal of better performance through extended periods of heavy radiation exposure [6]. Their main results are:

1. The introduction of controlled amounts of oxygen has several advantages. In particular, it slows the change in free carrier concentration due to radiation damage.

2. Reverse annealing saturates at high proton fluence ($\geq 2\times10^{14}$ p/cm^2) and its time constant is found to be a factor of 4 larger for oxygenated wafers. This allows the detector to remain at room temperature for a longer period of time without adverse effects.

The promising results from this effort have lead the LHC experiments to consider the adoption of oxygenated silicon for the sensors used in their inner tracking systems. BTeV is already working with companies capable of producing pixel sensors from oxygenated wafers.

A.1.1.3 Radiation Levels

The simulation of the expected radiation level for the BTeV pixel sensor has been performed using the BTeV-GEANT code, including a detailed geometry of our baseline detector, including support structures and services. Figure A.1 shows the spatial distribution of the expected particle fluence. Note that the fluence falls very rapidly with radial distance from the beam axis, making the radiation damage a crucial issue only for the innermost portion of our sensors. The maximum particle fluence is $\sim 10^{14}$/cm^2/yr, assuming a luminosity of 2×10^{32}cm^{-2}s^{-1}. This corresponds to an integrated dose similar to the one quoted for the ATLAS "first layer" pixel system, located at 10.1 cm from the beam. The dominant component of radiation dose are relatively high energy pions, with a NIEL factor less than 1.

A.1.1.4 Sensor Design

The BTeV pixel cell size is 50 μm by 400 μm, where the small dimension is dictated by the needed spatial resolution. The technology chosen is n^+np^+.

Different n-side isolation techniques have been developed for double-sided silicon microstrip detectors. In particular p^+ implants, generally called "p-stops", have been implemented with various geometries. Recent developments [7] have shown that the implant

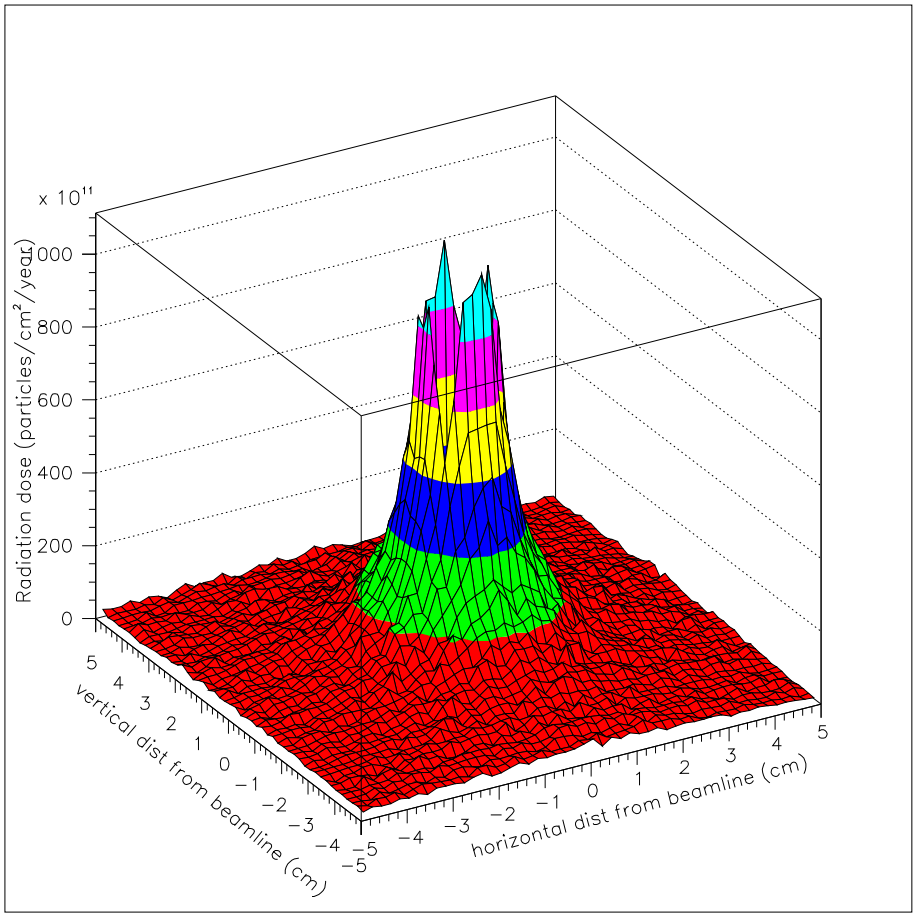

Figure A.1: Spatial distribution of the particle fluence in a pixel plane.

geometry can influence the interstrip capacitance and the noise performance. Moreover they can modulate the charge sharing between strips beyond the the spread due to diffusion.

An alternative approach, known as "p-spray", has been developed by the ATLAS collaboration. This consists of a medium dose boron implantation covering the entire n-side of the sensor. In the first implementation of this isolation technique, the ATLAS collaboration added a bias structure used for testing the sensor before bump bonding. Test beam results from ATLAS and BTeV have shown charge losses [9] in region of this bias network. A more refined solution is already implemented in new p-spray devices. We have acquired some of these new ATLAS devices, and thus will be able to verify whether they meet our specifications, both in terms of electrical performance and radiation tolerance.

We are also developing sensors of our own design. Our first effort was a joint development with the US CMS group led by B. Gobbi. We made a joint submission in Spring 1999 to two vendors, SINTEF and CSEM. These wafers contain n^+np^+ sensors with different p-stop isolation geometries. Both submissions include wafers from oxygen doped silicon.

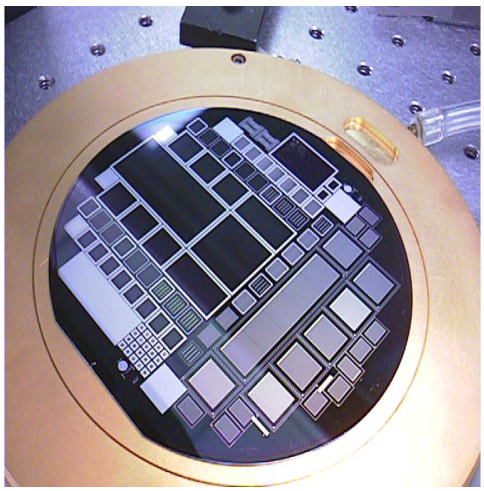

Figure A.2: SINTEF wafer from joint BTeV/CMS submission.

The specifications for the sensor prototypes in the joint BTeV-CMS submission are summarized below.

The following geometrical tolerances need to be met:

- Misalignment of p^+ implant, n^+ implant and metal layers $\leq 1.5\mu$m,
- uniformity of wafer thickness (wafer to wafer) $\pm 10\mu$m,
- thickness 300 μm,

The following electrical specifications need to be met:

- Leakage current 25 deg C $\leq$50 nA/cm^2 at 1.5$\times$ Depletion Voltage,
- resistivity 1.5-2.5 KΩ,
- breakdown voltage $\geq$ 300 V.

We have recently received the first wafers from this submission from SINTEF (see Figure A.2). Figure A.3 shows I-V curves measured for two of the smaller BTeV sensors on one of these wafers. These curves are as expected for wafer-probed pixel detectors, and show very small leakage current and high reverse breakdown voltage (500 V or higher).

We are planning to subject these devices to different types and doses of radiation. We will measure their static electrical characteristics and their signal collection properties before and after irradiation. In addition, we will investigate radiation effect on sensors bump bonded to front end electronics and study their properties in the laboratory and in beam tests.

A.1.1.5 Sensor simulation

A detailed understanding of the factors affecting the sensor performance is crucial to its design. We have studied a number of issues through simulation.

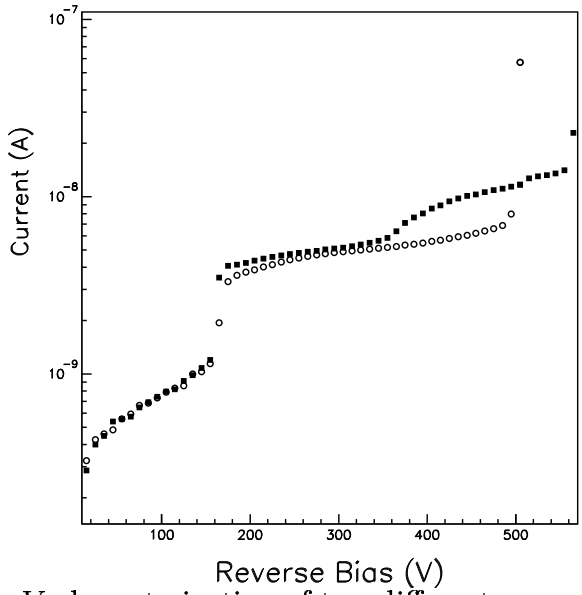

Figure A.3: $I - V$ characterization of two different sensor cells on a SINTEF wafer recently received at Fermilab.

In an n^+np^+ detector, the charge carriers collected at the pixel electrodes are electrons. We have simulated the properties of these n^+np^+ sensors, as well as more conventional p^+nn^+ pixel devices, which have holes as the collected charge. In addition, we have considered radiation damage effects. These include increased leakage current and the change in charge collection efficiency induced by the change in the effective donor concentration.

Other factors that affect the ultimate resolution achievable in this system are related more closely to the design approach and the performance of the readout electronics. In particular, the electronic noise, and the threshold that determines the minimal charge deposition that will be recorded as a signal hit, are important. The sensitivity to these parameters has been studied, as well as the tradeoff between analog and digital readout.

In order to understand these effects, we have developed a stand-alone simulation, based on a two-dimensional model of the signal formation in silicon. This program has been interfaced with the Monte Carlo software used to study our physics reach. This integration has been used to predict detector occupancy, crucial in trigger simulation, and to determine the required readout bandwidth. We have validated some of our results by comparing them with our recently acquired test beam data (see next section).

A.1.1.6 Spatial resolution studies

Our approach to silicon sensor modeling [10] is similar to previous studies performed for silicon microstrip detectors [11], [12]. We have investigated the interdependence of charge diffusion, magnetic field effects, electronic noise, discriminator threshold and number of bits in the back-end electronics.

The ability to achieve a spatial resolution better than the nominal "digital" resolution (σ=width $/\sqrt{12}$) is closely related to how accurately we can interpolate between the location of the centers of individual pixels using information on measured charge on each pixel in a

cluster.

We have modeled the signal induced by minimum ionizing tracks traversing silicon using a charge straggling distribution function supported by experimental data and a detailed theoretical model of the interactions responsible for the energy loss in silicon [13]. The detector has been divided into 30 μm thick slices to model fluctuations in the energy deposition along the path of the charged particle.

Electrons and holes produced by the energy deposited by a traversing charged particle drift along the electric field lines ($\vec{E}$) in the detector. The equations describing this drift motion are:

$$\vec{J_n} = q\rho_n\mu_n\vec{E} \tag{A.1}$$

$$\vec{J_h} = q\rho_h\mu_h\vec{E} \tag{A.2}$$

where q is the electron charge, μ_n and μ_h are the mobility of electrons and holes respectively, ρ_n is the number of free electrons per unit volume, and ρ_h is number of free holes per unit volume.

In parallel, the charge cloud spreads laterally due to diffusion. The parameters characterizing the drift in the electric field (μ_h, μ_e) are related to the parameter describing the diffusion of the charge cloud (D_h,D_e) by the Einstein equation:

$$D_{h(e)} = \frac{kT}{q}\mu_{h(e)} \tag{A.3}$$

where D_h and D_e are the diffusion coefficients, q is the electron charge and kT is the product of the Boltzmann constant and the absolute temperature of the silicon. The average square deviation with respect to the trajectory of the collected charge without diffusion is $< \Delta r^2 >= 2D\Delta t$. In our study we have used $\mu_h = 400\ cm^2/Vs$, $\mu_e = 1450\ cm^2/Vs$.

When the silicon detector is located inside a magnetic field, there is an additional source of charge spreading; the lateral motion induced on electrons and holes by the magnetic field. This effect shifts the centroid of the detection point of the charged cloud and also widens it, because the amount of drift is proportional to the path length of the detected electrons (holes). This so called "$E \times B$ effect" depends on a parameter called the Hall mobility, μ_H, which is proportional to the charge carrier mobility discussed above. In order to take into account the effect of the magnetic field in the bend plane, the following values of the Hall mobility have been taken from experimental data quoted in [14]:

$$\mu_{H,h} = 0.72\mu_h, \tag{A.4}$$

$$\mu_{H,e} = 1.15\mu_e. \tag{A.5}$$

The charge-cloud image appears on more pixels when the incident track crosses the detector at an angle, as the generation points of the electron-hole pairs spread out along the track pathlength. These various effects are illustrated in Figure A.4, which shows the charge broadening due to diffusion, the magnetic field and the combination of the these two effects together with track inclination with respect to the normal to the detector.

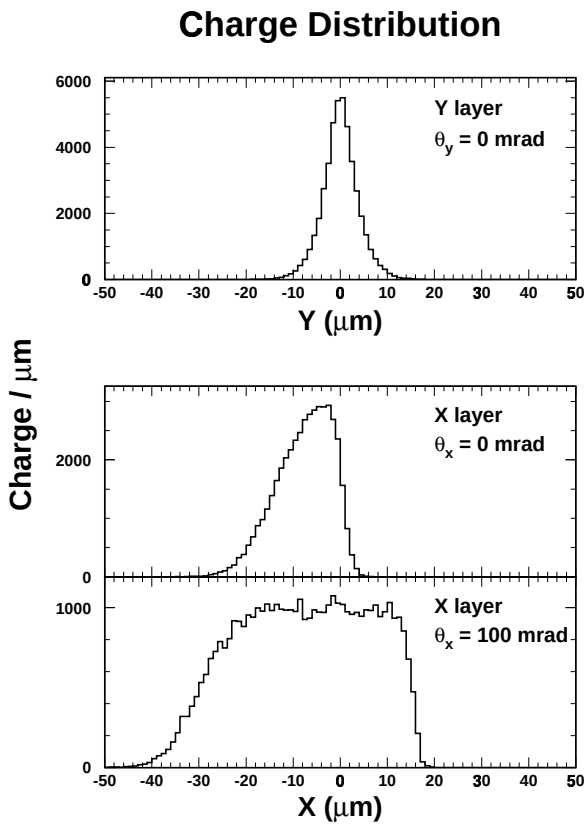

Figure A.4: Collected charge spreading in a 300 μm silicon detector a) produced by diffusion, b) produced by the interplay of diffusion and the magnetic field for B=1.6T, and c) produced by diffusion and magnetic field effects when the charged track is incident at an angle of 100 mr in the bend plane.

An analog readout improves the spatial accuracy through the use of charge weighting. low intrinsic noise is obviously a key element in this approach, together with a low and uniform threshold.

Two assumptions are common to all the configurations used in our study of the interdependence between threshold, noise and digitization accuracy . We have considered a 300 μm thick Si detector biased in over-depleted mode (200 V for a detector that is fully depleted at 120 V). We have assumed full charge collection and negligible capacitive cross talk between adjacent pixels. These assumptions will be relaxed in future studies.

A.1.1.7 Factors affecting the spatial resolution

We have carefully examined the various factors affecting the hit resolution in the small pixel direction, both in the bend plane and in the direction orthogonal to it, with reference to a pixel geometry of 50μm $\times$ 400μm, using several track orientations.

Figure A.5 shows the relationship between the position of incidence at the pixel plane and the reconstructed coordinate for tracks at normal incidence on the pixel detector, whereas Figure A.6 assumes a track inclined at an angle $\theta_x = 300mr$. We have started our study assuming a readout scheme with the intrinsic electronic noise switched off, and we consider both a binary and an analog readout (with 6-bit ADC resolution). We can see that if the electronics noise is negligible, a digital readout actually can achieve a better resolution than the naive expectation of the width of the cell divided by $\sqrt{12}$. This is due to the fact that when the charge is shared between two or more pixels it is possible to do a digital charge weighting algorithm that provides some interpolation between the position of individual pixels.

Let us start our discussion of analog readout with tracks at normal incidence. Figure A.5 shows that, in the presence of a magnetic field, the charge can actually be "focused" inside the pixel instead of spread out by virtue of the magnetic field. This makes the analog and digital readout equivalent, because there is not a second pixel helping to interpolate the track position using charge sharing. On the other hand, tracks incident on the pixel region where the magnetic field spreads the charge further with respect to diffusion, are helped significantly by analog readout. In order to take full advantage of the analog information, it is necessary to adopt an optimal choice of the charge weighting algorithm that reflects the expected distribution of the charge profile. In particular, for tracks incident at very small angles, it is necessary to perform a non-linear weighting [12].

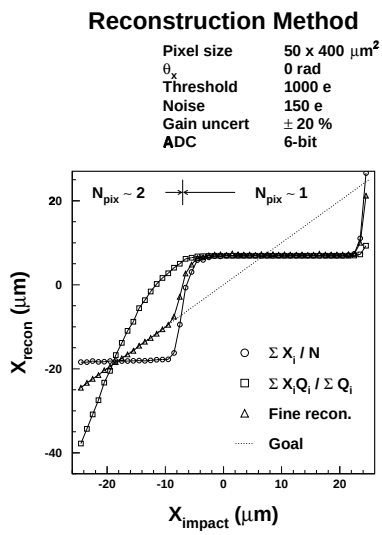

Figure A.5: The reconstructed x coordinate as a function of the charged track impact point on the pixel cell in a 1.6 T magnetic field, for a pixel size of 50x400 μm^2, and normal incidence. Both these coordinates are measured with respect to the pixel center.

An additional important constraint in the achievable resolution is the discriminator threshold. In this study we have assumed that only the pixels having a signal above threshold

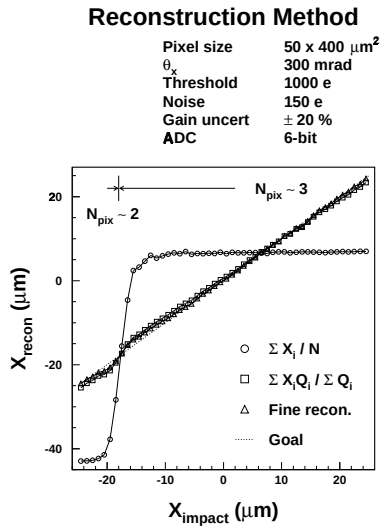

Figure A.6: The reconstructed x coordinate as a function of the charged track impact point on the pixel cell in a 1.6 T magnetic field, for a pixel size of 50x400 μm^2, and incidence angle in the bend plane θ_X = 300 mr. Both these coordinates are measured with respect to the pixel center.

are read out, and we have varied the threshold for analog and binary readout. Figure A.7.a shows the effect of increasing the threshold for an incident angle $\Theta_x = 300$ mr, for analog and digital readout respectively. Figure A.7.b shows the corresponding pixel occupancy. Each curve shows the fraction of events having N pixels hit for a given threshold. For instance, for a threshold of 1000 electrons, essentially all events have either two or three pixels above threshold, with $\sim$ 60% 3-pixel clusters, and 40% 2-pixel clusters. The resolution achievable for binary readout shows a characteristic oscillatory behavior as we change the threshold. The worst resolution is always at the thresholds for which most of the events have clusters with the same size, corresponding to less interpolation power. In the analog readout case, the higher the threshold, the coarser is the charge sharing process.

The slope of the threshold dependence of the resolution is not very high below 3000 electrons, as illustrated by Figure A.7.

Figure A.8 shows the number of pixels hit as a function of the track angle for electron and hole collection. Figure A.9 shows the resolution as a function of the angle in the bending plane (θ_x), and in the non-bend plane (θ_y) expected with digital readout and with a 4 bit ADC respectively. At angles above $\pm$50 mr the resolution achieved with analog readout is significantly better.

An understanding of the resolution and occupancy expected for a given sensor and readout electronics choice is very important to optimize the performance of the final system. In

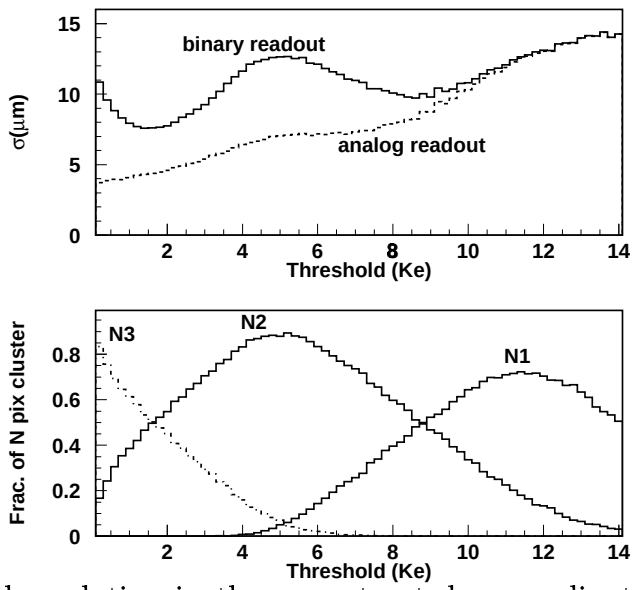

Figure A.7: a) Spatial resolution in the reconstructed x coordinate as a function of the threshold for a pixel size of 50x400 μm^2 and incidence angle in the bend plane $\theta_X = 300$ mr. b) percentage of events having N pixels hit as a function of the threshold for the same configuration.

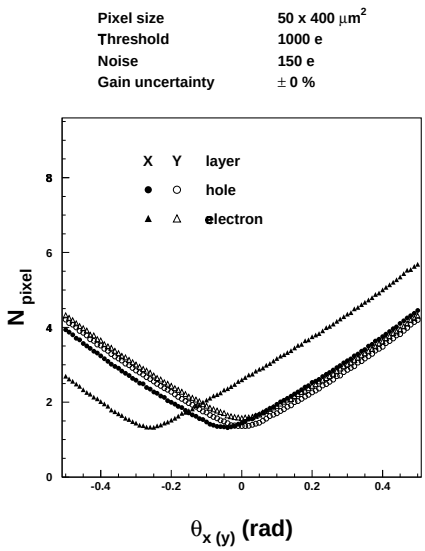

Figure A.8: Number of pixels hit for a 50 μm pixel small dimension as a function of the track orientation. The magnetic field is parallel to the $\hat{x}$ direction.

order for this tool to be effective, its accuracy must be checked with experimental data. We have done a systematic study of the performance expected from various sensor and readout

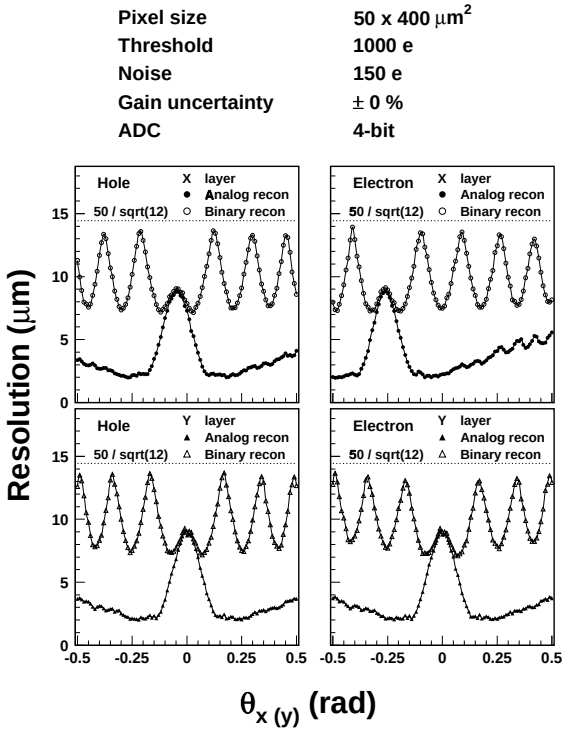

Figure A.9: Resolution for binary readout and 4-bit ADC readout for 50 μm pixel small dimension. The magnetic field is parallel to the $\hat{x}$ direction.

electronics combinations used in the test beam run recently completed. Details on the data taken and the analysis procedure will be given in the next section. The comparison between predicted and measured resolution is shown in Figures A.18 and A.19 for two different digitization accuracies (8 bits and 2 bits) and different thresholds. The agreement is very good, if we take into account that effects like imperfect alignment, track projection errors and angular resolution are so far neglected. We will introduce them in a Monte Carlo simulation of our beam set-up presently under development.

A.1.1.8 Occupancy studies

An additional application of our sensor model is a more accurate information on the hit multiplicity associated with a given track angle. We have used this information to achieve a better understanding of several key features of our detector performance.

We have investigated[15] the occupancy in the inner portion of our detector for different event classes and different assumptions on the interaction rate using GEANT. This study has been a crucial input for the engineering group responsible for the design of the pixel readout chip and to test the readout architecture and identify possible bottlenecks in the

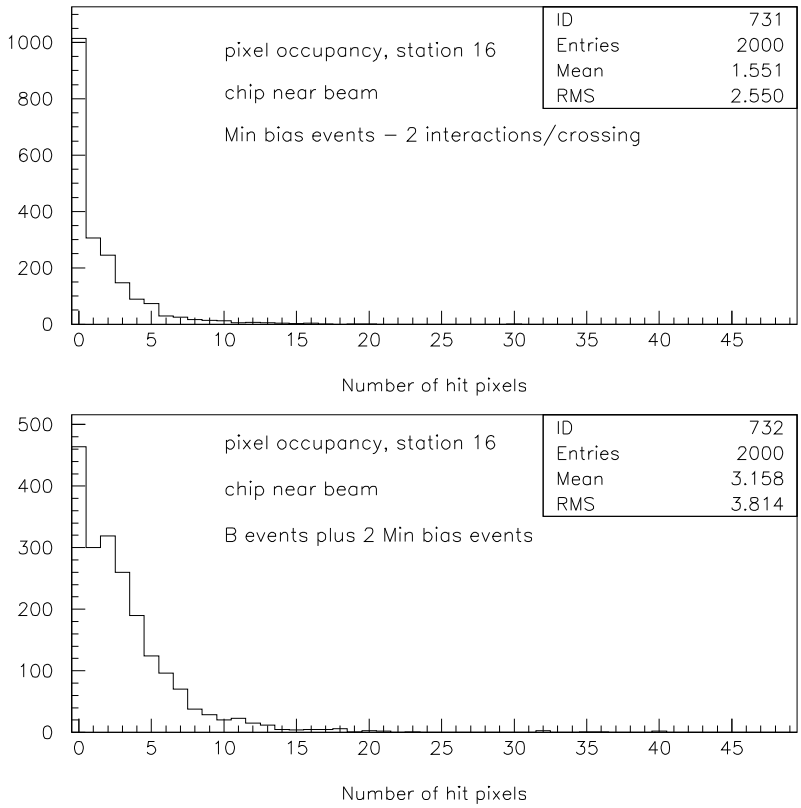

Figure A.10: Number of pixels hit per crossing in the hottest pixel readout chip (nearest to the beam). The upper histogram shows the occupancy expected at a luminosity of $2\times10^{32}\text{cm}^{-2}\text{sec}^{-1}$. The lower histogram shows the occupancy expected in b events at this luminosity.

data throughput. The pixel occupancy has been studied for a chip located with its inner edge 6mm from the beam pipe. The chip has been assumed to be 12 mm $\times$ 12 mm, with a 50 μm $\times$ 400 μm pixel cell. The results are shown in Figure A.10, based on an expected luminosity of 2×10^{32} cm^{-2}s^{-1}.

This study also provides data samples for the readout architecture simulation and the trigger processor generator. Initial studies have shown that, assuming a pixel size of 50 μm x 400 μm and 3 bit flash ADC's digitizing the pixel cell signal, the proposed column-based data-driven architecture should be capable of achieving the hit readout rate required by the BTeV experiment [16].

A.1.1.9 Assessment of the Sensor Performance

The characterization program that will enable us to finalize the design of our sensor includes laboratory measurements and beam tests. We successfully started this research program with p-stop and p-spray sensors of ATLAS design. We have studied the I-V performance of the detectors bump-bonded to FPIX0 and FPIX1 readout chips. Our measurements show that the static properties of these sensors are quite good prior to irradiation.

The results obtained through the large sample of data acquired in an extensive test beam run at Fermilab is discussed in the following section.

This summer we will start a program of irradiation of detector samples. We will start by exposing selected samples to a Co source and measuring the I-V curve following irradiation. Samples will also be exposed to a neutron beam. This will allow us to measure the change in leakage current and breakdown voltage. It is also very important to determine the change in collection properties upon irradiation. To this purpose we are planning to use the transient current and charge technique developed at BNL by V. Eremin, N. Strokan, E. Verbitskaya and Z. Li [17]. These techniques are based on the analysis of the current and charge pulse shapes which arise when carriers are produced inside the electric field region inside the material under study. These techniques have been shown to provide the most accurate measurement of the effective carrier concentration at high radiation dose and to measure carrier drift mobility.

When radiation hard electronics will be available we will complete our study by irradiating samples of detectors bump bonded to readout electronics. It is important to proceed in a systematic fashion to identify potential problems.

A.1.1.10 Interface with other R& D efforts

We have engaged in several collaborative efforts with other groups pursuing the development of sensors that meet our requirements. In particular, we are engaged in joint submissions with the US-CMS and ATLAS pixel groups and we have acquired samples of the ATLAS p-stop and p-spray devices.

We are particularly interested in the ATLAS development effort as the unit cell geometry of their choice matches our needs quite well. We will investigate how close these sensors come to satisfying our needs and we will develop our strategy for future submissions accordingly.

Some of us have also joined the ROSE collaboration and we will adopt any proven technological solution that will emerge from their work. Lastly, we are in close contact with the solid state sensor development group at BNL and we are planning collaborative efforts to develop a deeper understanding on some of the key issues affecting sensor optimization.

A.1.2 Test Beam Results

A.1.2.1 Introduction

A test of several pixel detectors was performed in the Fermilab MTest beam line during the fixed target run of 1999-2000. The purposes of the beam test were to:

- Gain operational experience with pixel detectors, utilizing both p-stop and p-spray varieties of ATLAS sensors, and look for potential problems and sensitivities in the use of pixel detectors for BTeV.
- Determine the spatial measurement resolution of 50 μm $\times$ 400μm pixel elements as a function of particle angle of incidence, number of readout bits describing the charge deposited in each pixel element, sensor bias, readout threshold, and combinations of these parameters.
- Determine the validity of our sensor simulations as predictors of pixel detector performance for future hardware choices.

The beam test was successful in all these aims. The main results are summarized in the body of this proposal. In the following pages, we describe the experimental setup, and present some of the results in greater detail.

A.1.2.2 Pixel Devices Tested

The pixel detectors tested are all from the "first ATLAS prototype submission [18]," and all have 50 μm $\times$ 400 μm pixels. Two of the sensors come from a single wafer manufactured by CiS, and the other three are from a single Seiko wafer. The CiS sensors (one p-stop "ST1" and one p-spray "ST2") were indium bump bonded to FPIX0 readout chips by Boeing North America. FPIX0 is the first generation pixel readout chip developed at Fermilab. Its primary purpose was to establish a front end design appropriate for use at the Tevatron collider with 132 ns between crossings. The FPIX0 readout pixel was designed to match the sensor pixel size of the ATLAS prototypes, but FPIX0 is much smaller than a prototype "single chip" sensor. The instrumented portion of the sensor is 11 columns $\times$ 64 rows. Each FPIX0 readout pixel contains an amplifier, a comparator, and a peak sensing circuit. When any comparator fires, a CHIP_OR signal is asserted. FPIX0 provides a zero-suppressed readout of hit pixels. The information read out consists of hit row and column numbers, together with a voltage level which is proportional to the peak pulse height recorded by the peak sensing circuit in the hit cell. For this beam test, the analog output was connected to a buffer amplifer mounted next to the pixel detector. The output of the buffer amplifier was digitized by an 8-bit flash ADC.

The Seiko sensors (two p-stop ST1's and one p-spray ST2) were indium bump bonded to FPIX1 readout chips by Advanced Interconnect Technology Ltd. (AIT). FPIX1 is the second generation of pixel readout chip developed at Fermilab, and is the first implementation of a high speed readout architecture designed for BTeV. Each cell contains an amplifier very

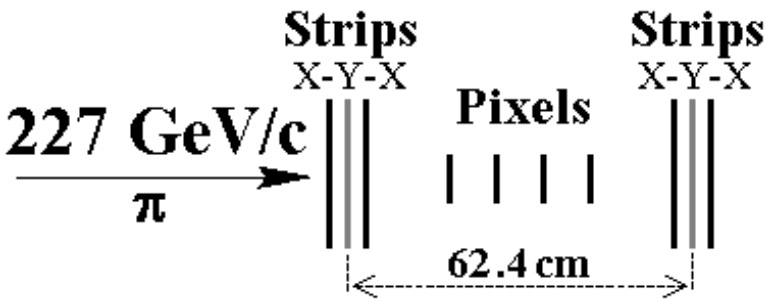

Figure A.11: Schematic drawing of the silicon telescope.

similar to the FPIX0 amplifier. Instead of a single comparator and a peak sensing circuit, each FPIX1 cell contains four comparators, which form a 2-bit flash ADC. FPIX1 is much larger than FPIX0. It contains 18 columns of 160 rows, and is the same size as the ATLAS single chip sensors. However, a minor design error limits the number of rows which may be read out to $\sim$ 90 per column.

A.1.2.3 Experimental Setup

All data described here were collected using a 227 GeV/c pion beam. This was the highest momentum available in the MTest beamline, and was chosen to minimize multiple scattering. The pixel devices under test were located between two stations of single sided silicon strip detectors (SSD's) as shown in Figure A.11. The pixel detectors were mounted on printed circuit boards which fit tightly into slots machined in an aluminum box. The box was connected rigidly to the mechanical support structure for both SSD stations. A number of slots were provided in the pixel box which allowed detectors to be positioned normal to the incident beam direction. One set of slots allowed a single detector to be positioned at angles of 5, 10, 15, 20, and 30 degrees with respect to the beam direction. Up to four pixel detectors were tested in the beam at one time. As is discussed below, at this point in our analysis, there is a small uncertainty of 1-2 degrees in the overall rotation of the SSD telescope and pixel test box with respect to the incident beam direction. The pixel detectors were oriented so that the 50 μm pitch measured the horizontal (X) coordinate. Each silicon microstrip station contained two planes which measured the X coordinate, and one plane which measured the vertical (Y) coordinate. Three of the four X-measuring microstrip planes were 20 μm strip pitch. The remaining X-plane, and the two Y-planes were 25 μm strip pitch. The silicon microstrip detectors were read out using SVX-IIb ASIC's [19]. Because of common mode noise problems, the sparse-scan feature of the SVX-II was not used (every strip was read out). The extrapolation accuracy of this silicon microstrip telescope at the pixel detectors under test was $\sim$ 2.1 μm for tracks with shared charge in adjacent SSD channels.

The readout was triggered by the coincidence of signals from two 15 cm $\times$ 15 cm scintillation counters, positioned upstream and downstream of the silicon telescope and separated from each other by about 10 m. In order to select tracks incident on the active area of the

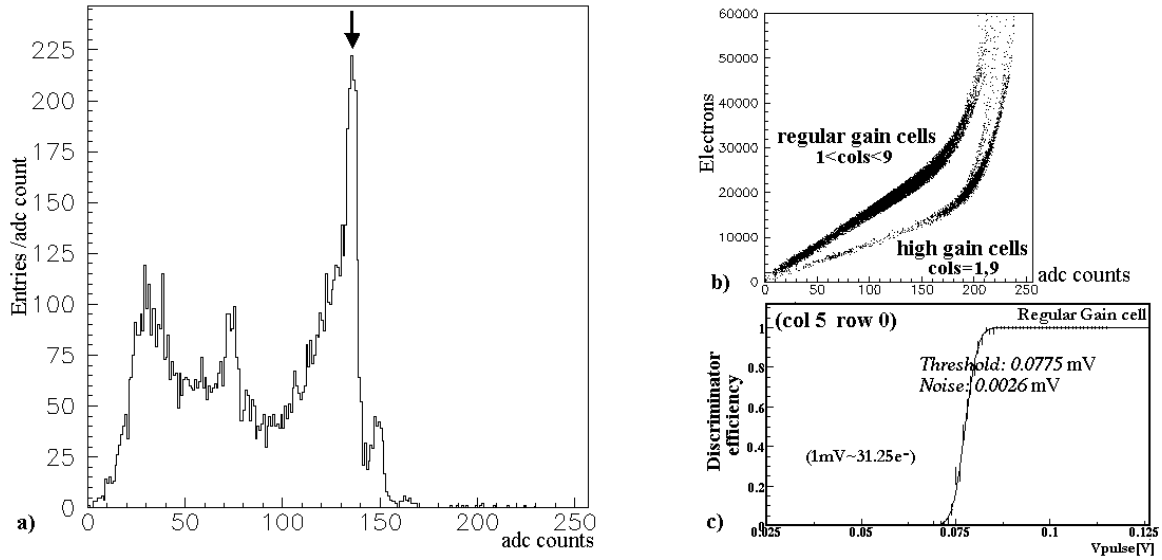

Figure A.12: Calibration for the FPIX0 p-spray (CiS) sensor. Plot a) shows a Tb x-ray spectrum. The arrow indicates the K_α peak. Plot b) shows the pulser calibration data for all channels, and plot c) shows a discriminator threshold curve for a single channel. Curves like the one shown in c) are used to determine the amplifier noise and discriminator threshold dispersion.

pixel detectors, the FPIX0 p-stop CHIP_OR output signal was also required in coincidence with the scintillator signals. The data acquisition system was based on VME, adapted from the CDF SVX test stand. The typical event size was $\sim$ 6.3 Kbyte, more than 6.1 Kbyte of which was the unsparsified SSD data. The DAQ system was able to record about 800 events per spill. A total of about 3,000,000 useful events were collected.

A.1.2.4 Calibration

The pixel detectors were calibrated using a pulser and two x-ray sources (Tb and Ag foils excited by an Am α emitter). The threshold efficiency curve and the analog pulse response for each cell were determined by injecting charge through the integrated calibration capacitance in each FPIX cell, and sweeping the injected pulse amplitude in small steps. For FPIX0-instrumented detectors, the absolute calibration of the discriminator thresholds, amplifier noise, and ADC scale, were established by measuring the ADC peak of the known K_α line of the sources. Figure A.12 illustrates the calibration of the FPIX0 p-spray sensor.

FPIX0 contains two types of amplifiers, "high gain" and "standard gain." For most of the data taking, the discriminator threshold for the FPIX0 p-stop was set to a voltage equivalent to 2500$\pm$400 e^- for the standard gain cells, and 1500$\pm$230 e^- for the high gain cells. For the FPIX0 p-spray device the corresponding thresholds were typically 2200$\pm$350 e^- and 1250$\pm$160 e^-. The amplifier noise was measured to be 105$\pm$15 e^- for standard gain

cells, and 83±15 e^- for for high gain cells of the FPIX0 p-stop sensor. The corresponding noise values for the FPIX0 p-spray sensor were 80 ±10 e^- for standard gain cells, and 67±8 e^- for high gain cells. In addition, we found an equivalent charge noise due to the external buffer amplifier and ADC of 400±150 e^- for FPIX0 p-stop standard gain cells, and 205±95 e^- for FPIX0 p-stop high gain cells. The corresponding external noise values for the FPIX0 p-spray sensor were 185±20 e^- and 100±20 e^-.

The calibration of the four thresholds input to the FPIX1 chips (one for each comparator in the 2-bit FADC implemented in every cell) and the amplifier noise measurement for FPIX1-instrumented detectors, was done by sweeping the thresholds and measuring the differential counting rate due to the x-ray source. We found a set of four average threshold values in nominal running conditions for the FPIX1 p-stop of about $3780e^-, 4490e^-, 10290e^-$, and $14680e^-$, with a spread of about $380e^-$. The amplifier noise was measured to be $110 \pm 30e^-$. The quoted spread refers to channel to channel variation on a single chip and is an rms value.

It should be noted that FPIX1 can be operated successfully at very low threshold. We are currently doing bench tests with an ATLAS tile-1 sensor, bump bonded to five FPIX1 chips, and read out through a prototype "High Density Interconnect" (HDI) flexible circuit. This test module can be operated without oscillation with discriminator threshold set below 1500 e^-. The FPIX1 sensor hybrids that we tested in the beam were mounted on a printed circuit board which was designed for bench tests. In order to interface this board to the readout system which we designed for FPIX0, we fabricated a daughter board which was mounted on the FPIX1 printed circuit board. This arrangement suffered from noise and pickup problems that we never fully overcame. Consequently, we were not able to test the FPIX1-instrumented sensors in the beam with very low discriminator thresholds.

A.1.2.5 Charge collection

Charge collection can be studied in detail for the FPIX0 instrumented sensors, thanks to the 8-bit analog information, and the absolute calibration provided by the use of x-ray sources. The measured pulse height distributions were fit using a Landau function convoluted with a Gaussian [20]:

$$f(E) = N \int_{-\infty}^{+\infty} dE' \frac{e^{-\frac{(E-E')^2}{2\sigma_g^2}}}{\sqrt{2\pi\sigma_g^2}} \frac{\phi(\frac{E'-E_{mp}}{\xi} + \lambda_0)}{\xi} \tag{A.6}$$

In this expression, N is a normalization constant, $\frac{\phi(E')}{\xi}$ is an ordinary Landau function, with $\lambda_0 = -0.223$, so that E_{mp} is the most probable energy loss[1], and σ_g is the standard deviation of the Gaussian function. The Landau curve is derived in the literature assuming that the energy loss is due to Rutherford scattering between the charged particle and free electrons. The Gaussian takes into account the smearing due to the bonding of electrons in the silicon crystal, and to the finite resolution of the detector and readout electronics. The fit is done with N/ξ, E_{mp}, ξ, and σ_g as free parameters (P1, P2, P3, and P4 in the fit), using the energy

[1]When $E' = E_{mp}$ the function $\phi(\lambda)$ reaches its maximum; the Gaussian shifts the maximum only by a small amount.

required to create an electron-hole pair in silicon (3.6 eV) to convert energy in eV to charge in e^-.

Figures A.13a and A.14a show the pulse height distributions for the FPIX0 p-spray and p-stop detectors respectively. The "improved Landau" function fits the experimental data quite well, except that there is an obvious peak at low pulse height in Figure A.13a, indicating charge collection inefficiency in the p-spray sensor, and a bump at $\sim$ 50000 e^- in Figure A.14a, which is due to saturation of the off-chip buffer amplifier/ADC combination. Figure A.13b shows that the p-spray sensor suffers sizeable charge collection inefficiency between columns, especially on the column boundaries which include the "punch-through biasing" network. Our measurement of this charge loss[2] is consistent with previous measurements made by the ATLAS pixel collaboration[21]. Figure A.14b shows the spatial distribution of the tracks for which the charge collected in the FPIX0 p-stop sensor is less than 15000 e^- (under this value the Landau distribution predicts a very small fraction of events). This plot shows that the p-stop sensor also suffers from a very small amount of charge collection inefficiency, and that this inefficiency is concentrated at the four corners of the sensor pixels.

We find that the charge collected by the CiS p-spray sensor is about 24% less than the charge collected by the p-stop sensor. This measurement is also in agreement with the ATLAS test beam results [21]. The most probable and average charge collected are respectively 20000$\pm$70 e^- and 23100$\pm$70 e^- for the CiS p-spray sensor[3]. For the CiS p-stop sensor, the most probable charge collected is 24730$\pm$30 e^-, and the average charge collected is 30100$\pm$30 e^-.

A.1.2.6 Charge Sharing

As is discussed above in the pixel sensor simulation section, the charge deposited by a single track is often shared by more than one pixel. The amount of charge sharing is determined by geometry (the number of cells crossed by the track), and by diffusion of the electrons drifting in the silicon. The fraction of the time that each cluster size is observed (for the regular gain cells of the FPIX0 p-stop sensor) are listed in table A.1. The data show clearly the dominance of two cluster sizes for each incident beam angle, as expected from geometry.

For each angle, we studied the influence on charge sharing of different detector bias voltages and readout discriminator threshold settings (see Figure A.15). Since charge-sharing is determined primarily by geometry at large track angles, the effect of changing the bias voltage is negligible for track angles of 10 degrees and above. However, at small angles, for which charge sharing is primarily a function of electron diffusion, lower detector bias increases charge-sharing. As expected, the discriminator threshold is important at all track angles; lower threshold always translates directly into more charge sharing.

[2]These charge losses are not intrinsic to the p-spray technology, but are a feature of this particular sensor design. The ATLAS pixel group has reported that their new p-spray sensor has charge collection properties very similar to what we observe for the CiS p-stop sensor.

[3]This measurement is done using only tracks far away from the inter-pixel boundary.

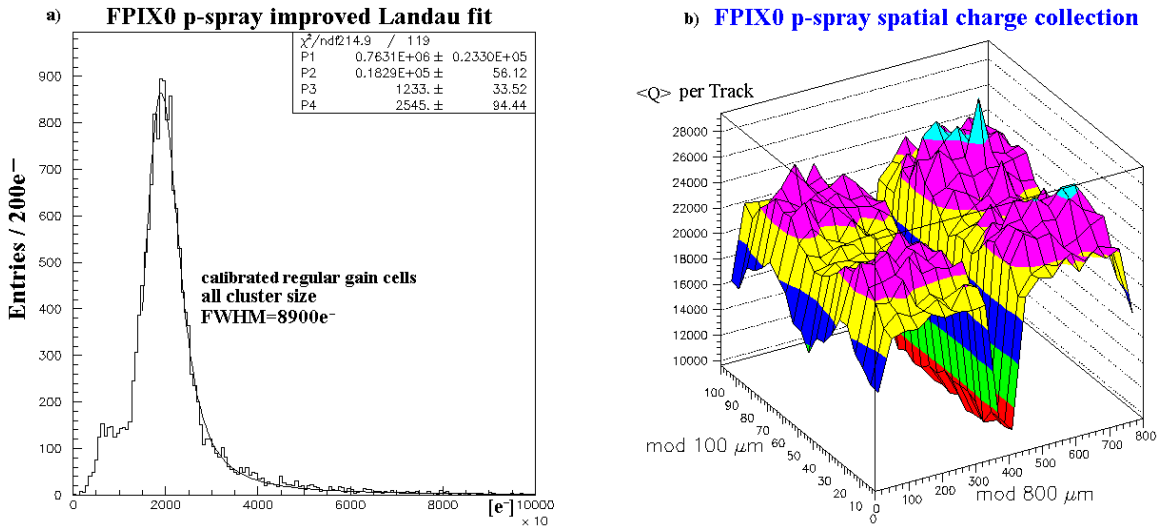

Figure A.13: The plot on the left shows the "improved Landau" fit of the pulse height distribution for the CiS p-spray sensor bump-bonded to an FPIX0 chip, when the track is at normal incidence. The plot on the right shows the average charge collected as a function of track position.

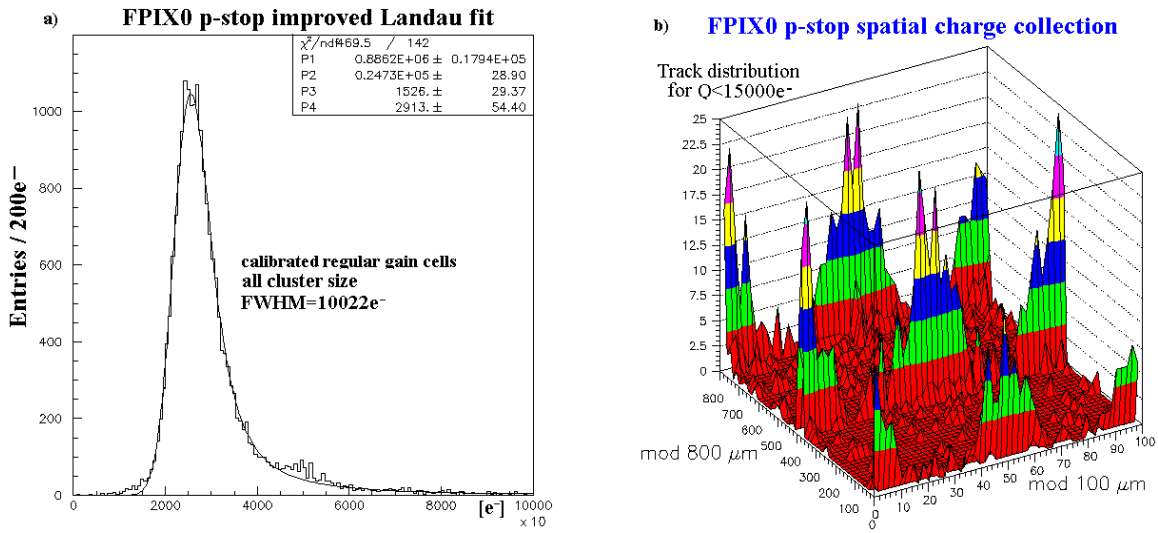

Figure A.14: The plot on the left shows the "improved Landau" fit of the pulse height distribution for the CiS p-stop sensor bump-bonded to an FPIX0 chip, when the track is at normal incidence. The plot on the right shows the distribution of tracks that leave a signal less than 15000 e^- in the detector.

A.1.2.7 Spatial Resolution

The tracks used to study pixel resolution were fit using data from the SSD telescope and from pixel detectors other than the device under test, using a Kalman-filter [22]. The prediction

[degs]	CS=1	CS=2	CS=3	CS=4	CS=5	$CS \geq 6$
0	.639±.0034	.328±.0033	.017±.0010	.009±.0019	.0034±.0004	.0025±.0004
5	.433±.0035	.527±.0035	.022±.0011	.010±.0011	.0041±.0004	.0028±.0004
10	.090±.0018	.846±.0025	.040±.0016	.015±.0009	.0055±.0005	.0029±.0005
15	-	.635±.0034	.332±.0034	.022±.0011	.0080±.0007	.0034±.0004
20	-	.209±.0027	.741±.0030	.031±.0014	.0124±.0009	.0060±.0006
30	-	-	.178±.0024	.769±.0029	.041 ±.0018	.0115±.0009

Table A.1: Cluster size fraction for various angles of incidence for FPIX0 p-stop regular gain cells. For each angle, the sample size is about 20000 tracks. These data were collected with a sensor bias voltage of -140 V, and a discriminator threshold of 2500 e^-.

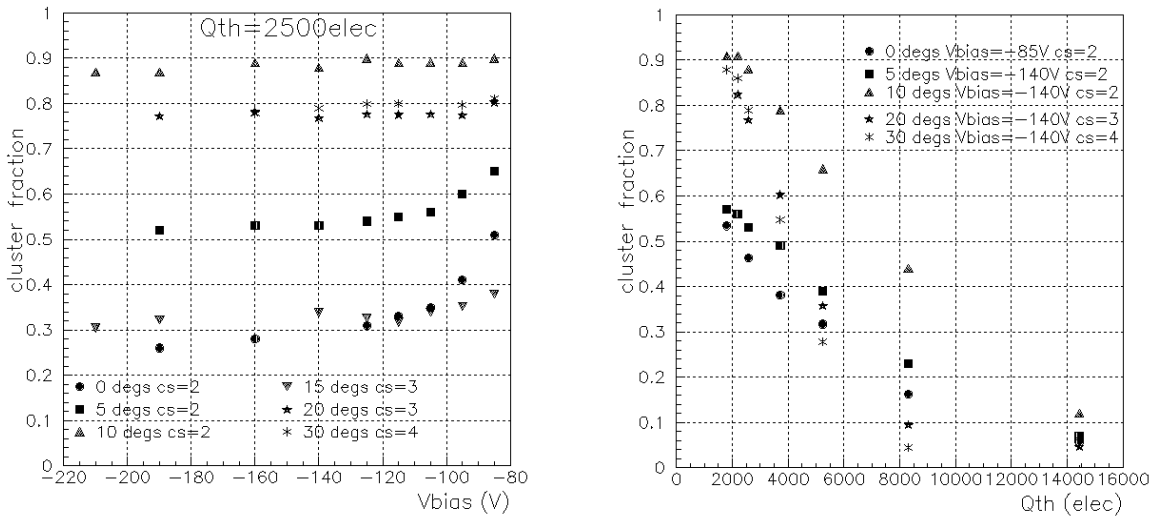

Figure A.15: The plot on the left shows the fraction of the time that the indicated cluster size was recorded as a function of detector bias for a fixed readout threshold and a variety of angles. The plot on the right shows the same fraction as a function of the detector readout threshold for a fixed bias voltage and a variety of angles. These data were recorded by the p-stop FPIX0 detector, which has a depletion voltage of ∼-85V.

error at the pixel device under test varied, depending on the cluster width (and therefore the measurement precision) of each of the points included in the fit, and on the number of pixel planes in the test setup for a given data set (and therefore the amount of multiple scattering). For the bulk of the data taking, two pixel planes were tested at a time. In this configuration, the average extrapolation error along the short pixel dimension (X) was about 2.5 μm. The prediction error was reduced to 2.1μm if tracks were required to have cluster size two in both the most upstream and the most downstream X-measuring SSD planes.

No projection error has been subtracted from the measurement resolutions reported here.

For all angles except 30 degrees, the results presented were obtained by demanding cluster size two in the most upstream and downstream X-measuring SSD planes. Less data were collected at 30 degrees than at the other angles. Consequently, no cluster size cut was made in the analysis of the 30 degree data.

The coordinate measured by a pixel detector is given by the position of the center of the cluster of hit pixels associated with a track, plus a correction (conventionally called the η function) which is a function of the charge sharing, the cluster width, and the track angle. For this analysis, we have used a "head-tail" algorithm for computing the η function, which ignores the charge deposited in pixels on the interior of a cluster, and uses only the charge deposited on the edges of the cluster. The histogram on the left side of Figure A.16 shows the distribution of $\eta = \frac{(q_R - q_L)}{(q_R + q_L)}$, where q_R is the charge measured in the "right" hand pixel in a cluster of two, and q_L is the charge measured in the "left" hand pixel in the cluster, for data taken with beam normally incident on the FPIX0 p-stop sensor. The asymmetry of this distribution indicates that, in fact, there was a small angle between the beam and the normal to the pixel detector. The plot on the right shows the difference between the predicted X position (in the plane of the pixel detector) and the edge between the two hit pixels (the "digital position"), as a function of η. The η function for cluster size two and normal incidence is the function required to make this distribution a constant, with an average value of zero. For each detector, we have determined a set of η functions using plots like the one shown on the right hand side of Figure A.16.

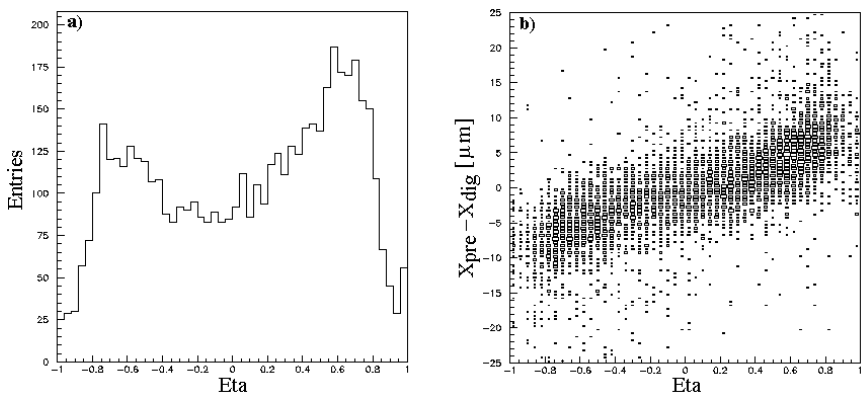

Figure A.16: The histogram on the left is the η distribution for data collected with beam normally incident on the FPIX0 p-stop sensor. An entry is made in this histogram only if exactly two adjacent pixels in a single column are hit. The plot on the right shows the difference between the predicted track X-position and the position of the edge between the two hit pixels, as a function of η for the same data.

The residual distributions for the FPIX0 p-stop detector, for data taken with V_{bias} = -140V, and Q_{th} = 2500 e^-, are shown in Figure A.17. Each residual distribution is fit to a Gaussian (shown superimposed in Figure A.17). Clearly, the residual distributions are not Gaussian. This is true especially at zero and five degrees, where no charge sharing

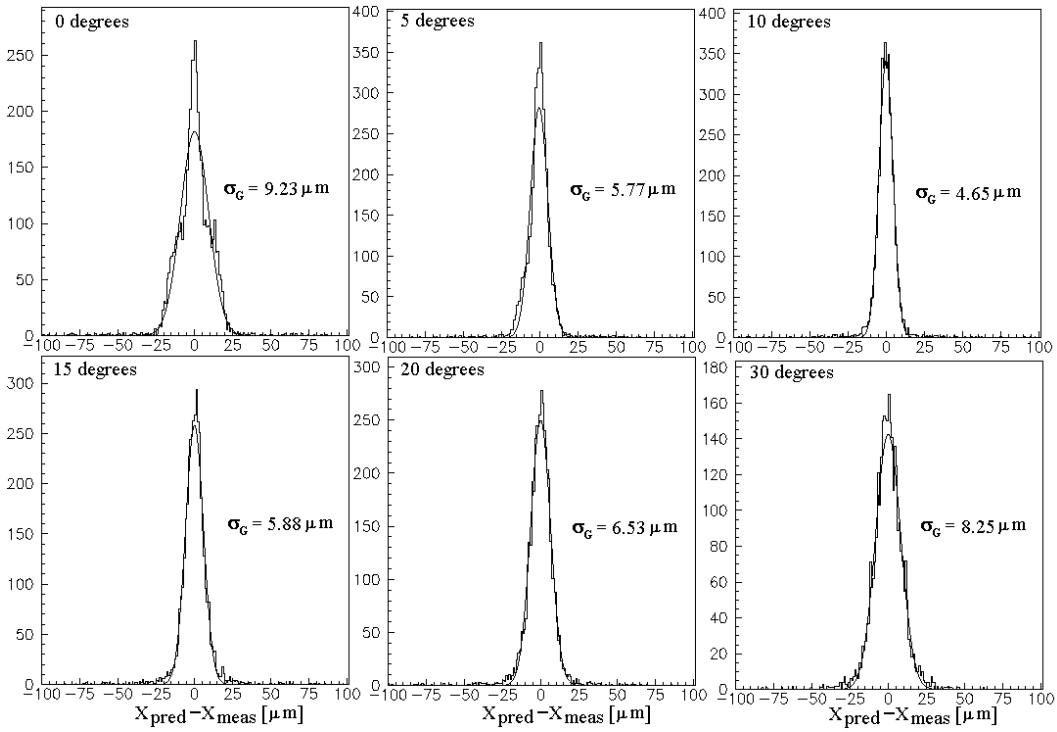

Figure A.17: Residual distributions for the FPIX0 p-stop detector. σ_G is the standard deviation of the Gaussian fit to each residual plot.

information is available a significant fraction of the time, since only one pixel is hit. The residual distributions also have more entries far from zero than the Gaussian fits. These "tails" are due to the emission of δ-rays, and are discussed below. Nonetheless, the Gaussian standard deviations provide a reasonably good characterization of the width of the central peak for all of the plots.

Figure A.18 shows our simulation result for the resolution as a function of angle, given a discriminator threshold of 2500 e^-. The points shown superimposed on the simulation result are the Gaussian standard deviations from the fits of Figure A.17. We have also computed residual distributions for this data set without using any charge sharing information. These "digital" resolution results are included in Figure A.18, superimposed on our simulated digital resolution.

Using this method, we have accumulated residual distributions as a function of incident beam angle for all five pixel sensors. All of the results are in reasonable agreement with our simulations. Figure A.19 shows the simulation and experimental results for the FPIX1 p-stop detector. These results are slightly worse than the results that we obtained by degrading the FPIX0 p-stop pulse height information to 2-bits equivalent (see Figure 4.6 in the body of this proposal). This is because the FPIX1-instrumented detector was operated with a discriminator threshold of ~3780 e^-, while the FPIX0-instrumented detector was operated

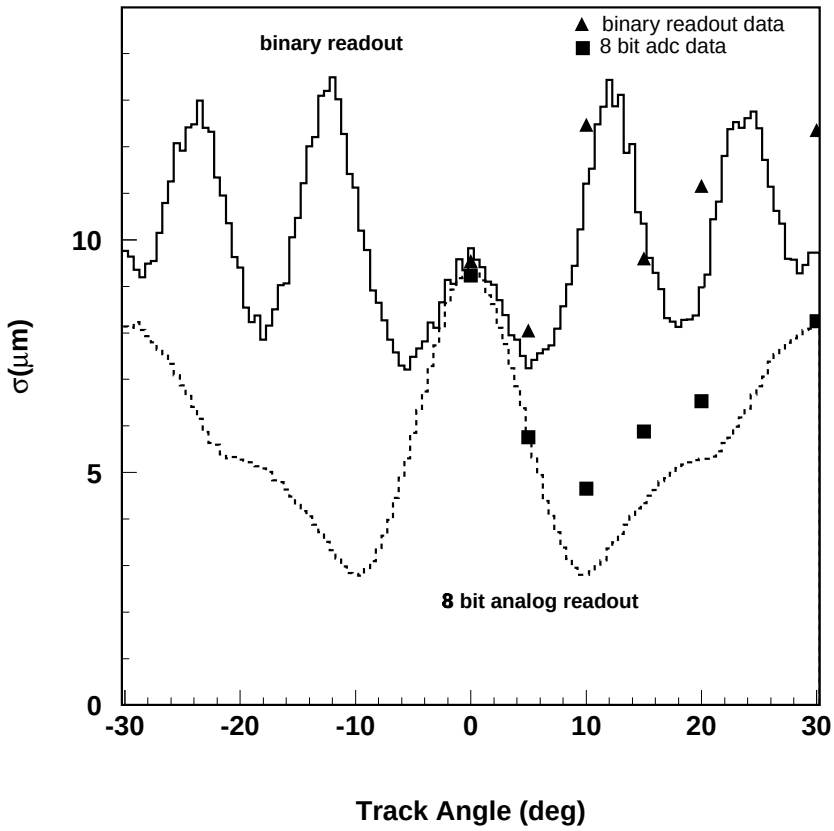

Figure A.18: Position resolution as a function of beam incidence angle for the FPIX0-instrumented CiS p-stop sensor. The curves are the simulated RMS for Q_{thres} = 2500 e^-. The oscillating curve is the simulated digital resolution; the lower curve assumes 8-bit charge digitization. The squares are the Gaussian σ's shown in Figure A.17, and the triangles are the σ's extracted from fits to residual distributions made without using charge sharing information.

with a discriminator threshold of ~2500 e^-. Figure A.19 shows that our simulation correctly describes the degradation of position resolution with increased discriminator threshold.

Figure A.20 shows how the position resolution is affected by changes in the sensor bias voltage and the discriminator threshold. As expected, these curves are highly correlated to the data presented in Figure A.15. At a given angle, more charge sharing translates directly into better position resolution.

The BTeV pixel detector will be exposed to a very non-uniform radiation dose. In our

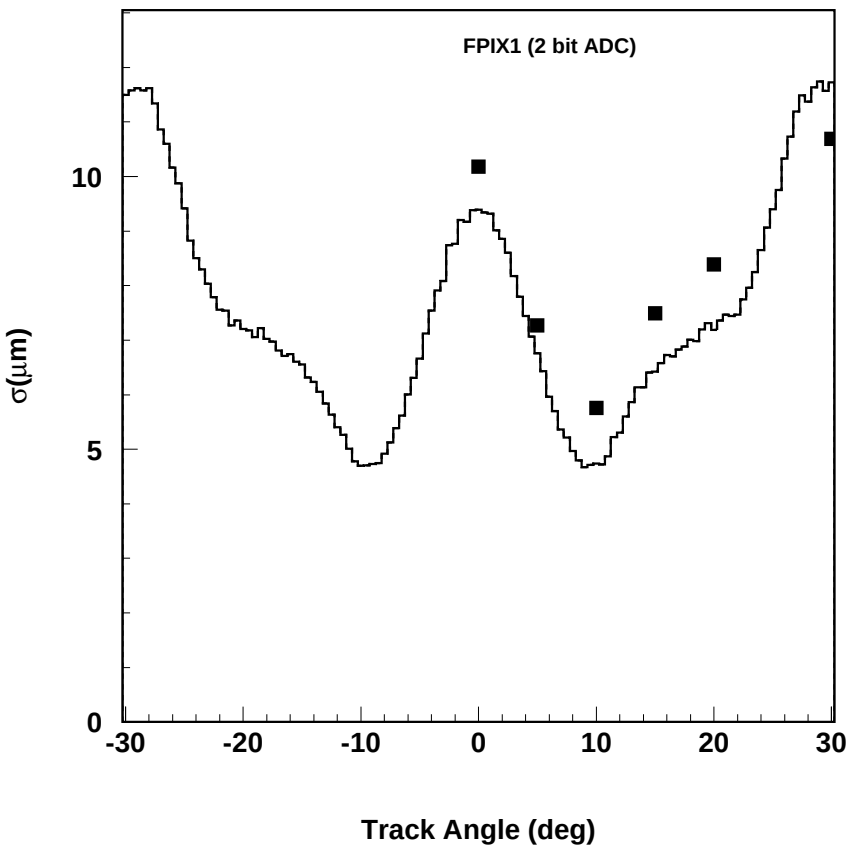

Figure A.19: Position resolution as a function of beam incidence angle for an FPIX1-instrumented Seiko p-stop sensor. The curve is the simulated RMS for Q_{thres}=3780 e^-, assuming 2-bit charge digitization. The squares are σ's from Gaussian fits to the residual distributions.

baseline design, a single sensor will extend from the outer edge of the detector, 5 cm from the beamline, to the inner edge of the detector, 6 mm from the beamline. As shown in Figure A.1, this will mean that the inner section of the sensor will radiation damage much faster than the outer section. Consequently, the depletion voltage of the inner section will change (first decreasing, and then increasing) much faster than the outer section. One bias voltage will be applied to the sensor, but the outer section will generally operate very over-depleted, while the inner section will likely be only slightly over-depleted. The insensitivity of the pixel position resolution to the degree of over-depletion shown in Figure A.20 is thus very encouraging. These data suggest that there will be little, if any, degradation in the position resolution as a function of radiation exposure until it is no longer possible to fully deplete the inner section of the sensor. At this point, the degradation in resolution due to loss of signal can be estimated using the results presented in Figure A.20.

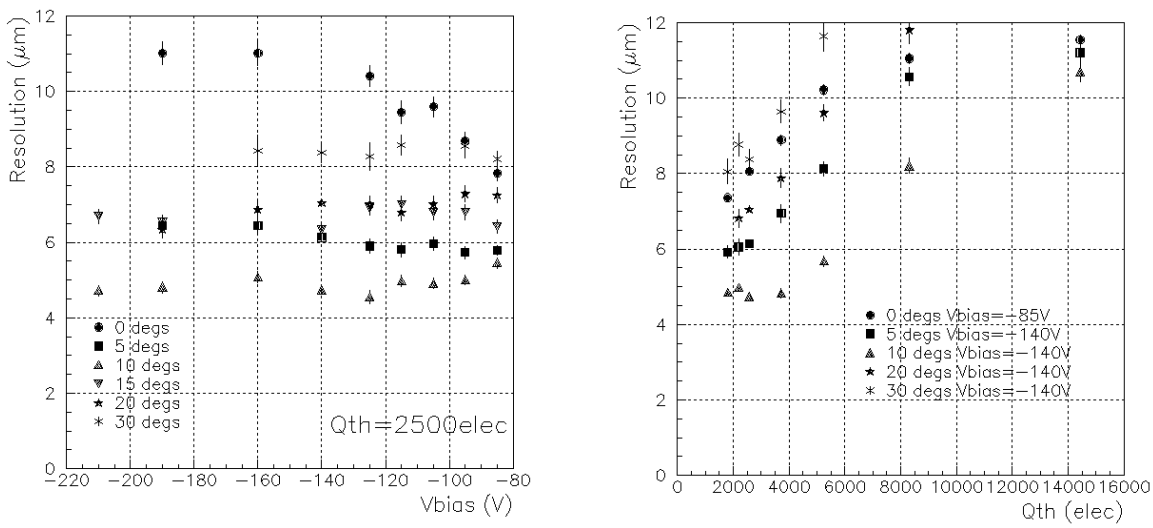

Figure A.20: Spatial resolution versus bias voltage for readout threshold and track angle fixed (left plot). Spatial resolution versus readout threshold for bias voltage and track angle fixed (right plot). The data are from FPIX0 p-stop.

A.1.2.8 More Accurate Fits to the Residual Distributions

The pixel residual distributions deviate from Gaussian in two important ways. First, for angles less than Arctan(50/300) = 9.5 degrees, some tracks pass through one pixel only. For these single pixel clusters, the residual distributions are almost square. In this case, the residual can be fit by the function:

$$F_1(x) = \int_{-\frac{p}{2}+W_D}^{\frac{p}{2}-W_D} dx \frac{F_1^0}{\sqrt{2\pi\sigma_{W_D}^2}} e^{-\frac{x^2}{2\sigma_{W_D}^2}} \tag{A.7}$$

This is a square convoluted with a Gaussian representing the fact that for tracks near an edge, diffusion spreads a fraction of the charge into the neighboring pixel. The total charge lost, which fluctuates from track to track, determines whether or not the neighbor receives enough charge to fire its discriminator.

The second factor that makes the pixel residual distributions non-Gaussian is the emmision of δ-rays. For relativistic particles, δ-rays are emitted at a large angle with respect to the particle direction. Very low energy δ-rays are emitted perpendicular to the track direction. Even 200 keV δ-rays are emitted at an angle of ~66 degrees[23]. These δ-rays travel a long distance in the pixel detector, and deposit energy as they do so. Low energy δ-rays which stop in one of the pixels crossed by the particle skew the charge sharing and degrade the resolution. Higher energy δ-rays cross one or more pixel boundaries and skew the position measurement even more. We have found that our experimental residual distributions for cluster sizes greater than one can be fit using a function which is the sum of a Gaussian term

and a term which is a square with edges that decrease like a power of 1/x:

$$F(x) = F_{Gauss}(x) + F_{power-law}(x) \tag{A.8}$$

where F_{Gauss} is a Gaussian, and $F_{power-law}$ is defined in the following way:

$$F_{power-law}(x) = \begin{cases} \frac{A_{pl}}{|r_{cut-off}|^{\gamma}} for |x| < r_{cut-off} \\ \frac{A_{pl}}{|x|^{\gamma}} for |x| > r_{cut-off} \end{cases} \tag{A.9}$$

A_{pl} is a normalization constant, $r_{cut-off}$ is the half width of the constant term, and γ is the exponent of the power law.

Figure A.21 shows the residual distributions for the FPIX0 p-spray detector taken with the beam (nominally) at normal incidence. The plot on the left shows the residual for one-pixel clusters, with a fit to equation A.7 superimposed. The plot on the right shows the residual for clusters of two or more pixels, with a fit to equation A.8 superimposed. The distributions are shown using a log scale to emphasize the fact that these functions provide good fits to the tails of the distributions.

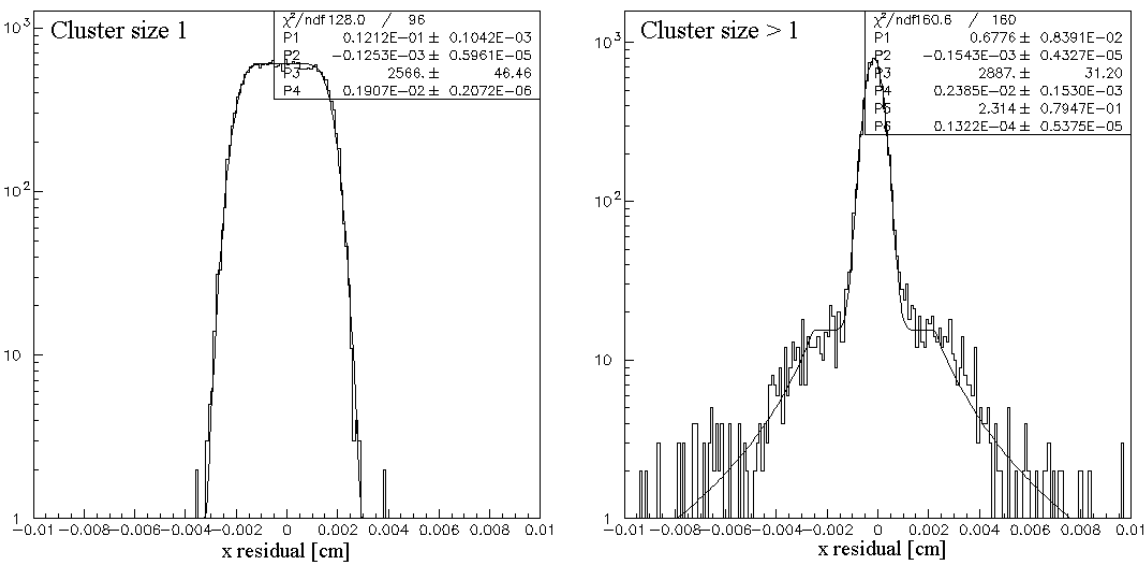

Figure A.21: Residual distributions of FPIX0 p-spray detector at zero degrees fitted with the functions described in this chapter. The plot on the left shows the distribution for cluster size 1 and the plot on the right for clusters having more than one hit.

All of our residual distributions are fit well using these functional forms. Moreover, we find that all of the residual distributions can be reasonably well described by equation A.8, using *one* set of parameters for $F_{power-law}(x)$. For all of these distributions, we find a satisfactory representation of the data with $\gamma = 2$, $r_{cut-off} = 15\mu$m, and A_{pl} set so that $F_{power-law}$ accounts for 20% of the total number of entries in the distribution.

For the simulations of physics processes discussed in the body of this proposal, the pixel resolution has been approximated by a Gaussian whose width is a piecewise linear function of the track angle. This function is shown in Figure 4.6 in the body of this proposal. For all Level 1 trigger simulations, we have added tails to this representation of the pixel resolution function using equation A.8, with the power-law parameters listed above. This slightly overestimates the tails for most angles of incidence, as can be seen in Figure A.22, and we are encouraged by the fact that the inclusion of these tails has only a very small affect on the Level 1 trigger.

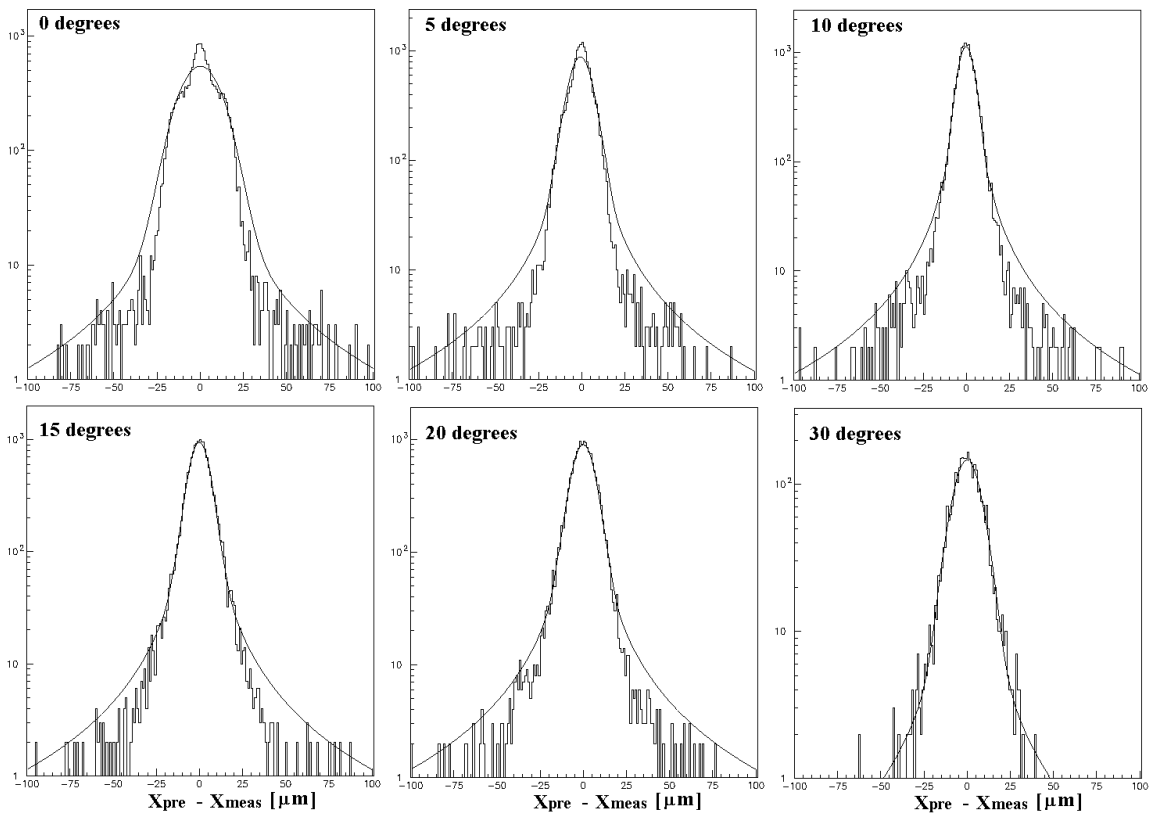

Figure A.22: Residual distributions for the FPIX0 p-stop detector. The data are the same as shown in Figure A.17, plotted here using a log scale to make the tails of the distributions easier to see. The curves superimposed on the plots are the resolution functions which were used in Monte Carlo studies of the BTeV trigger.

A.1.3 Electromagnetic Pickup Study

In order to study the effects of electromagnetic pickup on electronics located within the beam pipe, a bench top apparatus has been assembled which simulates the fields due to a circulating beam. This was accomplished using concentric cylinders. The center cylinder is pulsed using an Amplifier Research Model 3500A100 RF amplifier, and the outer cylinder is used as a return path for the current. The current along the center conductor approximates the circulating beam, while the outer conductor represents the beam pipe. The fields between these cylinders should approximate the expected fields in and around the BTeV pixel detector. The characteristic impedance for the apparatus is 50 ohms [24]. A 5 inch wide by half inch thick slot was cut into the outer pipe orthogonal to the apparatus axis to allow access to the field region between the pipes.

The input to the amplifier is driven by a pulse generator. The input pulse is roughly Gaussian with a width of 7ns. The pulse is repeated every 132 ns. The output pulse has a width of 8ns and a peak amplitude of 320 volts, corresponding to a peak current of 6.4 amps or 3×10^{11} electrons per pulse (which closely approximates the proton bunch density for the Tevatron). This pulse corresponds to an amplification factor of 20% of the maximum allowed by the RF amplifier.

A loop of wire was placed in the field region to measure the induced voltage with respect to apparatus ground as a function of the peak output power. This loop was terminated either with a 50 ohm resistor on each end or with a 10 kilo-ohm termination on both ends. The data is shown below.

50 Ω Termination		10 kΩ Termination	
RF Power (Watts)	Peak Voltage	RF Power (Watts)	Peak Voltage
80	2.7	60	7.1
180	3.3	160	9.0
340	4.1	320	11.5
580	5.0	560	14.7
1180	7.1	840	17.5

The first test utilized an existing data source (the Gazelle Developmental System or GDS). GDS sends and receives an ECL 40 bit random data pattern over a serial link and checks for errors. It can operate at 250 Mbps, 500 Mbps, and 1 Gbps. For our tests, the speed was 250 Mbps. The signal goes from the Gazelle System to the Finisar Card where the ECL signal is converted to an 850 nm fiber optic signal. The signal goes over 50/125 micron multimode fiber to the test card. On the test card, the signal is converted to differential ECL and goes over twisted pair wire through the field region. The signal is then sent back to the Gazelle System via optical fiber where it is checked for errors. The system is controlled by a Macintosh host computer which also displays the error rate.

With 20% RF amplification, no data errors were observed provided that the test card ground plane was tied to the outer shell of the apparatus. When the test card was isolated

from the outer conductor, data errors began to appear when the peak output power exceeded 1000 watts. At higher amplification, the error rate was essentially 100%. A metal plate was then added as a shield on the "upstream" side of the test card which reduced the error rate to zero.

A test card with traces of various length and width was manufactured to systematically study induced voltages and shielding techniques. In general, it was found that the induced voltage is weakly correlated with the trace width and length. Furthermore, grounded guard rings were not found to provide effective shielding from electromagnetic pickup. A solid metal foil connected to the apparatus ground (the outer cylinder) did dramatically reduce the pickup. Furthermore, simple low impedance resistive termination reduced the observed induced voltage by a factor of 10.

A simple test board without any shielding was built to study the operation of standard TTL chips in the field region. The test board consisted of a 555 timer and 7404 TTL inverter. The oscillation frequency was 30 kHz. Power and ground were brought into the field region using PCB traces, with the power and ground lines coupled using two 0.1 μF capacitors. Signals were brought out of the field region using micro coaxial cables.

During the first test, a ground strap was bolted between the board ground and apparatus ground. The circuit was found to perform flawlessly. Pickup was evident; however, the induced RF noise was measured to be only 400 mV (peak to peak). The grounding strap was then removed and precautions were taken to insure that the test board was electrically isolated from the apparatus ground. The 555 timer and 7404 inverter outputs were then measured with respect to the negative terminal of the DC power supply supplying power to the test circuit. As before, the circuit performed flawlessly with an RF noise of 400 mV evident. By measuring the board ground voltage with respect to the apparatus ground, it was found that the test circuit power and ground lines were floating with respect to the apparatus by more than 10 volts.

The TTL logic study will be extended to surface mount CMOS technology. A custom printed circuit board has been constructed using a 60 MHz CMOS oscillator connected to a CMOS inverter, connected to a PECL interface and Finisar optical transmitter. All components will be positioned within the field region. Future studies will also include prototype BTeV pixel boards along with an array of boards mounted within the apparatus to study the effects due to the unique BTeV pixel geometry. The initial studies are encouraging and indicate that RF pickup due to the circulating beams will not preclude the safe and reliable operation of pixel electronics inside the beam pipe.

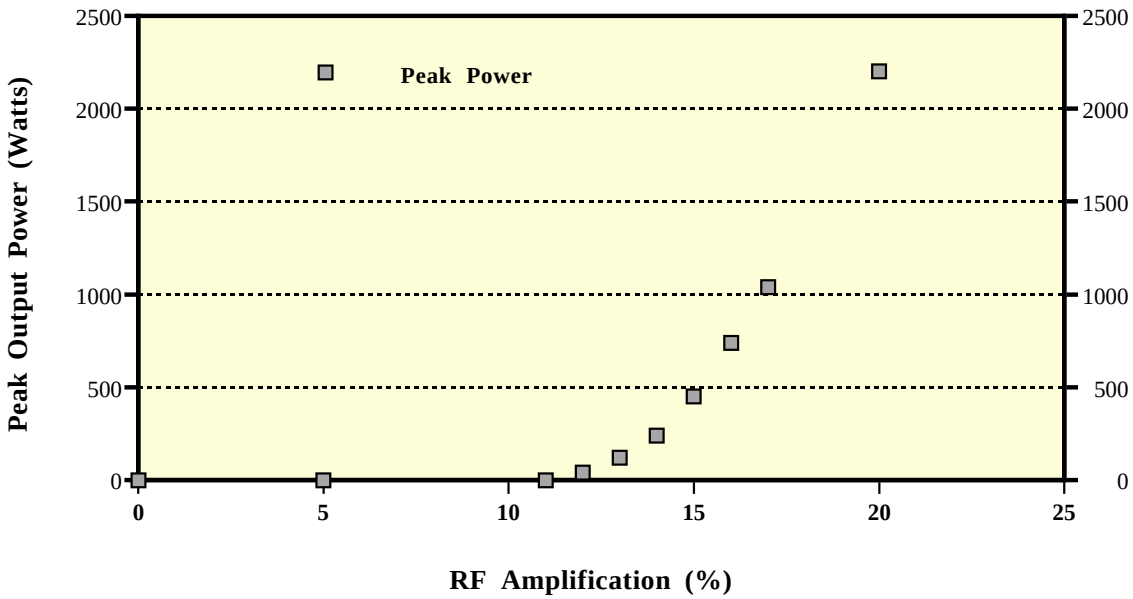

Figure A.23: Peak output power for the RF amplifier as a function of the RF amplification.

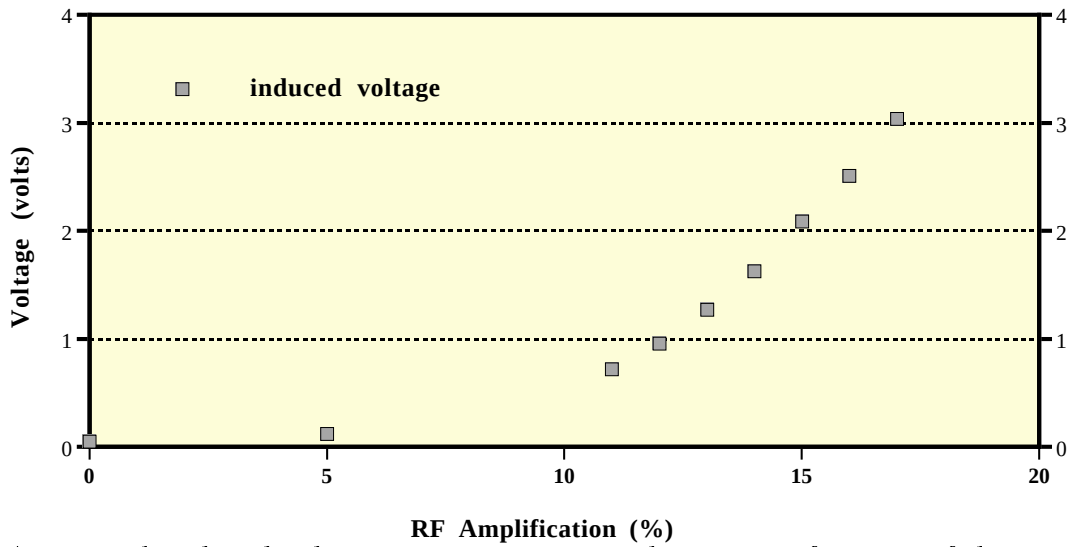

Figure A.24: Peak induced voltage on an unterminated trace as a function of the RF amplification.

A.1.4 FPIX2 Radiation Damage Tests

The first two generations of pixel readout chips designed at Fermilab (FPIX0 and FPIX1) were implemented in standard CMOS technologies (HP 0.8μm and HP 0.5μm, respectively). The R&D plan established in 1997 called for an eventual migration of the final FPIXn design to a military radiation hard technology, probably the Honeywell 0.5 μm CMOS SOI process.

In December, 1998, motivated by the results of RD49, which showed that commercial deep submicron CMOS devices could be made radiation hard, we modified our pixel chip R&D plan to focus on implementation in a commercial 0.25 μm CMOS process. Fermilab engineers joined RD49, and Fermilab initiated negotiations that have resulted in our gaining access, through CERN, to IBM's 0.25 μm CMOS technology. Since the Taiwan Semiconductor Manufacturing Corporation (TSMC) 0.25 μm CMOS, which is available through MOSIS, is similar to the IBM process, we decided to try to develop it as a second source. Starting with the radiation tolerant design rules developed at CERN for use with the IBM process, Fermilab engineers developed a set of design-rule files for their CADANCE IC design program which satisfy both IBM and TSMC design constraints. FPIX2 is being designed for implementation in 0.25 μm CMOS, either using the IBM process, or the TSMC process, or both.

Two prototype circuits have already been designed and fabricated using TSMC 0.25 μm CMOS. The first (preFPIX2) included sample transistors, and a small number of redesigned FPIX amplifiers and comparators. The second (preFPIX2T) includes two columns of 160 rows of complete FPIX2 pixel readout cells. Bench tests of these circuits verify that the analog sections of the new FPIX2 perform at least as well as previous FPIX circuits.

Very recently (April 18 - April 24, 2000), preFPIX2 and preFPIX2T chips were irradiated using a Co^{60} source at Argonne. The preFPIX2T chips received a dose of approximately 33 MRad. This is roughly equivalent to the 10^{15} particles/cm^2 exposure anticipated at the inner edge of the BTeV pixel detector after 10 years of running at a luminosity of 2×10^{32} cm^{-2}sec^{-1}. A preliminary analysis of data collected before, during, and after this irradiation is very encouraging. Figure A.25 shows the measured amplifier noise and discriminator threshold for the 320 cells in one preFPIX2T, both before and after irradiation. The circuit was biased using the same voltage and current levels after irradiation as before. After irradiation, the amplifier noise increased by less than 5%. The average discriminator threshold, expressed in equivalent e$^-$, for the applied threshold voltage, went down from $\sim$1100 e$^-$ to $\sim$1000 e$^-$, and the discriminator threshold RMS did not increase at all. More analysis is required to determine whether or not the apparent *decrease* in threshold dispersion is statistically significant.

Previous RD49 radiation damage tests have all been performed on parts made using IBM 0.25 μm CMOS. Our results verify that circuits fabricated using TSMC 0.25 μm CMOS are similarly radiation tolerant.

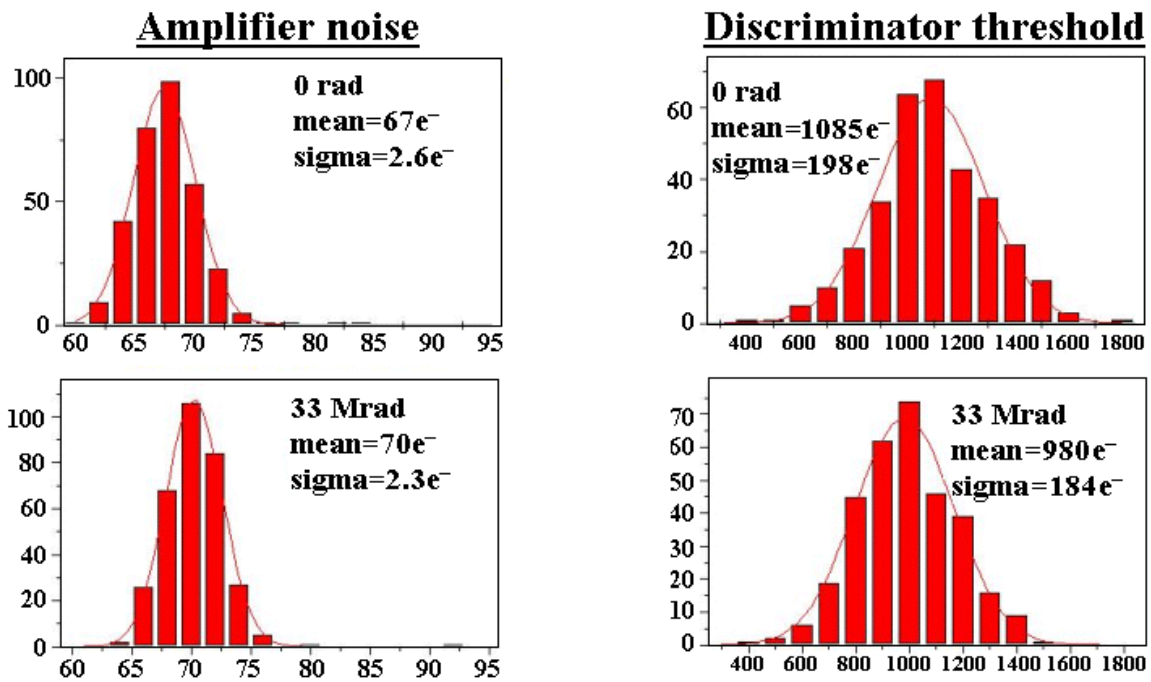

Figure A.25: PreFPIX2T radiation tolerance. The plots on the left show the measured amplifier noise for the 320 cells of a preFPIX2T chip. The average noise increased from 67 e^- to 70 e^- after 33 MRad. The plots on the right show the distribution of discriminator thresholds for the same 320 cells, before and after irradiation. The plots show that with the same external threshold voltage applied, the effective threshold decreased from ~1100 e^- to ~1000 e^- after 33 MRad. The threshold dispersion did not increase after irradiation.

Bibliography

[1] M. Moll, *Summary of the 3rd Rose Status Report*, 5th Rose Workshop, March 2000.

[2] The ATLAS Pixel Detector Technical Design Report, CERN/LHCC-98-13.

[3] *The CMS Tracker Project Technical Design Report*, CERN/LHCC-98-6.

[4] E. Fretwurst *et al.* , *Nucl. Instr. Meth.* **A326** (1993) 357; V. Eremin, Z. Li *Nucl. Instr. Meth.* **A362**, (1995) 338; Z. Li *Nucl. Instr. Meth.* **A360** (1995) 445, Z. Li *et al.* , *Nucl. Instr. Meth.* **277** (1996) 265; Z. Li *Nucl. Instr. Meth.* **A368** (1996) 353.

[5] The ROSE Collaboration *RD48 Status Report*, CERN/LHCC 97-39 (1997).

[6] The Rose Collaboration *CERN Report LHCC-2000-09*, Dec. 1999.

[7] M. Artuso, Presented at 29th International Conference on High-Energy Physics (ICHEP 98), Vancouver, Canada, 23-29 Jul 1998, Syracuse Un. Preprint HEPSY-98-2, (1998).

[8] F. Hügging *et al.* , *Nucl. Instr. Meth.* **A439** (2000) 529.

[9] F. Ragusa *contributed talk to Vertex '99, Preprint submitted to* Nucl. Instr. Meth. (1999).

[10] M. Artuso and J. Wang, BTeV Internal Report BTeV-Int-97-18, February 1998

[11] E. Belau *et al*, Nucl. Instr. and Meth. **124**, (1983) 253.

[12] R. Turchetta, Nucl. Instr. and Meth. **A 335**, (1993) 44.

[13] H. Bichsel *Rev. of Mod. Phys.*, (1988) 663.

[14] L.H.H. Scharfetter (RD19), *Active Pixel Detectors for Large Hadron Colliders*, CERN Thesis, 1997, and *CERN 99-09* (1999)

[15] P. Kasper, BTeV Internal Report BTeV-int-98/3, March 1998.

[16] G. Cancelo *et al.*, BTeV Internal Report BTeV-int-98/16, September 1998.

[17] C.J.Li and Z. Li, *Nucl. Instr. Meth.* **A364** (1995) 108.

[18] T. Rohe, et al., "Sensor Design for the ATLAS Pixel Detector", Nucl. Instr. and Meth. A409 (1998) 224.

[19] T. Zimmerman, et al., "Design of an Advanced Readout Chip for Silicon Strip Detectors", IEEE Trans. Nucl. Sci. Vol.40, No.4 (1993) 736.

[20] S. Hancock, et al., "Energy Loss Distributions for Single Particles and Several Particles in a Thin Silicon Absorber", Nucl. Instr. and Meth. B1:16 (1984)

[21] The Atlas silicon pixel sensors, ATLAS-INDENT-NO-XXX September 10, 1999

[22] R. Kutschke, "Coordinate Systems in the 1999 Test Beam Run", BTeV Internal Report, BTeV-int-1999/10+ (1999).

[23] M. Pindo, "Simulating Charge Collection in Silicon Pixel", Nucl. Instr. and Meth. A 395 (1997) 360.

[24] Specifications and a schematic of the beam simulator apparatus can be found at http://www-ap.fnal.gov/~gpj/BTeV/pixel_shield.html.

A.2 RICH Design and R&D

A.2.1 Hybrid Photodiode R&D

The PP0380V HPD tube from DEP [1] (see Fig 5.5 in Part II) which we plan to use to detect Cherenkov photons has been described in Part II of this proposal.

DEP, the manufacturer of the HPD, is an electro-optics company with over 20 years of experience in the field of image intensifiers. Its manufacturing capacity is about 6000 such devices per year; no image intensifier tube has ever been rejected after delivery, according to DEP. They have been producing hybrid tubes for several years. Last year, they produced 30 HPDs of the 61-channel variety.

HPDs are also the photon detector of choice for the CMS HCAL (about 500 HPDs of 19 and 73 channels), and the LHC-b RICH (about 500 HPDs of 2048 channels).

There are two issues in the tube construction which require development work: material to block short wavelengths and segmentation of the silicon diode. They are actually coupled to each other. We would like to operate with wavelengths above 280 nm, which makes the chromatic error somewhat smaller than the emission point error. This scheme also requires that the silicon diode segmentation is increased from the 61 pixels presently used by DEP to 163 pixels in order to bring the segmentation error down to a value comparable with the emission point and chromatic errors. Such an increase of diode segmentation can be achieved with the present manufacturing process. The development would be done by DEP and their subcontractors. The cost of this development is included in our budget.

The presently manufactured tube has a quartz window which cuts off at 160 nm. To increase the cut-off value to 280 nm, we plan to investigate alternative window materials, various coatings of the quartz window or a separate window between the gas volume and the HPDs. The latter solution is attractive from the point of view of sealing the RICH vessel, but would induce $\sim 8\%$ loss in photon yield due to the reflective losses.

The alternative approach would be to make use of the large wavelength sensitivity of the HPDs with quartz windows. This makes the chromatic error much larger but leaves per track Cherenkov angle resolution almost unchanged (about $\sim 10\%$ deterioration) because of the larger number of detected Cherenkov photons. In this approach, there is no need to develop a new silicon diode, since the 61 pixel version already produces a satisfactory segmentation error. Making use of short-wavelength photons imposes much stricter requirements on gas purity, mirror quality, etc., which is why we do not favor this solution. Such a possibility illustrates, however, that the performance of the RICH detector does not crucially depend on the success of the developments mentioned above.

There are, of course, a large number of tests which need to be performed on the HPDs. These are tests of linearity, gain, and uniformity of response. In addition, it is critical to study issues of tube aging, which are known to be caused by either Si diode instability, or photocathode degradation with time. These are not expected to be a problem in our design, however, due to the low radiation dose at the photon detector plane and the low light levels.

A.2.2 HPD High Voltage System

The Hybrid Photon Detector requires a very high applied voltage in order to provide the ejected photoelectron with the kinetic energy necessary to produce a sufficiently large signal, as there is no intrinsic charge amplification. The HPD design [1] requires three very high voltages: 20 kV for the photocathode, 19.9 kV for electrostatic focus, and 4.2 kV for final demagnification. There is essentially no current draw ($\sim$10 nA) for these electrodes. In addition, the HPD requires a 60 V low voltage for reverse-biasing the Si diode.

Our choice for a high voltage system is the commercially available CAEN SY 1527 system. CAEN either has developed or is currently developing modules for this system which suit our needs, with the exception of the 20 kV requirement. However, they are very interested in pursuing development of such a module, which would also be useful to LHC-b for their HPDs. For a previous system (SY 127) they already produce a 20 kV module, so the technical issues of very high voltage are well-understood by them.

Since there is effectively no current draw by the HPD, one can simply fan out each HV channel to a number of different tubes. Therefore our design for the distribution of the high voltage uses cable assemblies to bus the voltage from the SY 1527 or SY 127 modules to each HPD of a gang of HPDs. Currently we envision ganging 15 HPDs per single HV channel separately for each of the four voltages required.

The high voltage issues to be addressed by future R&D are:

1. Development of the 20 kV CAEN module. This development will be done by CAEN. With some inconvenience we could also use the existing SY 127 module.

2. Development of robust HV cable assemblies. The high voltage assemblies must fan-out a given voltage to a number of HPDs. They consist of cables, connector, and custom-made fan-outs and feed-throughs. Some of these components are commercially available, such as the cable and connectors. Other components such as the fan-outs, feed-throughs, and the assembly design itself must be developed and tested, and must be mechanically and electrically robust. We have to determine if the HV cable must be shielded, what material to use for the fan-outs, and how to design the feed-throughs.

3. Testing and Integration of the HV cable assemblies. In conjunction with the mechanical design, described elsewhere, the cable assemblies must be properly integrated to avoid arcing and corona discharges. Each assembly also needs to be tested beforehand at voltage in a test station.

A.2.3 Photon Detector Mechanical Design

The mechanical support structure for the photon detectors must support the tubes themselves, plus the analog electronics, digital electronics, high voltage cable assemblies, and cooling pipes. Additionally, the front face of the HPDs will make a gas seal to the gas radiator volume.

This structure must be designed in an integrated manner, taking into consideration all of the requirements of each of the parts it supports, i.e., mechanical, electronic, and thermal elements.

The current design calls for triads of HPDs to be bundled together as a unit, with readout electronics. This triad will be tested together and mounted as a single module.

There are several issues to be resolved in future R&D of the mechanical design.

1. The faces of the HPDs are hexagonally packed together on the detector plane, and should be maintained at the closest possible packing fraction to avoid loss of Cherenkov photons. The optimal way of accomplishing this needs to be determined.

2. The exterior of the HPD is at voltage, so it needs to be coated with Kapton or an equivalent material. The HPD triad bundling and support should not be metallic. There can be no possible corona points in the design.

3. The front of the HPD must make a gas seal with the gas radiator volume. The amount of pressure required and the mechanical support to deliver the compression needs to be studied. However, to ease the necessity of a high-quality seal, the photon detectors will be enclosed in a separate gas volume containing clean gas.

4. There must be sufficient support for the electronics and cooling at the rear of the HPDs. Transverse space for this and the high voltage cabling is at a premium, and a detailed design with realistic materials and standoff is needed.

Again, these issues are intimately connected to the overall mechanical structure for the photon detectors, which is non-trivial and needs to be engineered as an integrated whole.

A.2.4 HPD Readout Electronics

The signal produced by the hybrid photodiode (HPD) is a narrow charge pulse of ~ 5000 electrons. Our goal is to achieve a signal to noise ratio of about 7, corresponding to an equivalent noise charge (ENC) of about 700 e^-. The charge pulse duration depends upon the bias voltage of the silicon pad detector and its input capacitance and is typically around 10 ns. Thus, the readout electronics determines the time development of the analog signal. Our goal is to process the information coming from this detector element within the bunch crossing it originates from. This means that the information must be transferred to the data combiner chip discussed elsewhere [2] within 132 ns. The maximum number of readout channels to be instrumented is 339,040 corresponding to 2,080 readout chips.

Fortunately, there are some front end devices already developed and produced with their characteristics tuned to a whole variety of different applications that we can adapt to our system. These ASICs belong to the so called VA family [3], developed and produced by IDE AS, Norway [4]. They have been used in a variety of systems including particle physics detectors, both accelerator based [5] and in space [6], as well as for medical applications [7]. We have worked with this company on a previous project, the CLEO III RICH, to develop a

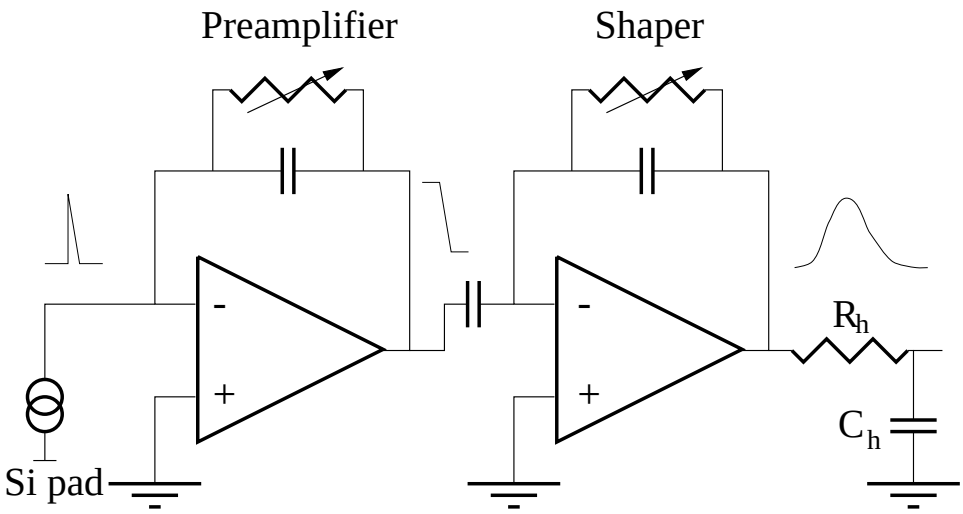

Figure A.26: Block diagram of the analog cell in VA circuits.

custom made ASIC, the VA_RICH and associated hybrids, that will be described below [8]. While this particular chip is not appropriate for BTeV, our experience has been extremely positive, both in terms of reliability of the products and in terms of meeting the production schedule and this gives us confidence that this effort will proceed equally smoothly. Thus we are planning to employ a custom made adaptation of an ASIC of the VA family, that we will refer to as VA_BTeV, as the front end device for HPD readout.

This conservative approach of decoupling the HPD and the readout electronics production is possible because the segmentation optimal for our needs allows us to bring the pad signals out of the HPD tube as pins that can be mated with a multi-chip module containing the readout electronics. On the other hand, LHC-b is pursuing an integrated sensor-chip system inside the tube as their preferred solution because they require a much finer segmentation than BTeV. This couples the tube manufacturing with the silicon pad detector and the readout electronics production which makes all stages of the project more difficult.

The most common solution for low noise analog front end chips for solid state and gas pad detectors is based on a RC-CR preamplifier and shaper circuit, which is at the core of the analog cell in the VA circuits. Fig. A.26 shows a block diagram of this circuit and the profile of the voltage signal at the output of the individual processing elements. This analog cell consists of a charge sensitive preamplifier with a large voltage-controlled resistor in the feedback loop to insure DC stability, followed by an AC coupled shaper that limits the bandwidth of the system. The bandwidth is related to the peaking time of the system: a short peaking time corresponds to larger bandwidth, making it more challenging to keep the ENC low as the dominant source of intrinsic electronic noise has a uniform power density spectrum. We are seeking peaking times below 100 ns.

Our goal is an equivalent noise charge (ENC) of 700 electrons or better. This would be a challenging task for new, undeveloped readout electronics, especially at the short peaking times that we envisage. The ASIC called VA_32/75 [4], already fully engineered and available from IDE AS as a 32 channel chip, has a nominal peaking time of 75 ns and a noise

performance given by:

$$\text{ENC} = 400e^- + 25e^-/\text{pf} \times C_{in} \tag{A.10}$$

This would correspond to an ENC of 500 e^- at our expected input capacitance of 4 pF. It is very likely that a tuning of the chip parameters for our specific application will achieve better noise performance for VA_BTeV, even though an ENC of 500 e^- is already suitable for our needs.

We have opted for a binary readout as we can achieve adequate spatial resolution with binary charge weighting and the readout system is much simpler this way. Thus, the analog section is followed by a discriminator to perform zero suppression. This component of the VA_BTeV chip is based on the TA32C fast triggering ASIC [4], developed by IDE AS for medical imaging applications. Each channel will feature a discriminator with its threshold individually adjusted with an internal DAC. The zero suppressed output will be sent to the BTeV data combiner multichip module. The low occupancy of the system allows us to fan in 3 VA_BTeV circuits to a single data combiner chip.

We are planning to purchase the VA_BTeV ASICs mounted in a multichip module. IDE AS has experience on a variety of packaging solutions. In particular, some packaging previously implemented by IDE AS match the HPD pinout structure quite closely. Possibly, 3 such modules could be integrated in a single printed circuit board to reduce the number of interconnections between individual ASICs and the data combiner chip hybrid.

A.2.4.1 The CLEO III RICH front end electronics

A brief summary of the process that we followed in acquiring the CLEO III RICH electronics and the performance that we achieved may be interesting to put this new effort in perspective. The CLEO III RICH includes 230,400 channels that need to be processed with low noise electronics to achieve good efficiency also for the low level photon signals that are quite copious in this device as the probability distribution of the charge produced in the avalanche initiated for a single photon is exponential.

The chip that was developed by IDE AS, VA_RICH, is an adaptation of the VA design concept to optimize simultaneously the noise performance and the dynamic range. This chip features 64 readout channels. IDE AS assembled them in G10 multi-layer hybrid circuits hosting two ASICs.

The VA_RICH chip is described by a block diagram similar to the one shown in Fig. A.26. The resistor R_h in this case is a switch and the capacitor C_h is the analog memory in this sample and hold circuit. Upon receiving a logical signal that signals that the charge is ready to be read out, the switch opens and the charge signal is stored in C_h. In our case we could afford to use a serial readout for 128 channels. Thus, two chips are daisy-chained and the signals stored in the capacitors C_h which are sent to the remote processing electronics as differential current signals. The clock driving the shift register that connects individual channels to the output has a frequency of 7 MHz.

The noise of this chip, measured in a laboratory test setup is [8]:

$$ENC = 117e^- + 8.1e^-/\text{pf} \times C_{in} \tag{A.11}$$

This performance was achieved with a peaking time of 2 μs. The input capacitance is relatively large because the signal from the cathode pad needed to be fanned in to a high density connector and then routed from the connector to the input pad on the chip. An average input capacitance of the order of about 15 pF is our estimate, with some spread due to different trace lengths. Thus we would predict an average noise figure of about 240 e^-. Note that the task of maintaining this low noise performance is very challenging because the power supply and all the control bias voltages and currents are provided by boards residing on a VME crate which feature mixed analog and digital circuitry and are transmitted by cables about 20 ft long [9]. This system has an additional component of coherent noise, due to ground fluctuations, that is subtracted on line, and some incoherent noise due to some small coupling between analog and digital ground in the data boards. However, the mean noise measured in the whole detector is about 400 electrons, which is good for such a large system with the constraints discussed above. The long cable and the vicinity of complex VME digital activity in the vicinity of the analog section will be missing in the BTeV design.

The VA_RICH production followed the initially projected schedule quite well. We produced a total of 2,200 hybrids, 1,800 of which are installed in the RICH detector. A smaller number (16) are employed to read out the main CLEO drift chamber cathodes. The hybrids were produced and tested at IDE AS, Oslo. They were subsequently tested at Syracuse University upon arrival and underwent a 1 week burn-in running at elevated temperature to eliminate the hybrids susceptible to early failures during detector operation. Almost no hybrids were discarded after this test. In summary, the production went quite smoothly and the performance achieved in the complete system is quite consistent with the expectations from our initial prototype characterization.

A.2.5 Silica Aerogel Radiator

The physics rationale for the use of a silica aerogel radiator in addition to a C_4F_{10} gas radiator has been presented in detail in Part II. Kaon/proton identification is extended below 9 GeV/c to $\sim$3 GeV/c, and also the fake-rate for a given efficiency is reduced compared to a gas radiator alone. The dual radiator approach has been proposed for one of the LHC-b RICH detectors [10] and has been adopted by HERMES for its RICH [11]. We now discuss some of the technical issues associated with the use of silica aerogel.

The most advantageous feature of silica aerogel is that its refractive index is in the range 1.01 to 1.10, placing it between that of the heaviest gas (C_4F_{10}, n=1.00138) and the lightest liquid (C_5F_{12}, n=1.26). The implication for a RICH detector is that this material allows hadron identification in the difficult momentum region of a few GeV/c. Aerogel is very light and does not add substantially to the material budget in front of the EM calorimeter. It is difficult to handle since it is extreme fragile, and can cleave with very little applied stress.

A.2.5.1 Fabrication Issues

Traditionally, the utility of silica aerogel has been limited due to the pore size acting as a strong Rayleigh scattering center. Recently a new fabrication technique has been developed

by KEK for BELLE which results in aerogel of better transparency [12, 13]. The strength of the Rayleigh scattering component was reduced by approximately a factor of two over previous values. This technique has been transferred to manufacturer Matsushita Electric Works, Ltd (Japan), who subsequently manufactured the aerogel for HERMES [11].

The Syracuse University group has had extensive discussions with Matsushita about their aerogel production and capabilities, which were very favorable. HERMES required ~100 liters of aerogel, which Matsushita successfully provided. In fact, their production output totaled ~1500 liters of aerogel last year. From them we have a price quotation for their standard material, and furthermore we have had discussions on the possibility of modifying their technique to obtain even clearer aerogel. They are currently evaluating this possibility.

In addition, there is another source of very good quality aerogel from the Boreskov Institute of Catalysis (Novosibirsk, Russia) [14, 15]. The capacity of this group is currently quite small, and thus far they have only produced aerogel with a different refractive index than we require, so we choose to stay with Matsushita but retain them as a backup source.

A.2.5.2 Transmittance Measurements

We have obtained six samples of standard SP-30 aerogel manufactured by Matsushita, and have performed a number of measurements on them.

Transmittance Measurement Technique

Transmittance measurements were made at Syracuse University with a Visible Light Spectrophotometer, a system consisting of an intense light source, chopper, monochromator, XY position control stage, PMT, ADC, and LabVIEW readout. This system, originally designed for measurements in the VUV (Vacuum Ultra Violet) of crystals for the CLEO-III RICH, has been modified to work in the visible spectrum.

The external transmittance is measured by taking the ratio of measured PMT photo-voltages for the "sample-in" over "sample-out" conditions, i.e.,

$$T_{\text{ext}} = \frac{\Delta V_{\text{in}}}{\Delta V_{\text{out}}}, \tag{A.12}$$

where ΔV indicates photo-voltage amplitude, with automatic baseline subtraction provided by the chopper, and the denominator is sampled periodically during the measurement procedure.

Currently, we are able to measure transmittance as a function of wavelength in the range 280–530 nm, with an accuracy of about 0.01. (We expect the HPD quantum efficiency to have an effective bandwidth 280–650 nm.) Systematic studies and wavelength calibration have been performed.

Transmittance Spectrum

The external transmittance was measured as a function of wavelength for all six Matsushita samples. At each wavelength, nine points over the face of the sample were measured and averaged. The result for all samples is shown in Figure A.27. The rms spread among the samples was under a few percent.

Also shown is a fit of the data as a function of wavelength, given by the standard parameterization of the external transmittance,

$$T_{\text{ext}} = A_H e^{-C_H d/\lambda^4}, \tag{A.13}$$

where the "Hunt parameters" are A_H, the asymptotic value of the transmittance, typically 0.95, that of a good glass, and C_H, the "clarity coefficient", the strength of the Rayleigh scattering component, typically 100 in units of $10^{-4}\,\mu\text{m}^4\text{cm}^{-1}$ for good aerogel. The wavelength dependence in this formula indicates the dominance in the attenuation process of the Rayleigh scattering component. Our fit yields the values

$$A_H = 0.977, \quad C_H = 67.9 \times 10^{-4}\,\mu\text{m}^4\text{cm}^{-1}, \tag{A.14}$$

which corresponds to a typical Rayleigh scattering length at 400 nm of $L_{\text{scatt}}^{(400)} = 3.77$ cm. This nearly matches our design thickness of 4 cm.

XY Uniformity Scan

A two-dimensional scan of some of the tiles was made, in which the external transmittance was measured at an array of positions over the surface of the piece. The result of the scan indicates that the external transmittance varies over the surface by about 5%. This variation is dominated by an area which has a filmy residue on the surface, clearly apparent on each of the samples, and probably the consequence of handling during the manufacturing process. There is no indication of any systematic drop in transparency near the edges.

Comparison of Different Aerogels

The external transmittance was also measured for a number of other samples, obtained courtesy of KEK. These were samples from the BELLE Endcap Aerogel Cherenkov Counter, labeled EACC herein, and a sample from the Novosibirsk group, which has $n = 1.05$.

From measurements of these samples, the Hunt parameters were extracted, and compared to other results available in the literature (either the published parameters or parameters extracted from published plots). Figure A.28 and Table A.2.5.2 summarize the results of our measurements and comparison.

The Matsushita samples we have obtained are in fact quite good, compared to the average Hermes and KEK EACC aerogels. They are not as good as the Novosibirsk aerogel, or the best samples that KEK has produced. We believe that further improvement can be obtained by the modification to the manufacturing technique mentioned above.

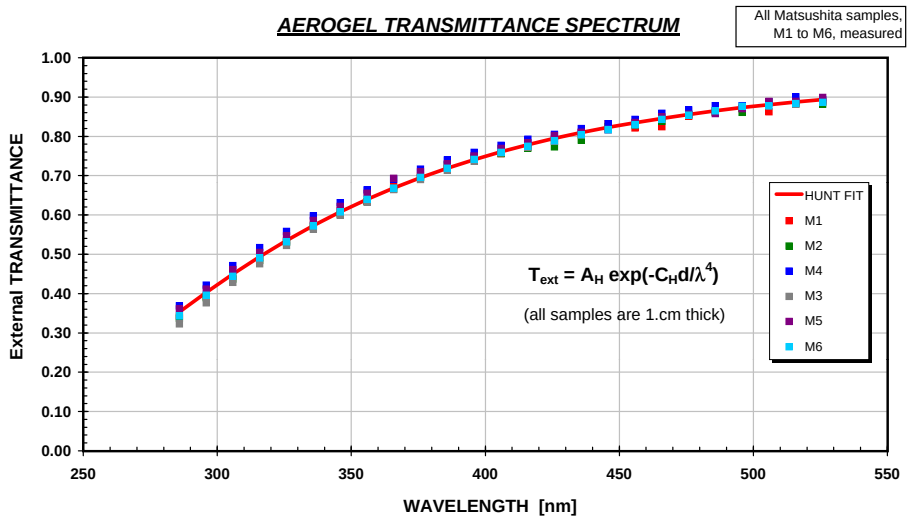

Figure A.27: Aerogel Transmittance as a function of wavelength, for six Matsushita samples. Points represent the data, the line represents a fit made to the standard Hunt formula.

Transmittance Variation with Thickness

As a test of the variation of the transmittance with thickness, we have measured the transmittance of a stack of Matsushita aerogel tiles, from 1 to 5 tiles (approximately 1 to 5 cm). This is not an accurate measurement of the bulk absorption of aerogel, rather it provides a comparison of a stack of tiles, with gaps, to a single thick tile, with the bulk absorption calculated from the Hunt formula extrapolated to the given thickness.

Figure A.29 shows the result of this comparison for our nominal design thickness of 4

Table A.2.5.2. Comparison of Different Aerogels.

Aerogel Source	n	A_H	C_H $[10^{-4}\mu m^4 cm^{-1}]$	$L_{scatt}^{(400)}$ [cm]	Comments
Matsushita	1.03	0.977 ± 0.002	67.9 ± 0.4	3.77	SU measurements
Novosibirsk	1.049	0.983 ± 0.011	54.0 ± 1.2	4.74	SU measurements
Novosibirsk	1.050	0.926 ± 0.012	47.8 ± 2.4	5.36	fit from data, [14]
HERMES	1.03	0.964	94	2.72	published fit, [11]
KEK EACC	1.030	0.980 ± 0.004	78.6 ± 0.7	3.26	SU measurements
KEK best	1.028	0.949 ± 0.006	49.9 ± 1.1	5.13	fit from data, [12]
Airglas Ltd	1.03	0.96	180	1.42	old one-step method [16]

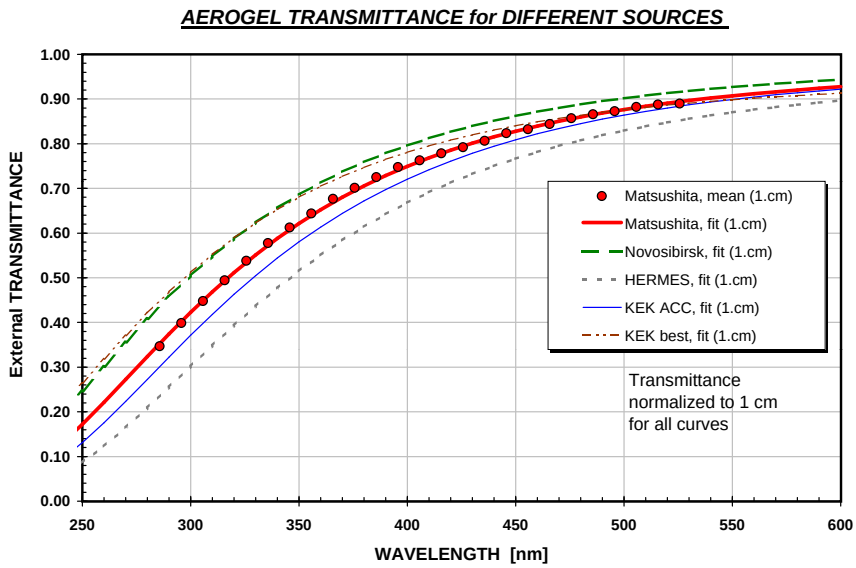

Figure A.28: Aerogel Transmittance as a function of wavelength, for samples from different sources. The data points indicate the mean transmittance of the Matsushita samples, whereas the lines are Hunt parameter fits as described in the text, all normalized to 1 cm thickness.

cm. As expected, the result is that the stack has a transmittance lower than the bulk by about 5% at 400 nm and about 10% at 500 nm (where the HPD quantum efficiency starts to drop). This scaling approximation may overestimate the transmittance due to multiple scattering in the thicker bulk. In any case, we conclude that we can reasonably stack the tiles mechanically in the detector and still obtain good transparency.

A.2.5.3 Future Aerogel Radiator R&D

The major issues for the aerogel radiator are:

1. Is the aerogel sufficiently transparent? Is it uniform over the face of the tile?

   Our measurements so far indicate that the Matsushita aerogel has good transparency, which should provide slightly larger photon yield than the 8 photons per track detected in the HERMES experiment [11]. Further improvements in transparency would increase the photon yield per track. As noted above, we must continue to pursue this issue with the manufacturer.

   We have provisional evidence that transmittance is uniform to about 5% over the face of the tile, however there are mechanical variations at the edges of the tile which provide non-uniform boundaries between tiles. This too needs to be improved by the manufacturer.

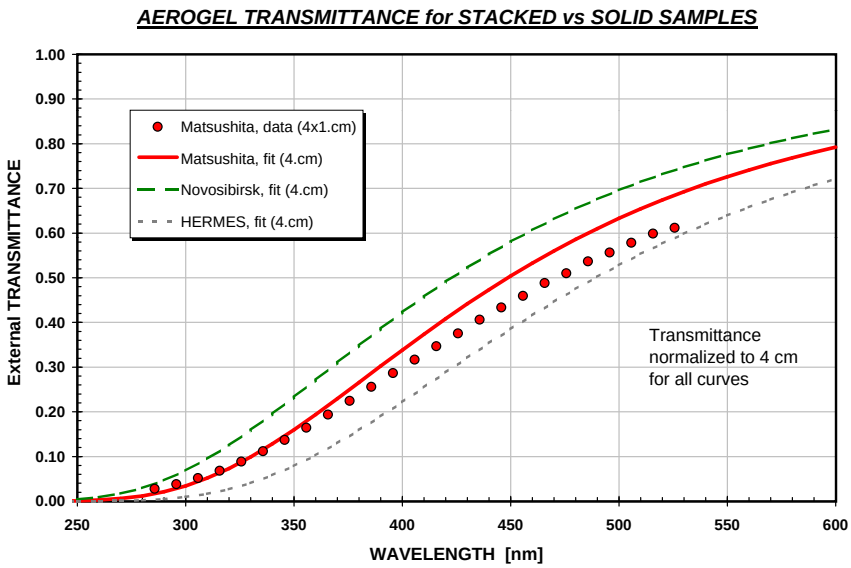

Figure A.29: Aerogel Transmittance as a function of wavelength, for a stack of 4 Matsushita tiles (data points), and for the Matsushita samples extrapolated to 4 cm bulk thickness (thick line). Other samples are shown for comparison.

2. Choice of a suitable window for aerogel-C_4F_{10} interface.

   The Rayleigh scattering cross-section increases for shorter wavelengths. Many scattered photons are eventually absorbed. Those which exit to the gas volume become background hits for Cherenkov ring reconstruction. The majority of the scattered photons can be eliminated by a suitable choice of window material to be inserted between aerogel and the gas radiator which would block short wavelengths. The type of material must be radiation hard. Material type and thickness need to be studied. This can be done with the existing transmission measurement setup.

3. Is the aerogel refractive index sufficiently uniform over a tile?

   We have not yet made this measurement. There are reported in the literature refractive-index variations of 0.003 over the face of a tile, peaking at the edges [14]. We need to construct a test station for this measurement and investigate the variations for the Matsushita samples.

4. Does aging affect either the transmittance or the refractive index? We will need to know if the aerogel properties are stable with time. In the past, aerogel transmittance has degraded after a few years in use which has been attributed to moisture absorption. However, the KEK method produces hydrophobic aerogel, which is expected to prevent this effect [12]. This is a situation which needs to be tested and monitored during

production.

In addition to these issues, we will need to construct a test station to measure each aerogel tile manufactured in the production runs, in order to be sure it meets our specifications and in order to be able to monitor the production process for possible difficulties. We have done this in the past for the crystals for the CLEO-III RICH, so we are well aware of the issues involved and the possibilities of production processes drifting out of tolerance.

A.2.6 Alternative Photon Detector System: MAPMTs

In addition to the hybrid photodiodes, we have considered multianode photomultipliers as an alternative choice for photon detectors in the RICH detectors. As illustrated in Fig 5.6, the HPDs offer a cheaper solution. However, acceptable performance can be achieved with the PMT system as well. Thus, it is useful to describe PMT based detector which we consider a back-up option in case the price structure changes or the HPD solution runs into some unexpected obstacles.

In the PMT approach, multianode tubes must be used in order to reach the required accuracy for the detected photon position. Hamamatsu has recently developed the R5900 multianode phototubes which are about 1 inch $\times$ 1 inch in cross-section and are segmented into four (R5900-M4), sixteen (R5900-M16) or sixty-four (R5900-M64) separate anodes. The active area of these tubes is only about 40%. Some kind of light focusing system in front of the PMTs is needed to recover the dead area. The R5900-M16 tubes were adopted for the HERA-B RICH detector [17]. HERA-B used a two-lens system providing demagnification by a factor of two. In the HERA-B solution, the tubes are not closely packed, reducing the cost of the detector but allowing the segmentation error to dominate the achievable resolution. In addition, the photon yield suffers from the reflective losses at each lens surface, further deteriorating particle identification. Light loss for aerogel photons would be even larger than for gaseous photons because of the small angular acceptance of the two lens system. Our simulations show that the two lens system would fall far short of our goals without any cost saving compared to the scheme described below.

A different demagnification system was proposed by R. Forty [18] (see Fig. A.30). A single refractive boundary in front of each Hamamatsu tube provides enough demagnification to recover the dead area of the tube. The convex-plano lens is in direct optical contact with the PMT window preserving good photon yield. High quality acrylic lenses can be formed by injection molding. Many lenses could be molded together as the tubes are closely packed in this approach. We have simulated such a system in our ray tracing Monte Carlo. Variation of the lens' refractive index with photon wavelength was taken into account. When using the M64 tubes, the segmentation error was found to be 0.35 mrad per photon, somewhat smaller than the emission point error, but larger than naïvely expected from the anode size and the demagnification factor. Geometrical and chromatic aberrations in the lens contribute to this error. The M64 tubes are too expensive to make them practical in our experiment. The M16 tubes are a factor of two cheaper than the M64 tubes. They increase the segmentation error by less than a factor of two as the aberration effects become unimportant compared to the

larger anode size. The photon position error for the M16 system is 0.55 mrad per photon (about the same as the emission point error). Overall resolution is only 18% worse for the M16 system than for the M64 tubes. Therefore, R5900-M16 tubes are a possible choice for the BTeV RICH detector.

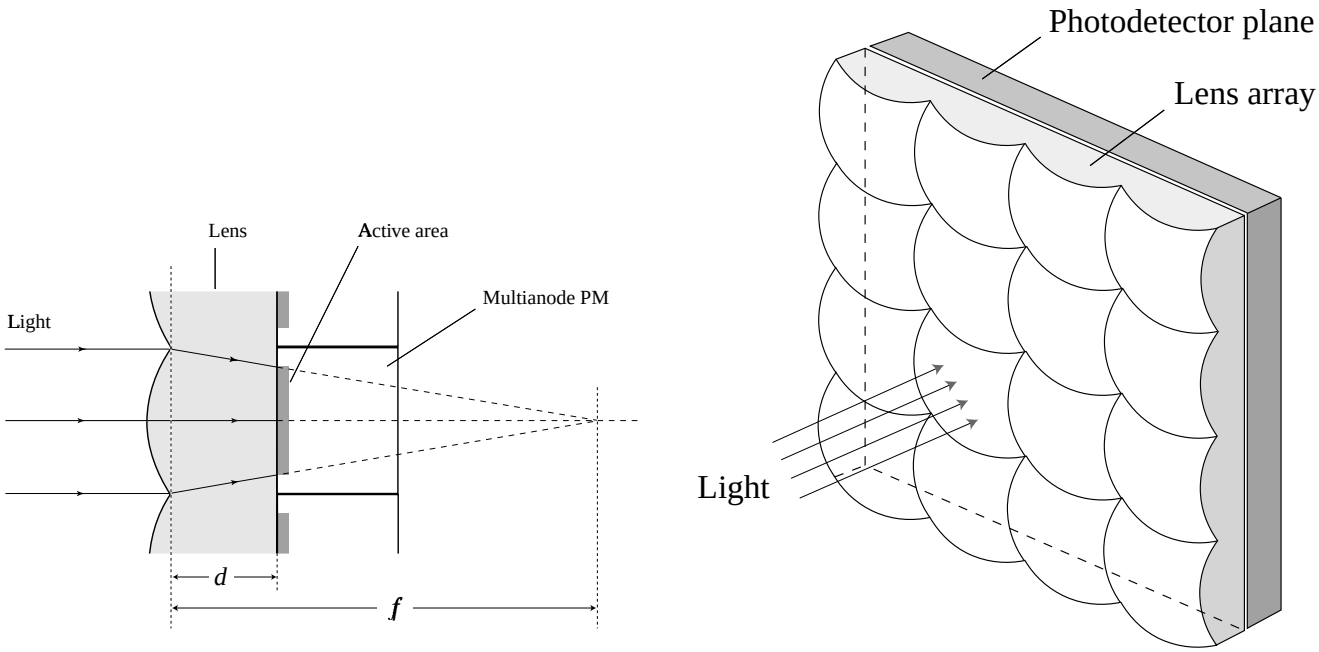

Figure A.30: Two views of the lens system proposed by R. Forty for use with closely packed arrays of Hamamatsu R5900 MAPMTs. The pictures are taken from Ref.[18].

In the PMT approach the wavelengths are limited to visible range by the affordable lens material. PMTs with sensitivity extended to the UV are more expensive since the sealing of quartz windows with a PMT glass envelope is complicated. Thus, standard bialkali photocathode on a borosilicate glass window (with the wavelength cutoff at 300 nm) is adopted, resulting in a chromatic error of 0.33 mrad per photon. On average, 58 photons are expected in the PMT system for a fully contained gaseous Cherenkov ring emitted by a fast particle. The total Cherenkov angle resolution is 0.83 mrad per photon and 0.11 mrad per track.

The particle ID resolution in the PMT option is only slightly worse than projected for the HPD system. Therefore, our choice is dictated by the cost of the photo-detectors. The price of PP0380V HPD tubes is 30% less than for the R5900-M16 multi-anode PMTs for the same area covered. Counting the cost of PMT bases and the lens system would only enlarge the difference. Even though HPDs require much higher voltages than PMTs, they don't draw any current making the HV system more affordable. The number of electronic channels is comparable between the two systems. The lifetime of photo-detectors, radiation hardness and resistance to remnant magnetic fields is sufficient for both types of photo-detectors.

A.2.7 RICH Simulation and Reconstruction Software

Charged tracks that exit the central dipole magnet are input to our RICH simulation package. The physics simulations included an average of two minimum bias events in addition to the $b\bar{b}$ event. Photon conversions in front of the RICH detector were also included. The same RICH simulation package is used in the BTeVGeant and MCFast environments. Cherenkov photons are radiated along charged track intersections with aerogel and gas radiators limited by their geometrical extent, which includes a simulation of the beampipe hole. The dependence of the refractive indices of the C_4F_{10} and aerogel radiators on the photon wavelength is taken from previous measurements. Cherenkov threshold effects are simulated exactly by explicit integration of the Cherenkov formula over wavelengths for each value of the particle velocity. Each Cherenkov photon is traced through the RICH geometry. The light reflection and refraction depends on the photon polarization induced by the Cherenkov radiation process. Absorption at the beampipe, vessel walls and in the gas radiator itself are taken into account. Photons reaching one of the spherical mirrors are reflected towards the photo-detectors. The wavelength dependence of the reflection probability is simulated. The average reflectivity was set to agree with the results achieved in the HERA-B experiment. Each photo-detector tube is represented in the ray tracing, including all geometrical details. The HPD tube has a spherical quartz window which focuses photons onto the photocathode. (In the PMT system, optical focusing by acrylic lenses plays an even bigger role.) We have included the wavelength dependence of the refractive indices and absorption coefficients for quartz and acrylic. The wavelength dependence of the quantum efficiency of the photocathodes is simulated according to the benchmark curves supplied by DEP and Hamamatsu. For HPDs, we introduced a 280 nm cutoff, which can be achieved with an appropriate window coating. Electrostatic focusing of photoelectrons onto the silicon diode is assumed to be linear. The hexagonal pixel geometry is assumed, with 163 pixels per HPD tube. For the multianode tubes we simulate the dependence of the photoelectron collection efficiency on the first dynode, which depends on the point of photon incidence at the photocathode (using data supplied by Hamamatsu).

In the analysis of the Monte Carlo data, we start from charged tracks reconstructed in the tracking system. For each hit recorded in the photo-detectors we calculate a Cherenkov angle for a given track and each mass hypothesis (e, μ, π, K, p), assuming that the photon was radiated at the middle point of the track intersection with the radiator. We store a list of such calculated Cherenkov angles if the reconstructed angle is within $\pm 3\sigma$ of any of these mass hypotheses. Since Cherenkov rings from different tracks intersect each other (see Fig. 5.7), we remove hits from the intersection regions before calculating the per track average Cherenkov angle. This is done in two steps. In the first pass, all hits within $\pm 3\sigma$ to a mass hypothesis are included in the per track average, excluding those hits which are within $\pm 3\sigma$ of the pion hypothesis for any other track. The second pass is essentially the same except that instead of assuming that all tracks are pions in the hit exclusion, the most likely mass hypothesis based on the first pass result is used.

Variables used to discriminate between two mass hypotheses for the same track are described in Section 5.6 of Part II of this proposal. We do not yet use all of the available

information in the most efficient way. Particle identification algorithms need to be refined, especially at lower momenta, where the threshold effects become important. Therefore, we believe that the simulation results presented in this proposal are conservative. Clearly more work on the reconstruction algorithms is needed.

Bibliography

[1] Delft Electronic products B.V., Specification of 72mm Electrostatically Focused Hybrid Photodiode, PP0380, 184-2114A0 (Sep. 1998).

[2] BTeV, BTeV proposal - Appendix A - Data Acquisition System.

[3] E. Nygard *et al.*, Nucl. Instr. and Meth. **A301** (1991) 506.

[4] IDE AS, *IDE Front End ASICS*, (1997).

[5] M. Tanaka *et al.*, Nucl. Instr. and Meth. **A432** (1999) 422.

[6] B. Alpat *et al.*, Nucl. Instr. and Meth. **A439** (2000) 53.

[7] M. Overdick *et al.*, Nucl. Instr. and Meth. **A392** (1997) 173.

[8] M. Artuso Nucl. Instr. and Meth.**A409** (1998) 375.

[9] M. Artuso *et al.*, Nucl. Instr. and Meth. **A419** (1998) 577.

[10] A. Braem *et al.*, Nucl. Instr. and Meth. **A433** (1999) 153.

[11] D. Ryckbosch *et al.*, Nucl. Instr. and Meth. **A433** (1999) 98.

[12] T. Sumiyoshi *et al.*, Nucl. Instr. and Meth. **A433** (1999) 385.

[13] I. Adachi *et al.*, Nucl. Instr. and Meth. **A355** (1995) 390.

[14] A.R. Buzykaev *et al.*, Nucl. Instr. and Meth. **A433** (1999) 396.

[15] A.F. Danilyuk *et al.*, Nucl. Instr. and Meth. **A433** (1999) 406.

[16] E. Nappi, ICFA Instrumentation Bulletin **17** (Fall 1998).

[17] J.L. Rosen, Nucl. Inst. and Meth. A408 (1998) 191; S. Kopar, Proceedings of the The 3rd Int. Workshop on Ring Imaging Cherenkov Detectors Weizmann Institute of Science Ein-Gedi, Dead-Sea, Israel, Nov., 1998.

[18] R. Forty, "Use of lenses to increase the RICH photo-detector coverage", LHCb Internal Note LHCB/98-038.

A.3 Electromagnetic Calorimetry

A.3.1 Introduction

A thorough investigation of B decays requires the ability to study final states including single photons, π^0's, and η's. Among these are some of the important decay modes mentioned in Part 1:

- $B^0 \to (\rho\pi)^0 \to \pi^+\pi^-\pi^0$;
- $B^0 \to K^{*0}\gamma$ and $\rho^0\gamma$;
- $B_s^0 \to \psi\pi^0$, $\psi\eta$, and $\psi\eta'$;
- $B^0 \to K^{*0}\pi^0$; and
- $B^\pm \to K^\pm\pi^0$ and $\pi^\pm\pi^0$.

In addition to reconstructing photons, the electromagnetic calorimeter will be used to identify electrons. This has critical application in CP studies: B-tagging with the semileptonic decays $B \to D^{(*)}e\nu$, and the reconstruction of exclusive B decays into J/ψ or ψ'.

To study these decays, one needs to separate small signals from background, a major challenge in the hadron-collider environment. The requirements for the BTeV calorimeter are similar to those for the CMS experiment at the LHC: excellent energy and position resolution (little inactive materials), compact shower size to minimize overlapping showers (small Moliere-radius materials), fast signal (to minimize shower overlaps in time), and radiation hardness. Among the materials that were known to have potential to satisfy these requirements were inorganic scintillation crystals such as $PbWO_4$ (PWO) and CeF_3. CMS chose PWO scintillation crystals. Taking advantage of the enormous R&D effort already carried out for CMS, we have decided to develop a design for an electromagnetic calorimeter based on PWO crystals. Since we can use PMT's (photomultiplier tubes) instead of CMS's APD (avalanche photodiodes) or VPT (vacuum phototriodes), our resolution will be better than that of CMS, particularly at energies below 10 GeV. This energy range is particularly important for BTeV.

A.3.2 Radiation Tolerance and Radiation Levels

Radiation damage of PWO crystals is a serious issue. Detailed studies [2] reveal that the light transmission of crystals deteriorates due to formation of color centers by radiation, while the scintillation mechanism itself seems unaffected. When a PWO crystal no longer receives radiation, its color centers (semi-stable excited states) disappear, and it recovers from transmission degradation by natural room-temperature annealing. In fact, this annealing goes on even during radiation exposure. Therefore, when crystals are exposed to a constant radiation level, they lose light only up to the point where the rates of radiation damage and natural recovery balance.

For the majority of crystals at CMS (all barrel crystals and 25% of endcap crystals), the expected radiation dose rate is less than 0.15 Gy/hour [3]. At this rate the CMS production crystals lose only a few per cent of their light output. For about 10% of the endcap crystals, the radiation dose rate will be as high as 18 Gy/hour. Even at this rate, the light loss saturates at less than 20% [4]. This reflects the fact that the density of crystal defects, which can turn into color centers, is limited in these high-quality crystals.

This level of radiation sensitivity is perfectly acceptable for BTeV, where most crystals will incur less than 0.1 Gy/hour, and only a few crystals receive more than 1 Gy/hour. To make these estimates, we have carried out a full calculation of the radiation environment, accounting for both the direct products of collisions and the secondary particles produced in interactions with the material of the BTeV detector [5]. To calculate the radiation levels in the crystals and the phototubes, a full Monte Carlo simulation using the MARS (IHEP) code was performed [6]. MARS is the standard IHEP package used for radiation environment calculations for both the CMS and LHC-b projects at CERN [7]. We used Pythia to generate minimum bias events for input to MARS. At a luminosity of $2 \times 10^{32}\mathrm{cm}^{-2}\mathrm{s}^{-1}$, assuming an inelastic cross-section of 60 mb, the Tevatron produces 1.2×10^7 inelastic $\overline{p}p$ events per second. Together with particles produced in interactions with detector material, this produces a decidedly hostile radiation environment.

Each year of BTeV operation was assumed to be 10^7 seconds, the same unit as was used in the physics sensitivity estimates. In Fig. A.31 we show the annual per-crystal dose (at shower maximum, 4-7 cm behind the front face of the EMcal) as a function of position transverse to the Tevatron beamline.

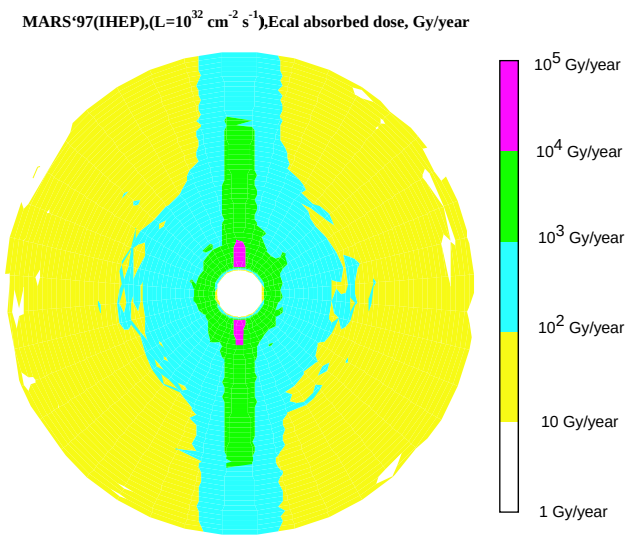

Figure A.31: Annual radiation dose in crystals at shower maximum. Note that a yearly dose of 1 kGy corresponds to a dose rate of 0.3 Gy/hour.

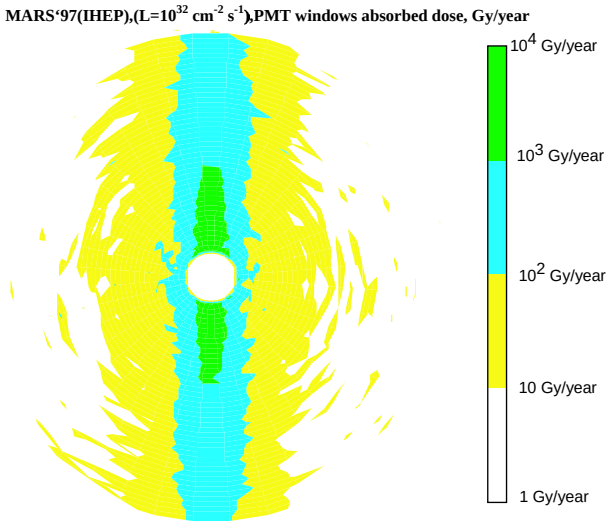

Figure A.32: Annual radiation dose at PMT windows.

The annual radiation dose exceeds 10 kGy (3 Gy/hour) for a small number of crystals at the smallest radii just above and below the beamline. This is because a portion of the intense flow of charged particles near the beamline, which mostly pass through the hole of 15 cm radius in the middle of the calorimeter, are deflected vertically by the dipole magnet. The highest dose is 30 kGy/year or 10 Gy/hour. This is still only 1/2 of the maximum dose rate CMS expects. Fig. 6.3 (in Part 2) shows the fraction of the BTeV crystals below a given dose rate, which is shown on the horizontal axis. One can see that 90% of the crystals receive dose rates less than those for the CMS barrel crystals.

The PMT windows can potentially also suffer radiation damage. Here our concern is the total dose, since there is no recovery mechanism. The same simulation as described above indicates that the maximum dose near the Tevatron beamline is 7 kGy/year. Fig. A.32 shows the radiation level at the PMT's as a function of their location. From this study, we conclude that the majority of the PMT's must have either quartz or radiation-tolerant glass windows [9].

A.3.2.1 Expected Energy Resolution and Efficiencies

The energy resolution that we can expect from a PWO system will depend on several factors, but it can be parameterized as a function of the incident energy E as

$$\frac{\sigma_E}{E} = \sqrt{\frac{S^2}{E} + C^2} \equiv \frac{S}{\sqrt{E}} \oplus C \quad . \tag{A.15}$$

The first term, the "stochastic term," is due to fluctuations in the leakage of shower energy to crystals surrounding the main cluster of crystals (transverse shower leakage). Since the number of photoelectrons detected by the PMT's fluctuates appreciably, it also contributes to this stochastic term. We will evaluate this term below. The second term, the "constant term," arises from variations in light output along the crystal length and errors in the relative calibration between crystals. Fluctuations in the energy escaping from the rear of the crystals also contribute to this term.

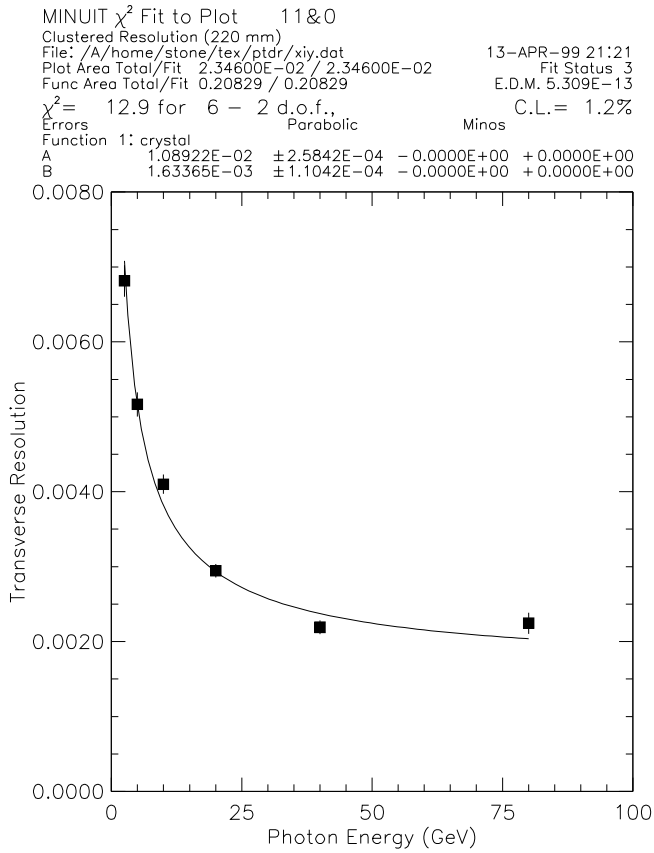

Figure A.33: Energy resolution as a function of incident photon energy for 220 mm long crystals and 5x5 clustering.

We can use the energy resolution expected by CMS to guide our expectations. CMS based their study on an assumption of 4 photoelectrons/MeV read out by two APD's. There is an excess noise factor in the APD's due to correlated gain, effectively giving a factor of two reduction in the number of photons. Thus photostatistics gives a contribution of $2.3\%/\sqrt{E}$ to the expected CMS resolution. The term for lateral containment was studied for a 5×5 array of 22×23 mm^2 crystals, for which CMS found a contribution of $1.5\%/\sqrt{E}$. Adding these together in quadrature gives $2.7\%/\sqrt{E}$. They estimated the constant term to be 0.55%. CMS also included extra noise, which is constant in σ_E, due to leakage currents in the photodiodes, and the effect of summing over ~25 interactions per crossing, each with

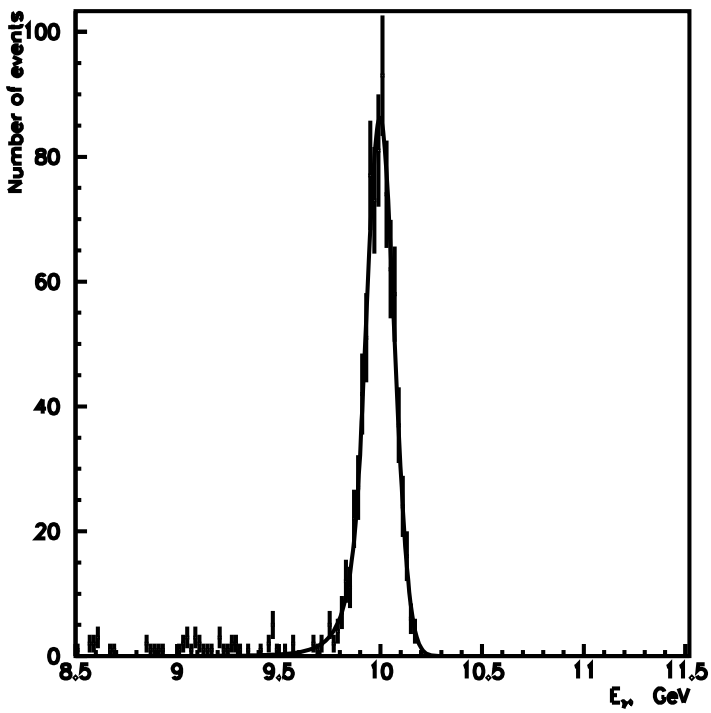

Figure A.34: Distribution of measured photon energies for 10-GeV photons using a realistic clustering algorithm. The curve shows the result of a fit to a resolution function.

7 times more energy than the Tevatron. These effects are not present for BTeV.

Additional guidance can be found by reviewing the performance of the KTeV CsI calorimeter. They have achieved [10]

$$\frac{\sigma_E}{E} = \frac{2\%}{\sqrt{E}} \oplus 0.45\%. \tag{A.16}$$

The dominant contribution to the constant term seems to be dependence of the response on the position on the face of the crystal where the photon is incident. This effect was not observed in the CLEO CsI calorimeter [11].

The photon statistics term for BTeV, taking 7 photoelectrons/MeV, is expected to be $1.3\%/\sqrt{E}$, including the correlated gain factor for the PMT of 1.2.

The energy resolution determined with a GEANT-based simulation of 220 mm long crystals, without photon statistics or electronic noise, is shown in Fig. A.33. It can be parameterized as

$$\frac{\sigma_E}{E} = \frac{a}{\sqrt{E}} \oplus b, \tag{A.17}$$

where $a = 1.1\%$ and $b = 0.2\%$, and E is in GeV. The stochastic term a comes mainly from transverse leakage, while the constant term arises mainly from longitudinal leakage.

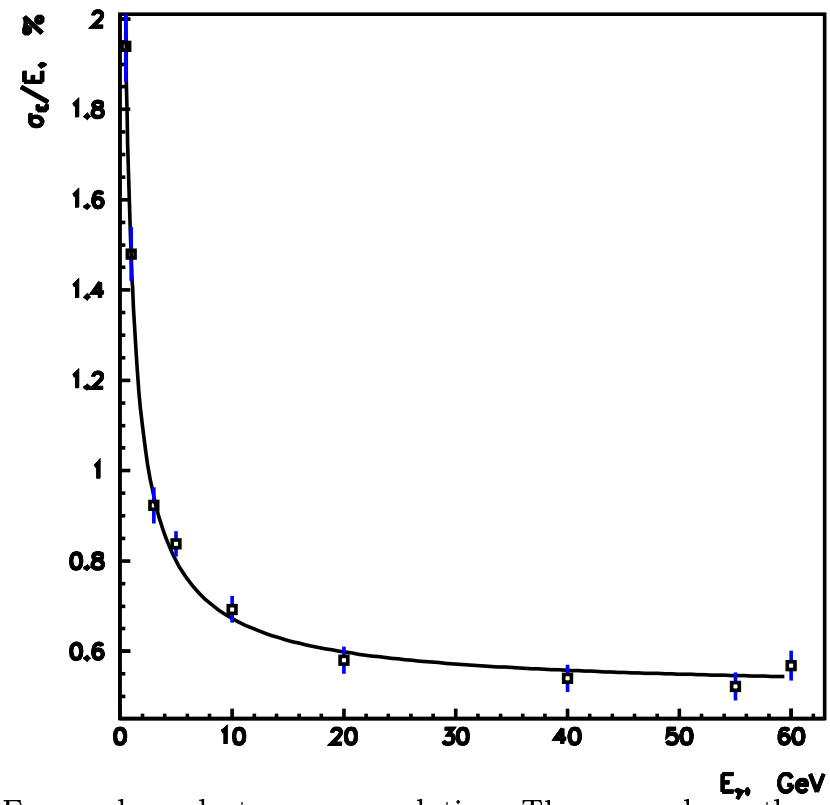

Figure A.35: Energy-dependent energy resolution. The curve shows the result of a fit to a resolution function.

Adding the two stochastic components in quadrature gives $1.6\%/\sqrt{E}$. We take the CMS estimated value of 0.55% for the constant term and find an expected energy resolution for BTeV of

$$\frac{\sigma_E}{E} = \frac{1.6\%}{\sqrt{E}} \oplus 0.55\%. \tag{A.18}$$

Fig. A.34 shows the distribution of measured energies for a Monte Carlo simulation of 10 GeV photons. The effect of photon statistics was included in the simulation. The curve shows the result of a fit to a photon resolution function [13]. The resolution is about 0.7% at 10 GeV. Fig. A.35 shows energy dependence of the energy resolution, and the result of the fit to Equation (1). The fit results indicate that the constant term of the resolution is 0.5% and stochastic term is 1.4% at 1 GeV, which is consistent with Equation A.18 above.

The efficiency for detecting photons in a clean event environment is about 80%, independent of energy. Most of the loss comes from conversions in material in front of the calorimeter. This efficiency clearly depends additionally on the event environment and the number of interactions per crossing.

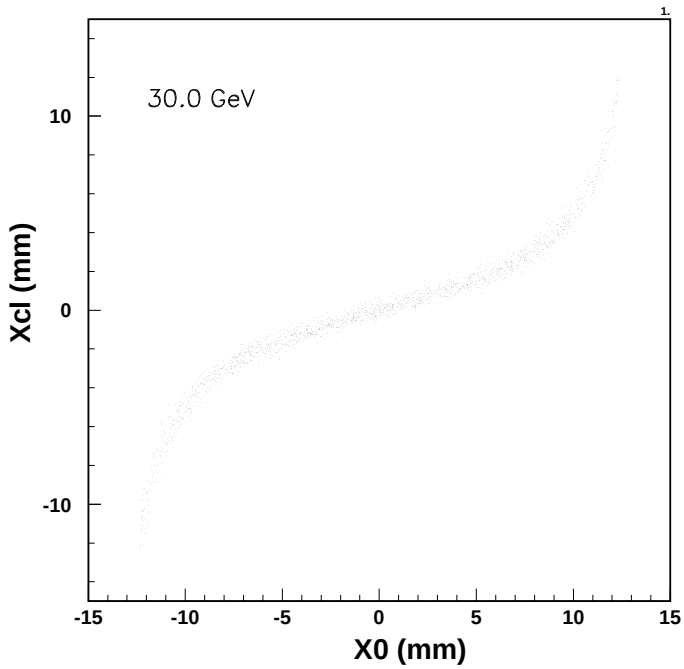

Figure A.36: Measured photon position x_{Cl} versus known photon position x_0 for 30 GeV photons.

A.3.2.2 Position Resolution

The BTeV electromagnetic calorimeter is 7 meters from the center of the dipole magnet, so the resolution of the projected angle is given to first order by the error in the transverse position divided by 7 meters. This is particularly important for high-energy π^0's, since the opening angle of the photon pair is small. We used GEANT to simulate the energy deposit in 220 mm long crystals. Positions were determined in both directions transverse to the crystal axes. The position of the reconstructed photon is determined from the energy deposited by using the formula:

$$x_{\mathrm{cl}} = \frac{\sum_{i=1}^{25} x_i \cdot E_i}{\sum_{i=1}^{25} E_i}, \tag{A.19}$$

where E_i is the energy reconstructed in each crystal, x_i is the position of the center of each crystal, and the sum extends two crystals in each direction from the highest energy crystal.

Fig. A.36 shows x_{cl} versus the true position of the photon, x_0, for a sample of simulated 30 GeV incident photons. The characteristic "S-curve" shape is apparent. To evaluate the position resolution, the overall shape of the S-curve is removed by a fit to give a corrected cluster position x_{corr}. In Fig. A.37, the distribution in $\Delta x = x_{\mathrm{corr}} - x_0$ is plotted. The width of this distribution is the r.m.s. position resolution.

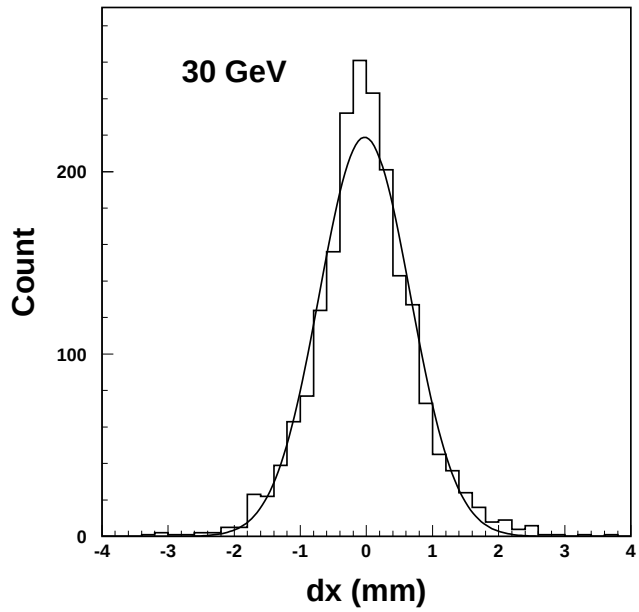

Figure A.37: Distribution of $\Delta x = x_{\text{corr}} - x_0$ for 30 GeV photons. The fit is a Gaussian with mean consistent with zero and $\sigma = 0.7$ mm.

The results of performing this study over a range of energies are shown in Fig. A.38, which shows the r.m.s. position resolution as a function of energy using full BTeVGeant simulations and a realistic clustering algorithm. The fit gives

$$\sigma_x = \frac{3.1\text{mm}}{\sqrt{E}} \oplus 1.7\text{mm}. \tag{A.20}$$

This position resolution implies excellent angular resolution. At 6 GeV, the r.m.s. angular resolution is 0.3 mrad.

A.3.3 Design Parameters

A.3.3.1 Projective *vs.* Non-projective Geometry

It is well known that calorimeters with projective geometry perform better than non-projective ones. The projective structure minimizes shower overlaps and provides better position resolution. Fabrication of the calorimeter, on the other hand, may be more complex with a projective geometry and may result in higher cost.

CLEO's endcap calorimeter has a non-projective geometry. This decision was made to simplify its construction, since it was possible simply to stack crystals one on top of another. Detailed Monte Carlo studies showed the performance of this calorimeter to be comparable to that of a projective-geometry alternative. This is because the angular resolution plays a negligibly small role compared to the energy resolution for all measurements relevant to the

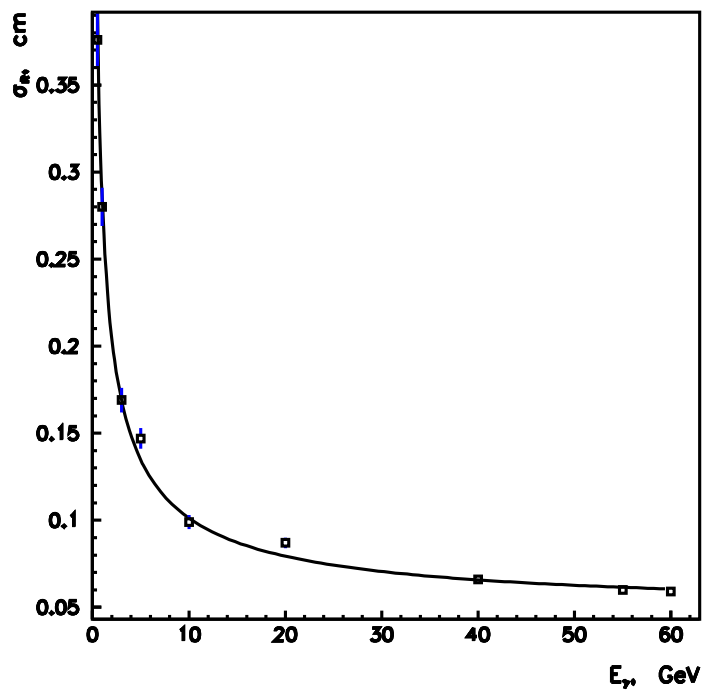

Figure A.38: Energy-dependent position resolution. The curve shows the result of a fit to resolution function.

CLEO physics program, including the π^0 mass resolution. This conclusion is specific to the physics of an e^+e^- storage ring at a center-of-mass energy of $\sim$ 10 GeV, where all particles decaying into photons are of quite low energy.

For BTeV, the deterioration of position resolution for rectangular crystals is as much as 2 mm. This will degrade the π^0 mass resolution above 10 GeV. No other negative effects of a non-projective calorimeter design have been identified at the time of this writing.

PWO crystals are too fragile to stack up one on top of another - with sufficient weight over them the crystals would fracture. In the absence of clear cost advantages, we have therefore decided to adopt a projective geometry as our baseline design for the BTeV calorimeter. If we find a way to make a non-projective (rectangular crystal) calorimeter more cheaply, and if there is no additional physics case for the projective geometry, we will likely change our baseline design.

A.3.3.2 Lateral Size

The lateral size of the crystals should be comparable to the Moliere radius of PWO to provide the best performance. We use 25.4×25.4 mm^2 in the front and 26×26 mm^2 in the back, somewhat smaller than the design for the CMS endcap crystals [12]. Anything larger would compromise the position resolution and increase overlapping showers, but would reduce the cost of PMT's and electronics. A smaller lateral size would increase the cost substantially, particularly because we would need to use custom-size PMT's.

A.3.3.3 Crystal Length

The crystal length for the BTeV calorimeter has been determined with a study of GEANT-simulated showers, the results of which are summarized in Fig. A.39. The distributions of the detected energies for samples of simulated 80-GeV photons (normalized to the true energy) are shown for crystal lengths ranging from 170 mm to 230 mm. It is clear that the loss in energy resolution in going from 230 mm to 220 mm is minimal, but as one goes to shorter lengths, the energy resolution suffers.

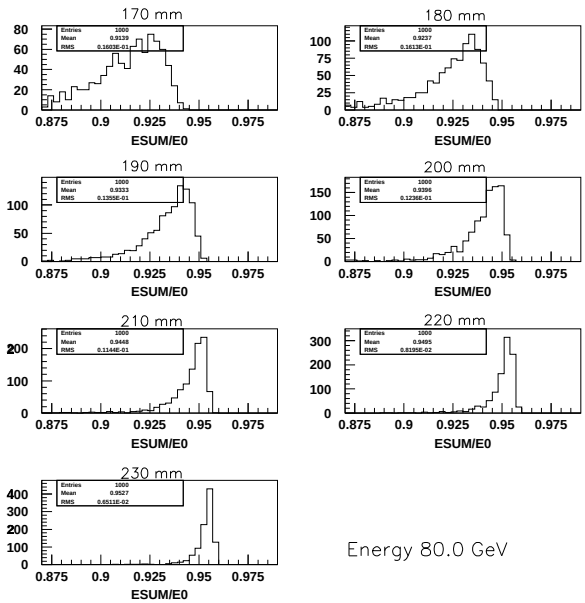

Figure A.39: Energy deposited for 80 GeV/c photons normally incident on $PbWO_4$ crystals of the labeled lengths.

The normalized energy distributions for GEANT events with different energy photons and crystal lengths between 210 and 230 mm were fitted with resolution functions developed for the Crystal Ball experiment [13]. An example of such a fit is shown in Fig. A.40. The values of the energy resolution for the cases considered in this study are shown in Fig. A.41. The energy resolution is minimally affected by shortening the crystals from 230 mm to 220

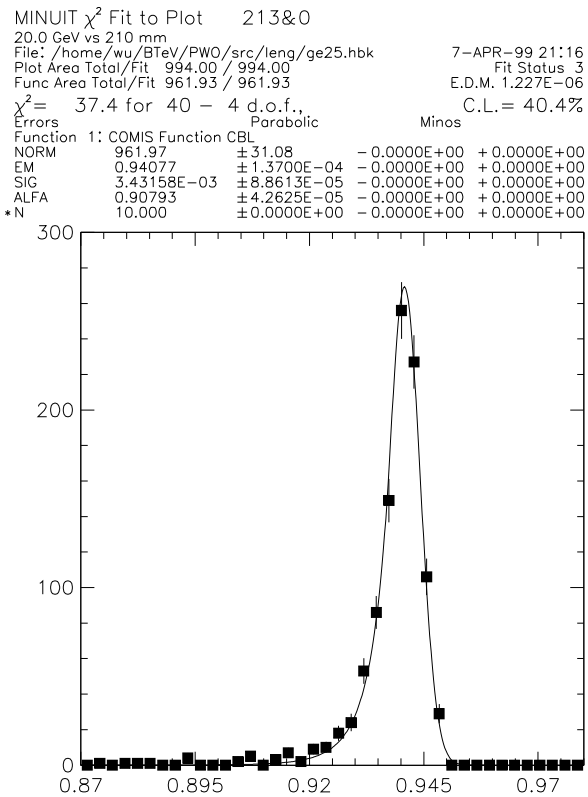

Figure A.40: Fit of the normalized clustered energy deposit for normally incident 20 GeV photons in crystals of length 210 mm. The fitted line shape is from the Crystal Ball experiment.

mm, but there is a significant degradation in going to 210 mm. This study uses the energy deposited in 5x5 arrays of crystals. Smearing due to photon statistics has not been included, so the resolutions are unreasonably good. Based on these studies, we decided to use 220 mm long crystals.

A.3.3.4 π^0 Mass Resolution

We have also studied the mass resolution for π^0 decays to photon pairs. Fig. A.42 shows the distributions of two-photon invariant masses when the initial π^0's have energies of 5, 10 and 30 GeV. We observe an excellent resolution of less than 3 MeV when the π^0 energy is between 2 and 10 GeV [15]. It degrades slightly at higher energies where the angular resolution starts to contribute. At energies lower than 2 GeV, the mass resolution also degrades, in this case because the stochastic term in the photon-energy resolution becomes significant.

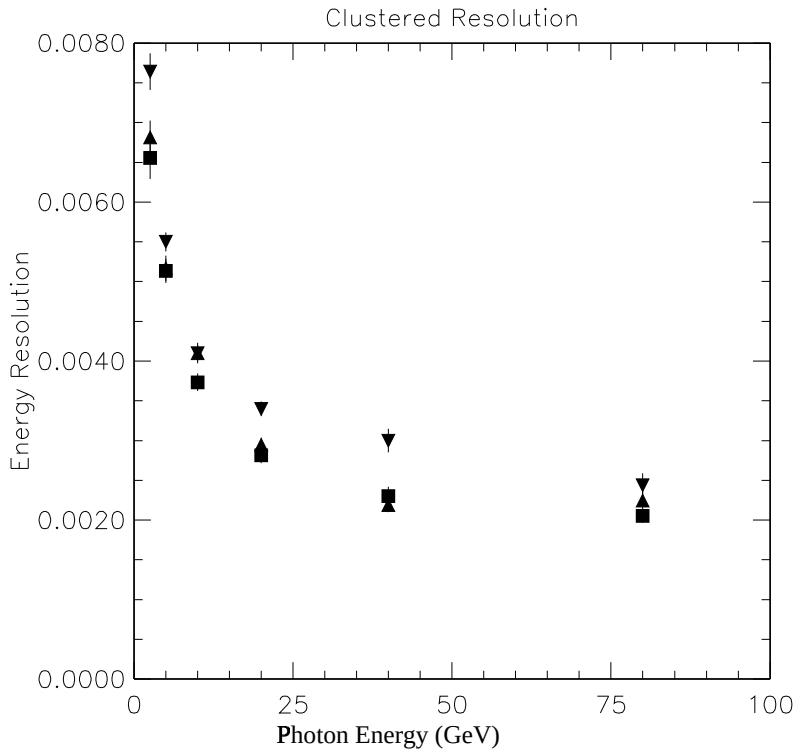

Figure A.41: Energy resolution as a function of incident photon energy for different crystal lengths using 5x5 clustering. The squares are for a crystal length of 230 mm, the triangles for 220 mm and the inverted triangles for 210 mm.

A.3.3.5 Merged π^0

It is clearly quite important that BTeV be able to distinguish photons from π^0's. Many of the π^0's will be fast and could in principle appear as single clusters. To study how well we could separate these two components with the proposed transverse segmentation, we generated samples of both γ's and π^0's at a variety of energies.

To study the probability of overlaps quantitatively, we calculated the second-moment mass or cluster mass, which is described in Section 14.3 (ECAL Cluster Finder). The cluster mass distributions for both photons and π^0's of fixed energies are compared in Fig. A.43. They are well separated up to 60 GeV, but they start overlapping at 70 GeV. In Table A.3 we show the photon detection efficiency for selection criteria with $\pi^0 \rightarrow \gamma\gamma$ rejection probabilities of 90% and 99%. Since most of the photons and neutral pions of interest in BTeV are below 60 GeV, the photon-π^0 discrimination achieved with this design is excellent.

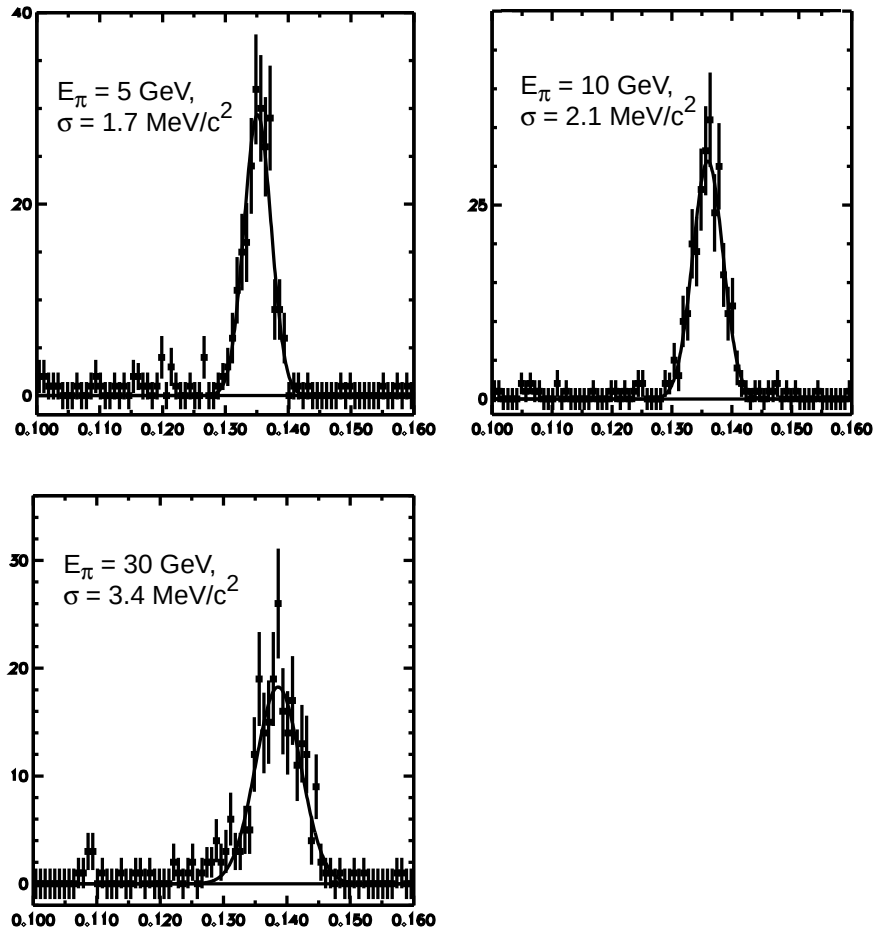

Figure A.42: Two-photon invariant mass distributions for simulated π^0's of energy 5, 10 and 30 GeV.

A.3.4 Mechanical Systems

Since no design work on the BTeV calorimeter mechanical support system has yet been done, the baseline assumes that we will adapt the CMS endcap design. It has many nice features, but is expensive. If we can use a CLEO-like approach, the cost could go down substantially. One of the major obstacles to this is the fragility of PWO crystals, which are very sensitive to mechanical stress. As has been mentioned, they cannot simply be stacked, because the crystals near the bottom are likely to crack from the weight above.

CMS chose to use a structure made of "alveolar cells." These are molded from glass fiber and resin for the barrel and carbon fiber for the endcaps. Crystals are held individually, so that the alveolar cells bear the weight. In the CMS endcap design, the alveolar cells are cantilevered from the strong back, which is the major structure member of the endcaps.

Table A.2: Reconstructed π^0 mass resolution.

π^0 Energy (GeV)	Resolution (MeV)
1	4.6
2	2.6
5	1.7
10	2.1
30	3.4
40	4.9

Table A.3: Photon detection efficiencies for 99% π^0 rejection

Energy (GeV)	γ efficiency for 90% π^0 rejection	γ efficiency for 99% π^0 rejection
40	100	99.8
50	99.7	99.7
60	99.5	93
70	93	64

There is 0.4 mm of alveolar materials between crystals, but this design avoids any materials in front of the endcaps.

The major cost for this design is in the production of alveolar cells, over $1M for the 80,000 crystals in CMS. The Babar experiment used a similar design for their CsI calorimeter, and their cost was comparable to CMS.

A.3.5 Crystal Acquisition

For PWO crystals to be fast and radiation hard, they need to be produced very carefully. Any impurities and crystal defects, like Pb and O vacancies, increase both the slower components of the light output, and the radiation susceptibility. Therefore, establishing mass production procedures to produce good crystals has been one of the major goals of the R&D program of the CMS calorimeter group and its vendors at the Bogoroditsk Plant in Russia and the Shanghai Ceramic Institute.

They have realized this goal by concentrating on the following five factors:

- economical raw material purification methods
- adjustment of the stoichiometric ratio between PbO and WO_3 in the raw material to compensate for the evaporation of PbO during crystal growth
- environmental gas during the crystal growth

- annealing methods
- doping of Y, La and/or Nb to compensate residual crystal defects.

The Russian manufacturer uses the Czochralski method to grow crystals. Before embarking on their PWO R&D project with CMS, they already owned more than 100 ovens, which had previously been used to grow other kinds of crystals. They have already succeeded in producing good PWO crystals for the CMS barrel calorimeter, and have in fact produced more than 6000 production crystals in the past year. The Russian manufacturer still needs to complete additional R&D before it can produce larger and radiation-hard crystals with high production yield for higher-radiation endcap calorimeters (up to 18 Gy/hour or 25 kGy/year).

The Chinese producer uses the Bridgeman method to grow crystals. Due to its prior commitment to other HEP experiments, it did not start production R&D until after the Russians. Nevertheless, the Chinese can already produce good barrel crystals, although it needs to improve its production yield more to be able to reduce the production cost below the quoted price.

We have visited both the Bogoroditsk and Beijing/Shanghai production facilties, hosted by our Russian IHEP and Chinese colleagues. Both companies are interested in growing crystals for BTeV at the same price they have promised to CMS, $1.60/cc. They plan to finish production for CMS by the middle of 2005 by producing 7000 crystals per year at Bogoroditsk and 10000 crystals per year in China. Some capital investment on our part will be necessary to start crystal production prior to the CMS completion. We believe an upfront investment of $0.8-1.6M is sufficient to start BTeV production either at Russian and Chinese plant, and will provide enough crystals for one calorimeter by 2005.

There are two other potentially interested sources for PWO crystals. One new source is at Shandong University. One of the physicists there has joined BTeV, and more are interested in joining BTeV. The Shandong University HEP group forged a collaboration with their university's Institute of Crystal Materials when it became clear that PWO crystals may be powerful tools to study b hadrons. The institute has grown a multitude of crystals for different purposes, many of which have been for laser applications. They have mastered various crystal growing technologies, including the Czochralski method. They have grown a handful of PWO crystals which are visually clearer than the first crystals grown in Russia several years ago, indicating that they already have good control of impurities and crystal defects. Although those crystals were smaller in size than we need, the Institute is eager to carry out an R&D program this year to produce full-size sample crystals by the end of 2000.

Many of the results of the R&D work done by the collaboration of CMS and the Bogoroditsk plant have been published, but some of the important details are proprietary. It therefore may take some time for Shandong University to be able to produce truly radiation hard full-size crystals at an acceptable production cost.

Meanwhile, it is crucial that BTeV develop capabilities to measure important crystal characteristics such as radiation tolerance, so that we can give quick feedback on the qualities of its crystals to the Crystal Institute at Shandong.

The Japanese firm, Furukawa, has worked with a KEK physicist to produce radiation hard PWO crystals for almost as long as Russians and CMS. They are the largest producer of Cadmium Tungstate crystals in the world, but they have not done much work to minimize production cost of PWO crystals. Consequently, their current production cost of PWO is about 3 times higher than the Russian and the Chinese. They are interested in producing PWO crystals for BTeV and are working on lowering their cost. One attractive option for them as well as for us is a possible collaboration between Furukawa and Shandong University, combining Furukawa's existing know-how about PWO production with lower Chinese labor costs. This collaboration has potential for producing good and affordable crystals in a relatively short time scale.

A.3.5.1 Calibration Systems

Good calibration systems and procedures are essential to realize the BTeV calorimeter's potential for excellent resolution. It is a challenging task to maintain the calibration to better than 0.5%, particularly when changes in radiation levels can affect the calibration. Since the radiation levels are different for different parts of the detector, the resulting changes in calibration also vary over the calorimeter. Fortunately, the maximum variation is expected to be less than 2%(0.5%) for 90%(50%) of our crystals.

Although the light output of PWO crystals depends strongly on the temperature (-2%/C), we will manage this problem by maintaining a very stable temperature for all of the crystals. This requires careful monitoring, but poses no serious obstacles.

Ultimately, we need to use physics events to calibrate every crystal so that we know how to convert the signals from the crystals to photon energies. We plan to use the electron sample from B semileptonic decays to calibrate every crystal.

The calibration can be checked using π^0, η and J/ψ particles, since their masses are well measured. Fig.A.44 shows a clear π^0 peak in B events at outer radii.

Unfortunately, we will not have enough of these physics events to calibrate every crystal every hour. So we will need to have a calibration system that will track the changes in the calibration over time, and relative to neighboring crystals.

Since we have not done any R&D on such a calibration system, we again draw on CMS R&D results. CMS plans to use a laser light source and optical fiber light distribution system to monitor the time variation of calibration. The light source needs to simulate both the color and the time structure of PWO scintillation light ($\sim$ 500 nm in wavelength, pulse width of 100 ns) and powerful enough to light many crystals at the same time. If the power of a light pulse simulates 100-GeV photons (*i.e.* 10^7 scintillation photons), the light source needs to produce 0.2 mJ of energy in each pulse. The output is sent to one of the 80 sections of about 1000 crystals through a "switch." After the switch, the light travels through two levels of splitters and quartz fibers to reach individual crystals. The light intensity is monitored at the source as well as after the two levels of splitters using PIN photodiodes. The overall objective is to maintain calibration of individual crystals to within 0.2% accuracy over time. KTeV as well as other FNAL experiments employ similar systems.

A.3.6 BTeV Electromagnetic Calorimeter R&D Program

We plan to acquire a small number of crystals from Russia and Shanghai, and some PMT's from Hamamatsu to get experience by looking at signals from radioactive sources. Performing our own studies on the effect of intense radiation on the light output and light transmission of these crystals will be valuable.

Since the stability of the PMT's is important for the performance of our detector, we also plan to study this.

When a test beam becomes available, we will want to expose a 5×5 (or better 7×7) stack of crystals to an electron beam to study the resolution, leakage, temperature sensitivity, and other parameters. We will also conduct further studies of the radiation effects. This study may be possible with a high-energy radioactive source, which produce photons or electrons of energies larger than 10 MeV.

We need to build equipment to characterize crystals (measuring transmittance and emission spectrum analyser). A radiation facility to test the radiation hardness is also important. It is urgent to help Shandong University Crystal Institute to make fast progress in their PWO crystal production R&D. One way to accomplish this would be to provide them with equipment for crystal characterization, particularly to test radiation hardness.

Although PWO crystals are "radiation hard", their light output varies as the radiation level varies. We need to study whether the light-injection calibration method can track this variation with sufficient precision. The planned calibration system will not simulate the spectrum of the light perfectly, nor are the mean path lengths that light travels in the crystals the same. By choosing the wavelength properly, the CMS people find that the system is likely to work well [14]. It will be necessary for us to test this ourselves.

We need to start studying the accuracy of the calibration of the energy scale using the physics processes mentioned above.

We also need to start designing a realistic mechanical structure, and the temperature control system. We will have to explore cost issues with phototube manufacturers.

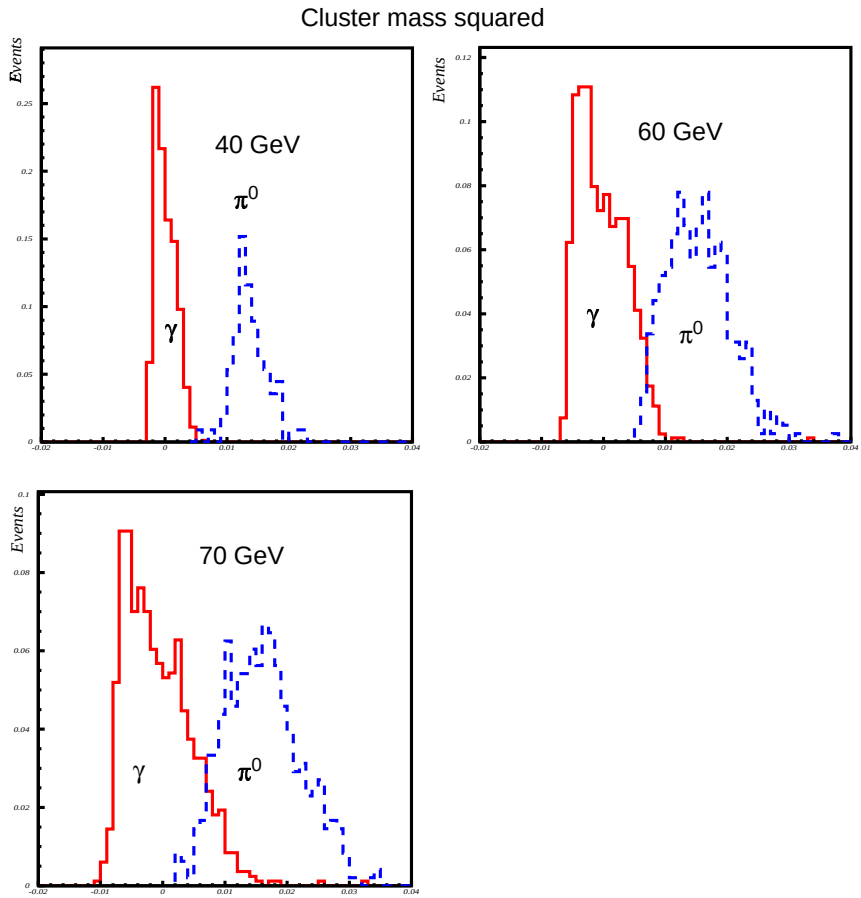

Figure A.43: Cluster mass distribution for γ's and π^0's obtained with a full BTeVGeant simulation. Energy of the photons and π^0's is 40 GeV, 60 GeV and 70 GeV, as indicated.

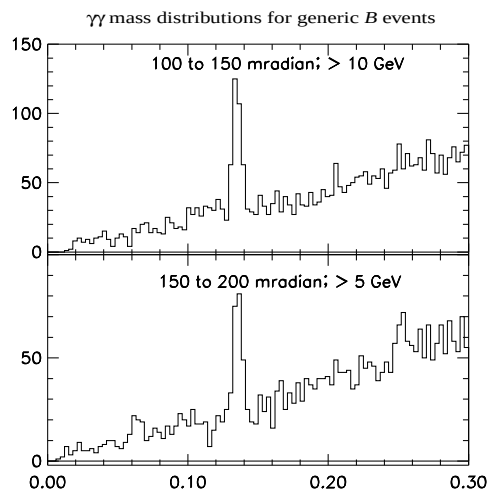

Figure A.44: $\gamma\gamma$ mass distribution for events containing a B event as well as a few minimum-bias events. The energy of the π^0 candidates are required to be greater than 10 GeV (top) and 5 GeV (bottom), respectively.

Bibliography

[1] Although the quantum efficiencies of photocathodes of PMT's are lower than APD's that CMS uses, they cover much larger areas of the end of PWO crystals.

[2] A.N. Annenkov *et al.*, "Systematic Study of the Short-Term Instability of $PbWO_4$ Scintillator Parameters under Irradiation," CMS Note 1997-055.

[3] The output results are given in units of absorbed dose (Gy/year). Note that 1 Gray [J/kg] is equivalent to 100 rads.

[4] "Radiation damage Kinetics in PWO crystals," CMS Note 1997-008.

[5] To a much lesser degree, some radiation results from beam halo and when beam particles which are deflected at small angles get backscattered by accelerator elements outside the BTeV detector. Their contributions are small enough to be ignored.

[6] I.Azhgirey,I.Kurochkin and V.Talanov, "Development of MARS Code Package for Radiation Problems: Solution of Electro-Nuclear Installations Design, Proc. XV Conf. on Charged Particles Accelerators, Protvino, October 1996.

[7] CMS Collaboration, "The Muon Project Technical Design Report", CERN/LHCC 97-32, CMS TDR 3 (1997); A.Uzunian," CMS Radiation Studies Results'99", Fourth Annual RDMS CMS Collaboration Meeting, CMS Document 1999-113, CERN (1999).

[8] CMS, "The Electromagnetic Calorimeter Project Technical Design Report," CERN/LHCC 97-33, CMS TDR 4 (1997).

[9] Hamamatsu Photonics K. K., "Photomultiplier Tube," p. 176 (1994). Beware the units are Roentgens not rads. Here 1 Roentgen is approximately 2 rads. U. V. glass windows lose about 10% of their transparency with a 3 kGy dose, and therefore are not an acceptable solution except on the outside in the horizontal plane, where there are alot of crystals.

[10] Private communication from Ed Blucher.

[11] E. Blucher, B. Gittelman, B. K. Heltsley, J. Kandaswamy, R. Kowalewski, Y. Kubota, N. Mistry, A. Bean, and S. Stone, "Tests of Cesium Iodide Crystals for an Electromagnetic Calorimeter," Nuclear Instruments & Methods **A249**, 201 (1986).

[12] CMS Endcap crystal size has changed to 30×30 mm^2 to reduce electronics cost after they confirmed that Bogoroditsk Plant can grow larger crystals.

[13] T. Skwarnicki, "A Study of the Radiative Cascade Transitions Between the Upsilon-Prime and Upsilon Resonances," DESY F31-86-02 (thesis, unpublished) (1986).

[14] "A Study of the Monitoring of Radiation Damage to CMS ECAL Crystals, Performed at X5-GIF," CMS NOTE 2000-020

[15] In part 2, chapter 6, we quote 2.6 MeV mass resolution for 10 GeV π^0's, which was found using a non-optimized photon position calculation method.

A.4 Muon Detector Design, R&D and Test Beam Results

In Chapter 8, we gave an outline of our proposed muon detector design and evidence for a workable standalone dimuon trigger. In this section we provide details of the detector design, the assembly, the front-end electronics, the method of readout as well as a summary of the results of the beam test conducted during the summer of 1999.

A.4.1 Detector Design and Fabrication

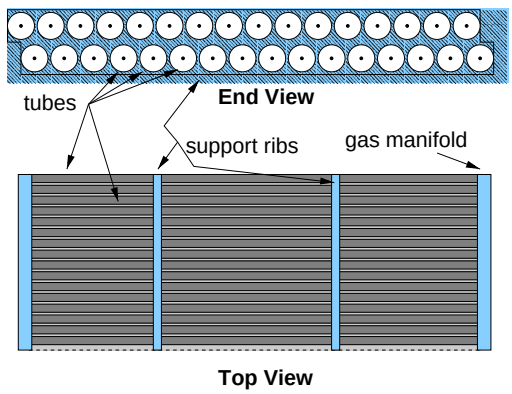

Figure A.45: End and top views of one "plank" of proportional tubes.

A.4.1.1 Basic Building Block: Proportional Tube Plank

The basic building block in the construction of a detector station is a "plank" of 3/8" stainless steel proportional tubes as shown in Fig. A.45. Thirty-two tubes are arranged in a double layer with an offset of half a tube ("picket fence" geometry). The tubes will be soldered to brass gas manifolds at each end. For the longer tubes, additional brass support braces will also be soldered to the tubes. This soldering technique has been tested by us and is simple and efficient. This system provides a sturdy, self-supporting building block. Soldering the tubes to brass also provides an excellent Faraday cage for the tubes. Proportional tubes have been selected as the detector technology because they are robust and have the necessary rate capability. We intend to use a fast gas (such as 88% Ar, 10% CF_4, 2% CO_2, which has a drift velocity of roughly 9 cm/μs [1]) so the maximum collection time (drift plus charge integration) for a signal should be less than 60 ns. Use of thin walled (0.01") stainless steel tubes has been proven to work by the CDF collaboration where similar tubes [2] had a long lifetime with low failure rate.

The 0.5 cm effective wire spacing of this design has a spatial resolution of 1.5 mm (5 mm / $\sqrt{12}$), with no dead regions between tubes.

A.4.1.2 Design of a Detector Station

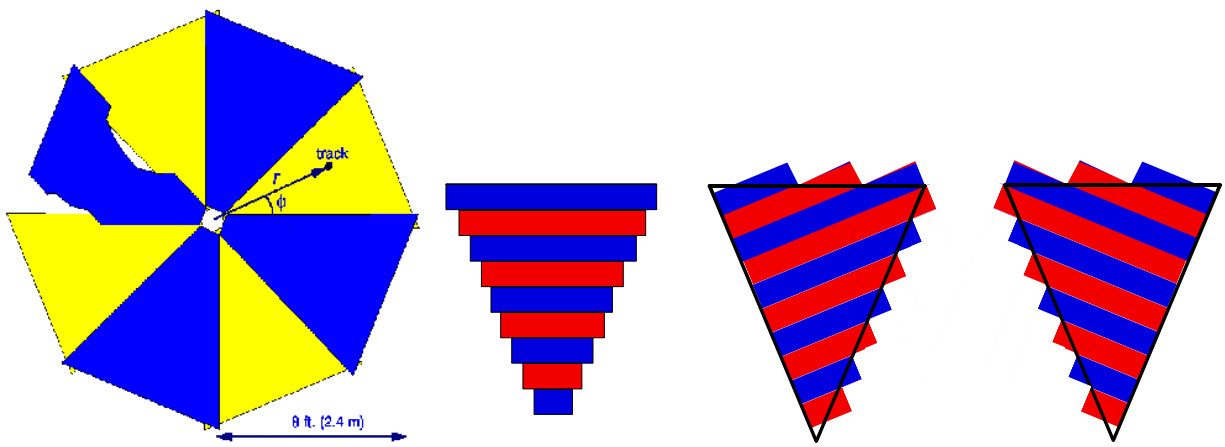

Figure A.46: (left) Beams-eye view of one muon detector station, which consists of eight overlapping octants arranged in two layers. One octant is cut away in places to show the overlap between adjacent octants. (right) Arrangement of planks to form the four views in an octant (r view is repeated). There will be 13 planks per view (more than shown).

To minimize occupancy at small radii and to minimize pattern recognition confusion, each detector station will consist of eight overlapping pie shaped "octants," as shown in Fig. A.46a. The four views (r, u, v, and r) in each octant are shown in Fig. A.46b. The r (radial) view is repeated to provide redundancy for the most important (bend) view and help reject fake tracks. The u and v stereo views are rotated $\pm 22.5^{\mathrm{o}}$ from the r view and are used to measure ϕ to resolve hit ambiguities. This geometry gives excellent resolution and redundancy in the bend direction ($\hat{\theta}$) of the toroids, and the resolution in the $\hat{\phi}$ direction is reasonable ($\sigma_\phi = 2.8$ mm, which is approximately twice the single plank resolution).

To construct an octant, the views are stacked on top of each other and are built from the planks described above. There will be 13 planks in each view of an octant ranging in length from 1 foot to 6 feet. This octant geometry has several advantages. In all views, the planks are short near the beam pipe and get longer at larger radii. This gives us shorter tubes where the occupancy is high and longer tubes away from the beam pipe which keeps the cost down. In addition to spreading the occupancy in a sensible way, splitting the system into octants should also help minimize pattern recognition confusion.

Pairs of octants will be combined into quads which will be the structure moved in and out of the spectrometer. These quads will be composed of 1/8" sheets of aluminum on which all of the planks are attached. Since the two octants that make up a quad are staggered in z, there are actually 8 (4 views for 2 octants) layers of planks in z (although the actual overlap is small). Each of the 8 layers of planks will be attached (front and back) to a 1/8" thick aluminum support sheet. This sheet will cover the entire quad area and will also act as a δ-ray shield.

With 32 channels per plank, 13 planks per view, 4 views per octant, 8 octants per station,

3 stations per arm, and 2 arms in the spectrometer, we arrive at 79,872 total channels in the system.

A.4.1.3 Proportional Tube Details

Each of the 32 tubes in a plank share a common gas manifold at each end which is made of brass and soldered to the tubes. The wires will be held at positive high voltage and read out through a blocking capacitor by front-end electronics which will attach at one end. High voltage will be fed to the plank at the same end as the electronics. We intend to use a "fast" gas mixture of 88% Ar, 10% CF_4, 2% CO_2 or something similar. For more details on the front-end electronics, expected signals, etc., see the section on front-end electronics below.

The tubes in the system will vary from 1–6 feet in length. During the beam test in the summer of 1999 we tested 10 planks with tubes ranging in length from 1–6 feet strung with 30 and 50 micron wire. There was no sign of wire slippage or breakage in the 320 channels. We plan on using 30 micron wire because it allows one to use lower high-voltage to achieve the same gain (see Section A.4.2.3). Our calculations and tests indicate no wire supports are necessary, even for 6-foot tubes.

After soldering the tubes to the gas manifold, the tubes will be strung and the wires held in place via a crimp pin. The arrangement is very similar to that used in the CDF muon system [2]. The crimp pins will extend out of the gas manifold and will attach to a circuit board which contains the blocking capacitors and an edge connector for the front-end cards.

A.4.1.4 Miscellaneous Mechanical Details

Because of the overlapping octant geometry of each detector station, there is plenty of room for cabling and front-end electronics everywhere except near the beam pipe. Space limittions at small radii limits the inner radius of the system to approximately 16 cm. GEANT studies of our detector at design luminosity (described in 8.3.1) indicate the innermost r-view tube (at $r = 16$ cm) of the first station will have an occupancy of 35% (the u and v views and downstream stations have significantly less occupancy). Therefore an inner radius of 16 cm is reasonable from a physics perspective as well as from a space constraint perspective. The hits from the minimum bias background have a $\sim 1/r^2$ dependence; as a result, at a radius of $r = 32$ cm the r-view occupancy of the first station drops to 7%. For stations 2 & 3, the r-view occupancy is 10% (2%) for r=16 cm (r=32 cm).

Weight is a potential concern because we are using stainless tubes. Using thin walled tubes reduces this concern significantly. We estimate the weight of the stainless tubes in one octant (all four views) to be 250 lbs, the same as if we were to use 1/32" thick aluminum tubes. However, the hanging frame used to support the octants and the supporting Aluminum sheets will probably double the weight of each octant, so that each detector station will weigh 1.5–2 tons.

We plan on building one extra station of spares ($1/6 = 16\%$ of those in the total system). The spares will be in the form of loose planks. If a problem develops (more than a handful of broken wires, etc.), we will take out a quad, replace the plank, and put the quad back.

Fabrication will take place at the three collaborating muon institutions, Illinois, Puerto Rico, and Vanderbilt.

A.4.2 Front End Electronics

In order to capture all the charge coming from a typical proportional tube for a single incident ionizing particle, one must integrate the charge due to the positive ion drift over a long period of time relative to the expected beam crossing for the BTeV experiment. The time needed to collect a portion of the total charge is a function of the gas used in the proportional tube, the geometry of the tube, and the high voltage bias of the center wire, relative to the outer conductor [3],[4]:

$$\frac{Q}{Q_o} = \frac{\ln(1 + t/t_o)}{2\ln(b/a)}$$

where Q is the charge collected in an amount of time, t, Q_o is the total charge from the ionization (depends on the gain of the tube), b and a are the outer and inner radius, respectively, of the conductors in the proportional tube, and [4]:

$$t_o \sim \frac{a}{2v_d}$$

where v_d is the drift velocity of the gas for the chosen value of the gain in the tube [1]. Alternatively, for a very fast signal, one could try to just capture the fast signal coming from the electron amplification, but this is only 1–2% of Q_o.

In BTeV we intend to use the muon proportional tubes in the Level 1 Trigger. The natural cutoff for integrating a signal then is on the order of a beam crossing, or 100 ns. However, we would like to reduce backgrounds associated with the collider beams, which pass through 60–70 ns before the interaction products arrive. For a fast gas like $ArCO_2CH_4$ [1], and an effective wire-to-wire spacing of 0.5 cm, the maximum drift time before the first signals from a track arrive is about 30 ns. This means that if we would like to be able to separate the various beam crossings, our electronics should be able to resolve 2 hits occurring 30 ns apart.

A.4.2.1 Amplifier choice

Fortunately, electronics to amplify and digitize the analog signal from a chamber hit in a high rate environment were developed for the SSC [3], and continue to be refined for use in detectors for the LHC [5] and at Fermilab [6]. We will take full advantage of these developments.

We intend to mimic the setup used for the CDF COT [6]. There will be a PC board soldered to the end of the gas manifold to deliver high voltage to each proportional tube. Connected to this is another PC board with electronics to amplify and digitize the tube signal. The high voltage will be delivered to each plank by one SHV cable. Therefore, high voltage will be adjustable on a plank-by-plank basis but not on a tube-by-tube basis.

We plan to utilize the ASDQ chip developed at the University of Pennsylvania to amplify and digitize the signals coming from the proportional tubes. The family of ASD chips (and applications) is described in detail elsewhere [3],[6], but we briefly mention some of the more important features here.

The ASD8B, which is being used for evaluation and beam tests is a predecessor of the ASDQ chip. The ASD8B (ASDQ) chip amplifies the first 6 ns (10 ns) of the signal and outputs an LVDS (equivalent) differential logic signal. The ASD8B (ASDQ) chip, when mounted on a PC board, has a low effective threshold of about 1 fC (2fc). The ASD8B noise level was verified in tests we performed on an evaluation board supplied by the University of Pennsylvania in December of 1998. Both chips features a double pulse resolution of ~20 ns. This family of chips seem to be an ideal choice for the BTeV muon system, and it is important to determine if we have sufficient signal to utilize them.

A.4.2.2 Practical Considerations

To calculate the signal expected in the proportional tube, we use the data presented in reference [1]. For the same gain as quoted in the paper($\sim 1.8 \times 10^5$), we can use the quoted results to determine our operating parameters for different tube geometries and gas mixtures. In Table A.4.2.2, we summarize the results for different gases and inner conductor radii.

Table A.4: Operating parameters for different gases and inner wire radii (a). The values of t^M_{drift} assume a wire space of 0.5 cm.

Gas	$E_{field}\|_a$	v_d	V_{bias}	Q_{6ns}	t^M_{drift}	a
$\frac{\text{ArC}_2\text{H}_6}{50/50}$	$150(\frac{\text{kV}}{\text{cm}})$	$4.8(\frac{\text{cm}}{\mu\text{s}})$	3545(V)	7.8(fC)	50(ns)	50(μm)
$\frac{\text{ArCO}_2}{80/20}$	164	2.4	3768	5.9	100	50
$\frac{\text{ArCO}_2\text{CF}_4}{88/2/10}$	150	8.7	3454	9.5	30	50
$\frac{\text{ArC}_2\text{H}_6}{50/50}$	150	4.8	1656	8.8	50	20
$\frac{\text{ArCO}_2}{80/20}$	164	2.4	1806	7.1	100	20
$\frac{\text{ArCO}_2\text{CF}_4}{88/2/10}$	150	8.7	1656	10.4	30	20

In the table, we have made some assumptions. We've assumed that the most important factor in calculating the gain is sensitivity to a *single* ionization cluster of a *single* electron–ion pair; we haven't taken into account the effect of adding a termination resistor (see below); we haven't taken into account the effect of a magnetic field; and we've neglected aging effects in the tube. We've also taken for granted that the electronics will be located at the end of the proportional tubes: lowering the electronic noise and increasing the amount of signal we get in the small integration time available. Even so, we can learn a great deal from looking at the table.

A.4.2.3 Amplifier Observations

A smaller wire size is desirable from an electronics standpoint: the operating voltage (V_{bias}) is lower and the integrated charge collected ($Q_{6\text{ns}}$) is a little higher. The lower operating voltage gives us more flexibility in the choice of a decoupling capacitor, allowing the option of surface mount components in the high voltage system. The higher integrated charge means we can safely raise the threshold of the electronics without losing signal, allowing greater flexibility in our noise budget. Additionally, it is expected that the gain of a tube has less sensitivity to the operating voltage with a smaller wire [1].

Also evident is the advantage of having a fast gas. Not only can one integrate more charge in a smaller period of time, one has less sensitivity to beam crossings. We can achieve our goal, stated previously, of the first signal to arrive after a maximum time of about $t^M_{\text{drift}} = 30$ ns.

Another way to look at the table is to reason that all the combinations calculated will produce a working detector, and that using the ASD chip allows us flexibility in our choice of wire diameter, gas, and operating voltage.

At most, a termination resistor will raise our noise by 1 fC and lower our gain by a factor of 2. This is to be offset by the expectation that about 10 primary ion-pair clusters will be produced, on average, for a MIP passing through 1/3 cm of gas volume.

One final consideration in evaluating the ASD8B for BTeV is that the process used to make the chip is obsolete and the chip will not be available in production quantities [7]. We plan to use the improved version (ASDQ). It integrates for a slightly longer period, has the same double pulse resolution, and has a higher intrinsic noise level of $\sim$2 fC.

A.4.2.4 Results of the Beam Test

In the summer of 1999 we contructed 320 channels in 10 planks, reading out 128 channels in 8 planks (due to limited electronics). The front part of the setup showing 3 one-foot planks followed by 2 six-foot planks with high-voltage and readout cables is shown in Fig. A.47. This construction did not have the Faraday cage properties of our current design. The gas manifolds were made of an insulator and glued to the tubes. The other supports, although made of aluminum, were glued, increasing the resistance between tubes up to 50 Ω. We used the ASD8B chip to amplify and digitize the signal. In our initial tests, we found that the ASD8B was very sensitive to RF noise and, in our configuration, required a nearly complete Faraday cage around the amplifier card. This was accomplished by wrapping the tubes with aluminum foil and constructing boxes made of copper plated G10 in which the amplifier card resided. These boxes were connected to the aluminum foil with copper tape. With the Faraday cage in place it was possible to reduce the random noise to sufficiently low levels. This is the motivation for our current design which naturally creates a Faraday cage by soldering the tubes to a brass gas manifold and connecting these to aluminum sheets which will extend out to the end of the electronics allowing a Faraday cage around the electronics.

With the makeshift Faraday cage in place we determined that the ASD8B chip gave enough gain as demonstrated by the plateau curves in Fig. A.48. Unfortunately, further

Figure A.47: Photo of the muon testbeam setup. The beam direction was from right to left. Three of the one-foot planks and the two six-foot planks can be seen. The remaining planks (two three-foot planks and three more one-foot planks) are further back. The planks and cables are wrapped in aluminum foil to provide sheilding. The amplifiers are inside boxes made of copper-plated G10.

tests revealed that with the front-end design we implemented, the level of cross-talk was quite high. That is, when only one or two tubes should be firing when a single particle passed through, oftentimes, five or six would fire. At the end of the beam test, the cross-talk was reduced by adding termination resistors to the open end of the tube. We believe we can reduce the noise even further with a more intelligent signal routing scheme and/or additional small components.

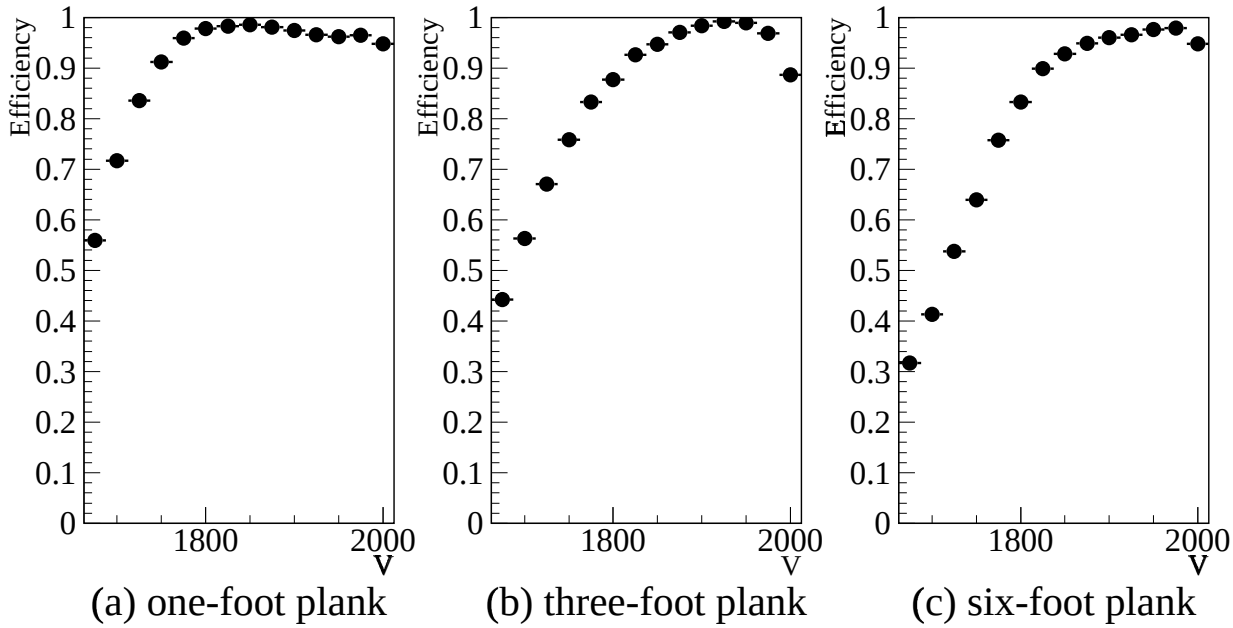

Figure A.48: Plateau curves (efficiency versus voltage) for a one-foot, three-foot, and six-foot plank of tubes. We require hits in scintillators upstream and downstream of the muon planks and for these events we read out single-hit LeCroy TDC's to determine if a hit occurred at the proper time. The drop in efficiency above the plateau is due to the particular readout electronics (single-hit TDC's with a long gate) when high hit rates are encountered. These data were taken using the tubes strung with 30 micron wire with 80%/20% Ar/CO_2 gas.

A.4.2.5 Front–end Readout

As mentioned previously, the ASD chips produce differential logic signals (LVDS) suitable for driving up to 10 m of cable. The LVDS signal consists of 1 bit/channel signifying whether or not a channel is on or off. The BTeV experiment plans to use optical fiber to deliver data to the counting room upstairs. We plan to convert the signals to optical at the octant level. Converting each plank of 32 channels to optical would require 2496 optical connections which is quite expensive and inefficient. Similarly, bringing all 79,872 channels out of the muon system to the north wall would require a large amount of cables and many racks of serializing boards. We propose to use copper-based twisted-flat cables to connect the 13 planks that make up one view of one octant to a serializer board(s). These 13 planks (416 channels) would be sparsified, serialized, and delivered to the counting room on an optical-fiber link. Other links will also be used to run the slow control (mainly threshold setting) and monitoring.

A.4.3 Future prototyping

We plan to continue developing prototypes over the next year. We are planning on building on the successful construction of the first prototypes for the beam test in the summer of 1999. The basic construction change that we will be making is to solder brass gas manifolds to the tubes instead of gluing plastic gas manifolds. This was motivated by the requirement of a good Faraday cage for the tubes and the amplifier. The basic soldering technique has been verified on a small test sample. Since this soldering technique requires heating the tubes, it was felt that rather than stringing the tubes first and then attaching the manifold (as was done in the first prototypes) it would be safer to solder the manifold (and any support pieces) and *then* string the tubes. This requires a slight adjustment of the tools and methods used to string the tubes, especially in crimping the wire to the crimp pin which holds the wire at tension.

In our next round of prototypes we will test the basic changes to the construction (soldering instead of gluing and crimping after instead of before). We would like to verify that the new construction method is as efficient and reliable as the old method. In addition, we would like to determine how much this helps reduce the noise problems we saw with unshielded tubes in the previous prototype. Finally, we would like this to proceed rapidly so that we can conduct long-term tests of the system including such potential problems as wire "creep," gas "poisoning," etc.

We will also require new prototypes for the front-end electronics. The new prototype will be using the ASDQ chip instead of the ASD8B chip, used previously. We are also planning a new prototype for the card which uses the ASDQ chip. We have many ideas for improving the layout of this card compared to its predecessor which was used for the 1999 test beam run. These improvements include better signal routing and possibly an analog buffer.

Bibliography

[1] J.M. Butler *et al.*, "Study Of Fast Gases, Resolutions And Contaminants In The D0 Muon System," Nucl. Instrum. Meth. **A290**, 122 (1990).

[2] S. Bhadra, S. Errede, L. Fishback, H. Keutelian and P. Schlabach, "The Design And Construction Of The CDF Central Drift Tube Array," Nucl. Instr. Meth. **A268**, 92 (1988).

[3] "A Fast, Low Power, Amplifier-Shaper-Discriminator for High Rate Straw Tracking Systems," F.M. Newcomer *et al.*, Trans. Nuclear Science, Vol 40, N4, P630-636, August, 1993.

[4] F. Sauli in *EXPERIMENTAL TECHNIQUES IN HIGH-ENERGY NUCLEAR AND PARTICLE PHYSICS (2nd ed.)*, edited by T. Ferbel, World Scientific, Singapore 1991, p. 79.

[5] ATLAS Collaboration,"ATLAS inner detector: Technical design report. Vol. 2," CERN-LHCC-97-17.

[6] R. Blair *et al.* [CDF-II Collaboration], "The CDF-II detector: Technical design report," FERMILAB-PUB-96-390-E.

[7] M. Newcomer, *Private Communication.*

A.5 Level 1 Trigger Timing Studies

A.5.1 Introduction

During the past year, considerable effort has been devoted to timing studies of the Level 1 vertex trigger. Since the vertex trigger must perform a large number of calculations in a very short time, the number of processors required to do the job is large. It is important to have an accurate determination of the number of processors, because factors of two or more can have a significant impact on whether or not a particular design is feasible. For example, a farm of 50,000 digital signal processors (DSPs) might be difficult to maintain, whereas farms of $\approx 10,000$ DSPs are being operated successfully [1].

Fortunately, the timing studies for the calculations that we plan to perform using DSPs indicate that Level 1 requires fewer than 2300 DSPs. This number will shrink as processor speeds increase.

To obtain an accurate estimate of the processing needs for Level 1, we adopted an aggressive approach aimed at achieving maximum performance for the type of DSP selected for our design study. This approach was called for, since early estimates based on Level 1 trigger code suggested that very large numbers of processors might be needed. For our studies we selected the Texas Instruments 200 MHz TMS320C67X floating-point DSP, rated at 1200 MFLOPS. We are also considering the ADSP-2106x family of DSPs made by Analog Devices for use in the trigger, but all of our detailed timing studies were done assuming the TI DSP.

The software for our timing studies is the Level 1 trigger code. This is the same track and vertex reconstruction software that is used to determine trigger efficiencies for physics simulations, and to study the Level 1 trigger performance (see Chapter 14). The trigger code that finds track segments is not included in the timing studies, since the segment finding is performed by the FPGA tracker, not by DSPs.

Three key decisions made it possible for us to achieve our final timing estimate for Level 1. First, we decided to develop the trigger code using a Windows PC development and debugging environment. This made it possible to develop the trigger code for three different purposes: (i) physics simulations running under UNIX, (ii) detailed trigger studies using the Windows development environment, and (iii) vendor-supplied DSP simulators, which are often able to run the code developed for the Windows environment (without too many platform-specific modifications). Second, we decided to write the trigger code using the lowest-level assembly language for the TMS320C67X DSP. This leads to a signficant increase in the effort required to implement the trigger code in the DSP, but it provides the maximum performance gains. The resulting code is called *expert-optimized assembly-language code*, in contrast to the code that is generated by an optimizing compiler. The expert-optimized code development involves interleaving calculations, rearranging the order of calculations compared to the original C code, and tailoring the code to the specific architecture of the TMS320C67X. Third, we included timing estimates for "operating-system software," so that our time estimates are representative of all software required for a complete implementation of the Level 1 trigger code. This includes code for memory management, I/O and DMA

support, as well as interrupt and error handling. Time estimates for the operating-system software are based on code developed for the BTeV hardware trigger prototype.

Our final result for the number of processors required to execute the Level 1 trigger code using the TMS320C67X is 2300 DSPs. This represents a factor of 20–50 improvement (depending on the level of optimization achieved for different subroutines) compared to a high-level C-code implementation of the trigger algorithm. This result is significant, since it means that a much smaller number of processors (a factor of 20–50 fewer processors) is required for Level 1, compared to an estimate that is based on a high-level implementation of our trigger algorithms.

A.5.2 Timing Studies

As shown in Fig. 9.3 and described in Chapter 9, there are two distinct processor farms in the design of the Level 1 trigger. One farm is used to process tracks, the second is used for vertexing. The results from our timing studies are presented for the track and vertex farms in Tables A.5 and A.6, respectively.

Table A.5: DSP cycle counts for each subroutine in the track processing code. The cycle counts are calculated per pixel detector quadrant per beam crossing.

Subroutine	cycles/quadrant/crossing
bb33–triplet–sorting	650
bb33–forward–matching	980
bb33–backward–matching	980
bb33–faketrack–removal	1940
bb33–radius–of–curvature	1500
calculate–angles	660
extrapolate–yz–to–beamline	1440
extrapolate–xz–to–beamline	300
estimate–vertexing–errors	300
estimate–vertex–z–coord	240
calculate–momentum	660
Total DSP cycle count	9650

Table A.5 lists the subroutines that are executed by DSPs in the track farm. The table shows the estimated number of DSP cycles required by each subroutine. The estimates are based on an accurate determination of the number of machine-code operations, and the average number of trigger primitives handled by each subroutine (assuming an average of two interactions per beam crossing). We tend to overestimate the numbers of trigger primitives, and to assume maximum loop counts. For example, if a particular subroutine operates on an average of 5.2 tracks, we use 6 tracks for our time estimates. With regard to loop counts, the code often involves loops with conditional statements that permit loops to terminate before

completing all iterations. An example of this is a double loop over all interior and exterior track segments (ordered by pixel-station number) that finds matching track segments. As soon as a match is found by the Level 1 trigger code, the loop terminates. We simplify our estimate of the time required to execute this double loop by assuming that the loop does not terminate until all combinations of interior and exterior track segments have been considered. This overestimates the required time, but it is a conservative result that we are comfortable with.

Our estimate for the number of TMS320C67X DSPs required for the track farm is calculated as follows. We multiply the total number of DSP cycles required by the track subroutines by the cycle time (5 ns) for the TMS320C67X DSP. This gives us an average time of 48.25 μs per quadrant per beam crossing. We add 6.75 μs for the "operating system" overhead, and obtain 55 μs. Finally, we require a large enough number of DSPs working in parallel so that a processor is available every 132 ns, on average. Therefore, we need 417 DSPs per quadrant, or a total of 1668. For faster DSPs that Texas Instruments will unveil in the coming years, the cycle counts shown in Table A.5 should remain the same (TI promises code compatibility), and the time per cycle will be reduced.

Table A.6: DSP cycle counts for each subroutine in the vertex processing code. The cycle counts are calculated per beam crossing.

Subroutine	cycles/crossing
setup–tracks	1925
get–ip–miss–at–primary	3060
compare–tr–to–clst	4788
calculate–cluster–vertex	360
add–to–cluster	1080
vtxp1–init	50
vtxp2–clusters	120
vtxp3–primary	90
vtxp4–add–tracks	1200
vtxp5–detach–tracks	600
vtxp6–detach–tracks	600
vtxp7–count–dtracks	300
vtxp8–count–dtracks	300
vtxp9–trigger	200
Total DSP cycle count	14673

For the vertex farm we use the cycle counts listed in Table A.6. This gives us an average time of 73.4 μs per beam crossing. The processors in the vertex farm are not subdivided by quadrants, so we do not multiply this result by 4. We add 3.8 μs for the "operating system" overhead, and obtain 77.2 μs. The total DSP count is 585.

Thus, the total DSP count for Level 1 is 2253.

Bibliography

[1] D. Chen *et al.*, Nucl. Phys. Proc. Suppl. **73** (1999) 898.